



MAX-PLANCK-GESELLSCHAFT



**Kinetics of Methanol Electrooxidation on PtRu Catalysts
in a Membrane Electrode Assembly**

**Kinetik der Elektrooxidation von Methanol an PtRu
Katalysatoren auf einer Membranelektrode**

Dissertation

zur Erlangung des akademischen Grades

**Doktoringenieur
(Dr. - Ing)**

von Dipl.-Ing. Tanja Vidaković

geb. am 2. September 1970 in Požega, Serbia

genehmigt durch die Fakultät für Verfahrens- und Systemtechnik
der Otto-von-Guericke-Universität Magdeburg

Gutachter: Prof. Dr.-Ing. habil. Kai Sundmacher
Prof. Dr. Mihai Christov
Prof. Dr. habil. Helmut Weiß

Promotionskolloquium am 17. 06. 2005

Table of contents

Preface.....	IV
Abstract.....	VI
Zusammenfassung	VII
1. Introduction	1
2. Experimental.....	6
2.1. Electrochemical cell.....	6
2.2. Reactants	7
2.3. Electrocatalysts	7
2.4. Preparation of MEA	7
2.5. Electrochemical measurements.....	8
2.6. CO stripping voltammetry	9
2.7. Determination of ohmic resistance	9
2.8. Comparison of steady state and quasi-steady state measurements	10
2.9. Determination of geometric surface area.....	11
3. Electrochemical methods for the real surface area determination	14
3.1. Hydrogen adsorption method.....	15
3.1.1. Experimental approach	18
3.1.2. Determination of real surface area of unsupported Pt catalyst.....	19
3.2. CO adsorption method	21
3.2.1. Experimental approach	25
3.2.2. Unsupported Pt catalyst	26
3.2.3. Unsupported PtRu catalyst.....	30
3.3. Conclusions.....	38
3.4. Outlook	39
4. Kinetics of methanol oxidation.....	40
4.1. Mechanism of methanol electrooxidation – Literature overview	41
4.2. Catalyst characterization.....	52
4.3. Activity in methanol oxidation – Experimental findings.....	55
4.3.1. Influence of flow rate.....	55
4.3.2. Influence of methanol concentration	58
4.3.3. Electrochemical impedance spectroscopy	60
4.3.4. Influence of temperature.....	62
4.4. Mechanism and rate expression for methanol oxidation	64

4.5.	Simulated vs. experimental data	67
4.6.	Influence of PtRu loading	71
4.6.1.	Catalyst characterisation	71
4.6.2.	Activity towards methanol oxidation.....	72
4.7.	Influence of support	72
4.7.1.	Cyclic voltammetry in the absence of methanol.....	73
4.7.2.	Activity towards methanol oxidation.....	73
4.8.	Conclusions.....	74
4.9.	Outlook	75
5.	Relation between catalyst synthesis and activity in methanol electrooxidation	76
5.1.	Methods for nanoparticle preparation.....	77
5.2.	Experimental	81
5.2.1.	Catalyst synthesis.....	81
5.2.2.	Physical methods	86
5.2.3.	Electrochemical methods	87
5.3.	Characterisation of catalysts	87
5.3.1.	Physical methods	87
5.3.2.	CO stripping.....	94
5.3.3.	Cyclic voltammetry in absence of methanol.....	99
5.4.	Catalyst activity in methanol oxidation	102
5.4.1.	Current vs. time - stability test	106
5.4.2.	Electrochemical impedance spectroscopy	107
5.5.	Influence of conditioning, support and leaching.....	108
5.5.1.	Influence of conditioning.....	108
5.5.2.	Influence of support	111
5.5.3.	Influence of leaching.....	112
5.6.	Conclusions.....	115
5.7.	Outlook	116
6.	Concluding Remarks.....	117
7.	References	119
	Appendix I	124
	Appendix II.....	128

Preface

This thesis was done at the Max-Planck Institute for Dynamics of Complex Technical Systems in Magdeburg, during my 2 years stay at the Institute. However, the beginning of my work in this topic was in Belgrade at the Department of Physical Chemistry and Electrochemistry, Faculty of Technology and Metallurgy. There I made my first steps in the field of methanol oxidation under supervision of Prof. Snezana Gojković. I would like to thank Prof. Snezana Gojković for understanding my decision to continue my work and to defend my thesis in Magdeburg. So, in 2002 I decided to come to Germany, join the group of Prof. Sundmacher and continue work on the same topic but in a different kind of system. In order to do so, I first had to get a leave of absence from my Faculty in Belgrade, where I have been working as a teaching assistant since 1995. At this point I would like to express my gratitude to my colleagues and Professors at the Department of Physical Chemistry and Electrochemistry who took over and distributed my normal teaching duties in this time and allowed me to concentrate only on the research. I owe special thanks to my Diploma and Master Thesis supervisor Prof. Branislav Nikolić, who supported my idea to come to Magdeburg in spite of his concerns that it will double my work on the thesis.

For my stay in Magdeburg I would like to thank Prof. Sundmacher, who accepted my application to work on one of the projects in his group related to the kinetics of methanol oxidation and also the Max-Planck Society, which provided me a scholarship during my stay. Prof. Sundmacher was a supervisor who tried to teach me the importance of numbers and equations. I would like to thank him for being patient and supportive. Besides Prof. Sundmacher during my stay in Magdeburg I was closely working with Prof. Christov from the University of Metallurgy in Sofia, Bulgaria. His help on my thesis was inevitable and I thank him a lot.

One can say that the major output of my thesis was formulation of a rate expression for the methanol oxidation, which in my opinion can explain most of the literature as well as our results. Besides, the reaction kinetics was investigated on different test catalysts. These results seem also very promising and I hope that in combination with the model they will bring a better insight into a “smart” catalyst design. For having an opportunity to work with these test catalysts I would like to thank Prof. Bönnemann (and Prof. Sundmacher) from the Max-Planck Institute for Coal Research, Mülheim an der Ruhr. In 2003 I had a privilege to spend some time in his research lab and get some hands-on experience in catalyst synthesis.

In this respect I would like to thank the colleagues with whom I was working over there (Dr K. Nagabushana, W. Fei and S. Kinge) and to the Analytical service groups of this Institute which provided me the results on physical characterisation of the catalysts.

Besides my scientific work, equally important thing that I learnt in Magdeburg was an importance of teamwork. At this point I am especially grateful to my colleagues Dilp.-Ing Ulrike Krewer and Dr Thorsten Schultz. Ulrike tried to teach me many different things and always was a very good friend.

I would also like to thank Prof. Weiß from the Otto-von-Guericke University in Magdeburg for accepting to be co-referee of this thesis.

Last but not least I am thankful to my family who always supported my decisions and to my friends both in Belgrade and Magdeburg for being good friends in all this time.

Magdeburg, June 28th, 2005

Abstract

In this study the kinetics of methanol oxidation was investigated on the state-of-the-art PtRu-catalysts. The influence of methanol concentration, temperature and flow rate was investigated. The influence of the electrode metal loading was also evaluated and the activity of supported *vs.* unsupported catalysts was compared. The activity with respect to methanol oxidation is influenced by the catalyst synthesis. Catalysts synthesized by Bönemann's "precursor method" using pre-prepared PtRu metal colloids were characterized by physical and electrochemical methods and their activity towards methanol oxidation was determined. An important factor for the catalyst activity is its real surface area. It was determined by CO stripping voltammetry.

In order to study the kinetics of anodic methanol electrooxidation on a membrane electrode assembly (MEA) under technically relevant conditions a special type of electrochemical cell, the cyclone flow cell (CFC), was used. The experiments (steady-state, cyclic voltammetry, chronoamperometry and electrochemical impedance spectroscopy) were performed at temperatures between 22 and 60 °C. MEA's were prepared by spraying the catalyst onto a Nafion[®] membrane followed by hot pressing to the back diffusion layer. Both commercial (Johnson Matthey) and non-commercial (Max-Planck-Institut für Kohlenforschung in Mülheim an der Ruhr) supported and unsupported catalysts of nominal composition Pt:Ru - 1:1 were used. The electrode metal loading was varied between 1 and 5 mg cm⁻². In the working electrode compartment 1M methanol in water was circulated at different flow rates. The supporting electrolyte in the counter electrode compartment was 1 M sulphuric acid.

The formal reaction order with respect to methanol in the activation controlled region changes from 0.3 at low methanol concentrations to 0 at higher methanol concentrations, while at the beginning of the limiting current region the variation of the reaction order is less pronounced and the mean value is about 0.7. Apparent Tafel slope values in the activation control region were dependent on methanol concentration and temperature (typically values of about 130 mV dec⁻¹ were determined at room temperature, while about 100 mV dec⁻¹ at 60° C for 1 M methanol solution). The apparent activation energy was determined to be 56±2 kJ mol⁻¹ in the activation controlled region and 34±2 kJ mol⁻¹ in the limiting current region. It was assumed that an electrochemical reaction is the rate-determining step in the activation controlled region while in the limiting current region it is the methanol adsorption step. A rate expression for the methanol oxidation is derived which, shows a good qualitative agreement with the experimental data.

Zusammenfassung

In der vorliegenden Arbeit wurde die Kinetik der Methanoloxidation an PtRu-Katalysatoren untersucht. Es wurde der Einfluss der Methanolkonzentration, der Temperatur, der Strömungsgeschwindigkeit, sowie der Metallbeladung analysiert. Eine Gegenüberstellung von geträgerten und ungeträgerten Katalysatoren wurde ebenfalls unternommen. Es wurde festgestellt, dass die Aktivität im Hinblick auf die Methanoloxidation vom Syntheseweg des Katalysators abhängig ist. Einige nach dem Bönemann-Verfahren aus PtRu-Kolloidpartikeln hergestellten Katalysatoren wurden mit Hilfe physikalischer und elektrochemischer Methoden charakterisiert und als Methanolelektroden untersucht. Ein wichtiger Aspekt der Katalysatoraktivität ist die reale Elektrodenoberfläche, die durch voltamperometrische Oxidation von adsorbiertem CO bestimmt wurde.

Um die Kinetik der anodischen Methanolelektrooxidation auf einer Membranelektrode unter praxisnahen Bedingungen untersuchen zu können, wurde eine spezielle elektrochemische Messzelle (Zyklonzelle) eingesetzt. Die Experimente (stationäre Strom-Spannungskurven, zyklische Voltammetrie, Chronoamperometrie und elektrochemische Impedanzspektroskopie) wurden bei Temperaturen zwischen 22 und 60° C durchgeführt. Die Membranelektroden wurden durch Aufsprühen des Katalysators auf die Nafionmembran hergestellt, die danach auf die Diffusionsschicht bei hoher Temperatur gepresst wurde. Als Katalysatoren (Pt:Ru=1:1) dienten sowohl kommerzielle (Johnson Matthey) als auch nicht kommerzielle (Max-Planck-Institut für Kohlenforschung in Mülheim an der Ruhr) Materialien. Die Metallbeladung, der Elektrodenfläche wurde zwischen 1 und 5 mg cm⁻² variiert. Auf die Seite der Arbeitselektrode wurde eine 1M wässrige Methanollösung mit verschiedenen Strömungsgeschwindigkeiten zugeführt. Der Leitelektrolyt auf der Seite der Gegenelektrode war eine 1M Schwefelsäurelösung.

Die formale Reaktionsordnung in Bezug auf Methanol ändert sich von 0,3 bei niedrigen Konzentrationen bis 0 bei hohen Konzentrationen im Durchtrittsüberspannungsbereich. Im Grenzstrombereich ist diese Reaktionsordnungsänderung schwächer ausgeprägt und beträgt etwa 0,7. Die scheinbaren Tafel-Steigungen hängen vom Potentialbereich und von der Konzentration ab (typische Werte: 130 mV dec⁻¹ bei Zimmertemperatur und 100 mV dec⁻¹ bei 60° C für 1 M Methanollösung). Die berechneten scheinbaren Aktivierungsenergien betragen 56±2 kJ mol⁻¹ im Durchtrittsüberspannungsbereich und 34±2 kJ mol⁻¹ im Grenzstrombereich. Es wird ein reaktionskinetisches Modell vorgeschlagen, das in guter qualitativer Übereinstimmung mit den experimentellen Daten steht.

1. Introduction

A fuel cell converts chemical energy into electrical energy (Figure 1.1). It consists of two electrodes sandwiched around an electrolyte layer. Reactants (oxygen/air, hydrogen, methanol etc.) are consumed on the electrodes generating electricity, heat and products of the reactions.

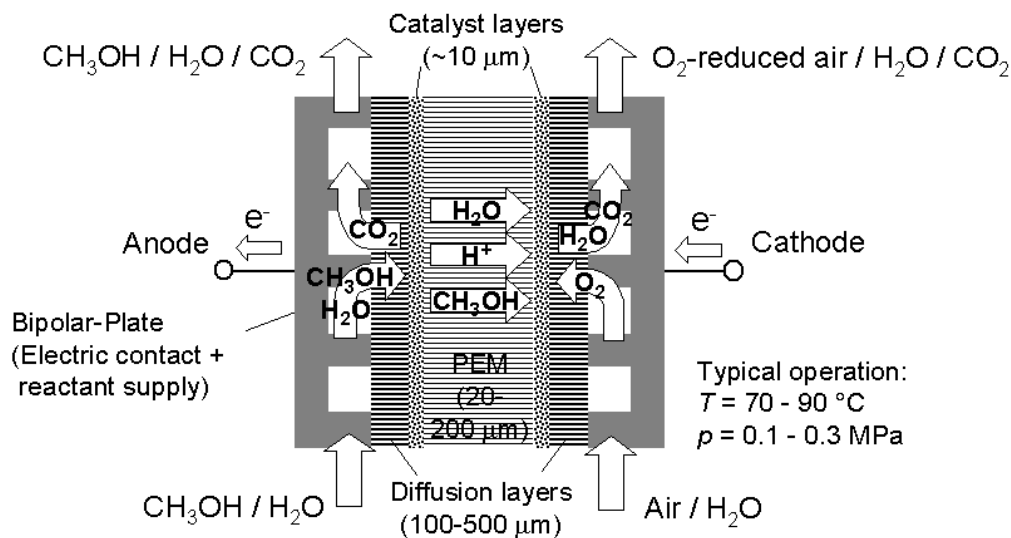


Figure 1.1 Schematic representation of a fuel cell [1].

Among many types of fuel cells, the Direct Methanol Fuel Cell (**DMFC**) deserves special attention due to relatively cheap, abundant, easy for handling and storage feeds (from one side methanol and from another oxygen/air). DMFC belongs to a group of low and intermediate temperatures (up to 150 °C) fuel cells and as an electrolyte employs a solid electrolyte. It has potential application in transport (it works at low temperature, does not produce much heat which otherwise has to be eliminated by some cooling device, has a short start-up period, it can be easily refilled, has low polluting emission (ideally carbon dioxide and water) etc. and as a portable power source (for example in laptops, pocket calculators, mobile phones etc). To be competitive at the market, the DMFC has to be able to operate at conditions close to ambient conditions and to deliver a high power density at low costs. Still there are a few obstacles on the way. They are: a) low catalyst activity and stability in

methanol oxidation, b) low catalyst activity in oxygen reduction and low tolerance with respect to methanol, c) methanol crossover, d) aspects regarding the fuel cell stack, like materials and design of cell housing, bipolar plates, gasketing etc. In this study emphasis was on point a) *i.e.* on slow kinetics of methanol oxidation.

Electrochemical oxidation of methanol can be presented by the following equation:

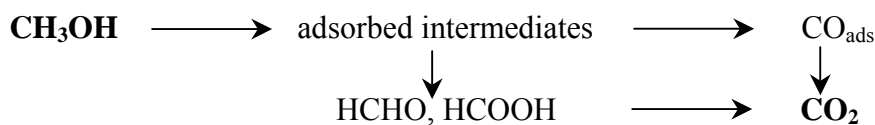


Thermodynamically this reaction is favourable (the equilibrium potential of methanol oxidation to CO_2 is close to the equilibrium potential of hydrogen reaction). In reality the overpotential of methanol oxidation is higher than of hydrogen oxidation. The difference in kinetics of these two reactions is due to the fact that hydrogen oxidation is the simpler reaction involving transfer of only two electrons, while methanol oxidation involves the transfer of six electrons and many adsorbed intermediates and side-products. Some of the reaction intermediates can irreversibly adsorb on the catalyst surface and hinder further reaction. In general, kinetics of a reaction with adsorbed intermediates and many elementary steps is greatly influenced by the catalyst (electrocatalyst). Thus, it is very important to develop an electrocatalyst which will improve the kinetics of methanol oxidation (decrease the overpotential of the reaction) and which will be resistant to poisoning.

To accomplish this demanding task, *i.e.* to develop “smart” electrocatalyst, one has to understand the main constraints of methanol oxidation. Therefore, apparent kinetic parameters (like formal reaction order, Tafel slope, activation energy, etc.) of the reaction have to be determined. Then a suitable reaction mechanism is assumed. So the overall reaction (equation (1.1)) is divided into elementary steps, where all steps together represent the mechanism of the reaction. In the last thirty years many mechanisms of methanol oxidation were proposed and an overview will be given in Chapter 4. As it will be seen in validating the reaction mechanism, different experimental techniques were used. Classical electrochemical techniques were used for the determination of the electrokinetic parameters: reaction orders with respect to methanol and H^+ , Tafel slopes, activation energies etc. For identification of reaction intermediates different spectroscopic techniques were used, like infrared spectroscopy or mass spectroscopy. The reaction was investigated on different electrocatalysts (for example platinum, platinum ruthenium alloys etc.) and in different cell configurations (standard three compartment electrochemical cell, fuel cell, half fuel cell).

Influence of methanol concentration, temperature, anions, catalyst surface composition and crystal orientation were studied.

It was concluded that, in principle, methanol oxidation can be formulated as follows:



Both of these pathways require a catalyst, which should be able to a) dissociate the C-H bond and b) facilitate the reaction of the resulting residue with some O-containing species to form CO₂ (or HCOOH). The first process involves adsorption of the methanol molecule and requires several neighbouring places at the surface. The second process requires dissociation of water, which is the oxygen donor for the reaction. Schematic presentation of these processes is shown in Figure 1.2 below.

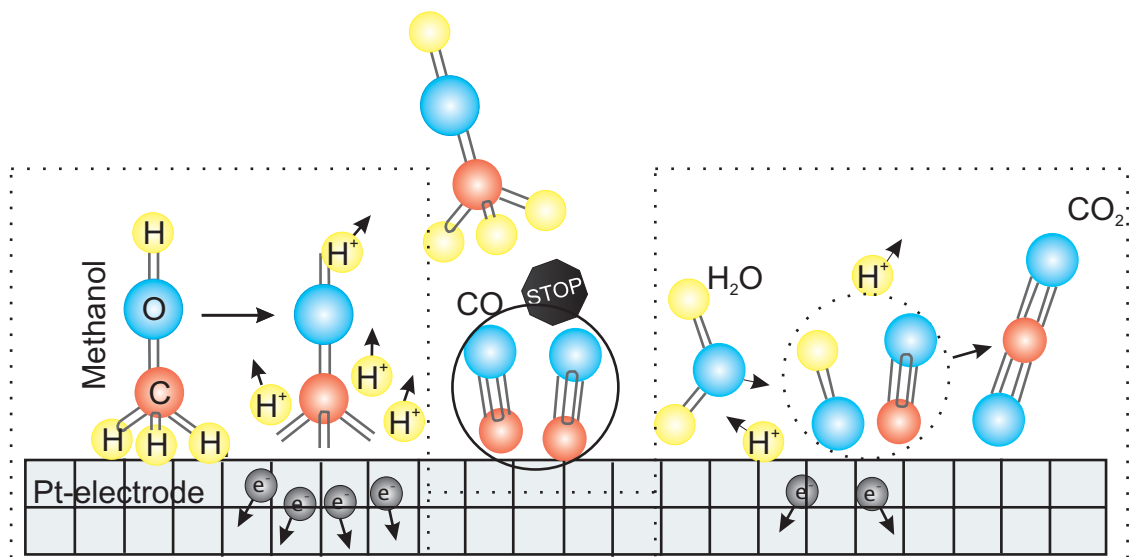


Figure 1.2 Schematic presentation of the different reaction steps during methanol oxidation on a model catalyst surface. From left to right, methanol adsorption followed by methanol dehydrogenation, adsorption of blocking CO intermediate, dissociation of water and formation of OH_{ads}, reaction between CO and OH adsorbed and CO₂ evolution (Adopted from reference [2]).

So far it was found that platinum is very active in step “a” (methanol dehydrogenation), but not very active in step “b” *i.e.* in oxidation of species formed after the dehydrogenation step. A strong interaction of water with the platinum surface is only possible at potentials above 0.4 – 0.45 V *vs.* RHE. Thus, on pure platinum methanol oxidation to CO₂ cannot start below 0.45 V. In reality, methanol oxidation at high enough rate for practical application can occur only at a much higher potential *i.e.* 0.7 V. So, the catalyst requires further improvement. If platinum is alloyed with a less noble metal like Ru, Sn etc. its activity

towards methanol oxidation will increase. Although some other combinations were tested, a platinum-ruthenium alloy proved to be the best choice up to now. The efficiency of PtRu catalyst was explained by the theory of bifunctional catalysis where platinum is responsible for methanol dehydrogenation and Ru for OH species donation. Thus, at PtRu catalysts methanol oxidation to CO₂ can start at 0.22 V vs. RHE. Again, a high enough reaction rate for practical operation is achieved at higher overpotentials (say, 0.5 V vs. RHE).

Today the state of the art catalyst for methanol oxidation is based on PtRu combinations. Although there are many studies devoted to the kinetics of methanol oxidation on PtRu, a lumped approach describing kinetics of methanol oxidation, under fuel cell relevant conditions, including reaction parameters (rate constants, reaction orders, etc.) is still missing. So, in this work kinetics of methanol oxidation on commercial unsupported PtRu catalyst under technically relevant conditions (60°C, 1 M methanol, membrane electrode assembly (MEA)) was studied and discussed in connection with literature results (Chapter 4). The reaction order with respect to methanol, Tafel slopes and apparent activation energies were determined and the influence of the flow rate of the surrounding fluid was checked. Based on experimental data and literature findings a suitable mechanism of methanol oxidation is proposed and a rate expression for methanol oxidation is derived. This rate expression can be later on implemented into a mathematical model of the whole DMFC.

The activity of the PtRu catalyst depends on the PtRu composition, the degree of alloying, the presence of oxide phase, particle size, support etc. These factors are influenced by the chosen catalyst preparation route. In Chapter 5 an overview of preparation routes for nanoparticle synthesis is given. Special emphasis is put on the colloidal route for nanoparticle synthesis with descriptions of three variations of colloidal salt reduction method. Catalysts synthesised in these ways were characterized by physical (energy dispersive X-ray analysis (EDX), X-ray diffraction (XRD), transmission electron microscopy (TEM)) and electrochemical methods (cyclic voltammetry and CO stripping voltammetry) and their activity towards methanol oxidation was tested and commented with respect to the mechanism of methanol oxidation proposed in Chapter 4.

An important parameter in normalizing activities of porous electrocatalysts is real surface area of the catalyst. CO stripping voltammetry was applied for determination of the real surface area of investigated catalysts (Chapter 3). Some difficulties in applying this method were discussed and some solutions were suggested.

In this study the following experimental techniques were used: a) electrochemical measurements: cyclic voltammetry, steady state, chronoamperometric and electrochemical impedance spectroscopy and b) non-electrochemical: EDX, scanning electron microscopy (SEM), XRD and TEM. EDX, SEM, XRD and TEM results were obtained in cooperation with the Max-Planck Institut für Kohlenforschung in Mülheim an der Ruhr.

In order to study the kinetics of methanol oxidation at the membrane electrode assembly (MEA), under technically relevant conditions, a special type of electrochemical cell – a cyclone flow cell (CFC), was used. Compared to classical solutions (rotating disk assembly and fuel cell assembly), the CFC has the advantages of both assemblies, *i.e.* it enables reactant supply through the back diffusion layer like in a fuel cell and it allows real potentiostatic control like in a rotating disk assembly. CFC allows half-cell measurements using a reference electrode with a stable and well defined potential, in contrast to the typical fuel cell set-up, where the influence of the cathode cannot be excluded. Also in contrast to standard half-cell measurements, the reaction occurs at the contact layer between the catalyst particles and the polymer membrane (Nafion[®]) without the influence of anion adsorption from the supporting electrolyte. Since the hydrodynamic conditions are well defined [3] (in a rotating disk assembly the electrode is rotating in a stationary fluid, while in CFC the fluid is rotated over a stationary electrode, but the thickness of the hydrodynamic boundary layers are described in a similar manner) mass transfer limitations can be investigated as well.

2. Experimental

2.1. Electrochemical cell

All measurements were performed in a cyclone flow cell as depicted in Figure 2.1.

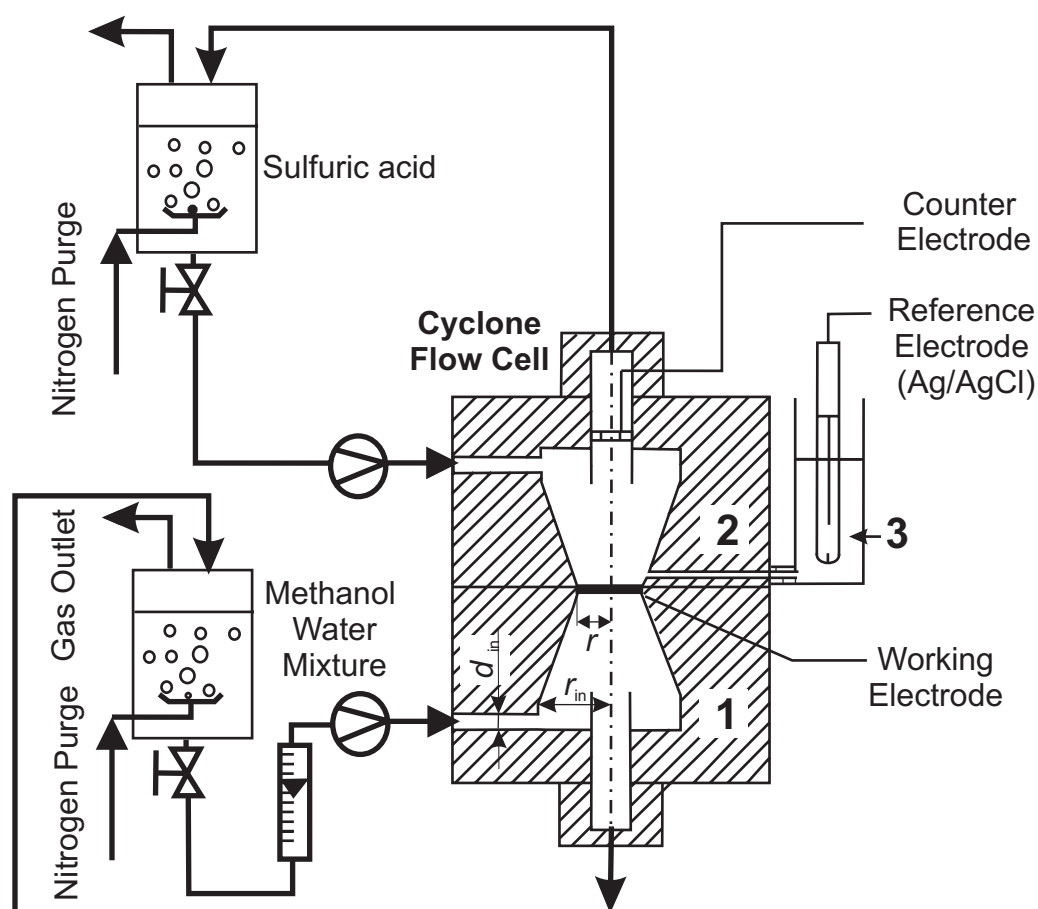


Figure 2.1 Schematic representation of cyclone flow cell.

The cell consists of three compartments: working electrode compartment (1), counter electrode compartment (2) and reference electrode compartment (3). The working electrode compartment is supplied with reactants (water or methanol/water mixture with different methanol concentrations or nitrogen or carbon monoxide in argon), while the counter electrode (2) and the reference electrode (3) compartments are supplied with 1 M sulphuric acid solution. The reference electrode compartment is connected to the counter electrode compartment by a Luggin capillary. Due to the electric current in the liquid layer between the

end of the Luggin capillary and the catalyst layer, the measured working electrode potential has to be corrected for corresponding Ohmic drop (see later).

2.2. Reactants

Electrolyte solutions were prepared from sulphuric acid (Merck, extra pure), methanol (Merck, extra pure) and ultrapure water (Millipore, 18 M Ω cm). Both methanol/water and sulphuric acid containers were deaerated with nitrogen and the deaerated solutions were circulated through the cell. For CO stripping voltammetry 0.1 % CO in Argon (Technische Gase, Westfalen AG, Germany) was used.

2.3. Electrocatalysts

In this study different electrocatalysts were used. They can be divided into two groups: a) commercial catalysts, from Johnson Matthey, UK, and b) non-commercial catalysts prepared at the Max-Planck Institut für Kohlenforschung in Mülheim an der Ruhr. Both commercial and non-commercial catalysts were used as carbon supported and unsupported catalysts. In all cases the nominal PtRu composition was 1:1. Carbon supported catalysts were prepared with 30 *mass* % PtRu on carbon. In the case of non-commercial catalysts carbon support was Vulcan XC-72, while in case of the Johnson Matthey the catalyst support was assigned as carbon black.

Unsupported Johnson Matthey catalyst was designated as HiSpec 6000 and according to the supplier its Brunauer Emmett Teller (BET) surface area was 62.56 m² g⁻¹.

Besides PtRu catalysts, in Chapter 3 an unsupported platinum (Pt) catalyst was used. This catalyst was also supplied by Johnson Matthey. The BET surface area according to the supplier was 26.8 m² g⁻¹.

2.4. Preparation of MEA

All MEAs were prepared in-house. The catalyst ink was prepared by suspending a proper amount of catalyst powder in ultra pure water, with an addition of an aqueous Nafion[®] solution in order to obtain 15 *mass* % of Nafion in the catalyst layer. The suspension was first agitated in an ultrasonic bath for 15 min and then additionally stirred for 3 days. Then the catalyst was sprayed on a Nafion[®] 105 membrane [4]. Details about Nafion[®] 105 membrane pre-treatment are given in reference [4]. The back diffusion layer (BDL) was teflonized Torey[®] paper (type TGP-H-060) or in some experiments teflonized carbon cloth. Carbon

cloth was purchased from ElectroChem, Inc., Woburn, MA 01801. A Teflon content in the BDL was approximately 22 *mass* %. Details about Toray[®] paper pre-treatment are given in reference [5].

The MEA was prepared by hot pressing of the gas diffusion electrode (Nafion[®] membrane and catalyst layer) at 130°C at a pressure of 10 MPa during 3 minutes onto a teflonized BDL. The total geometric area of the MEA covered by the catalyst layer was 12.56 cm².

Typical metal loadings used in this study were:

- 5 mg cm⁻² for unsupported catalysts (both PtRu and Pt)
- 1 mg cm⁻² for supported and unsupported catalysts (only PtRu unsupported catalysts).

2.5. Electrochemical measurements

All electrochemical measurements were carried out with a Zahner impedance measurement unit (IM6e). Experiments were performed in a temperature range from room temperature (22 ± 0.5)°C to 62 ± 0.5 °C. The cell temperature was controlled by use of a Julabo F12 thermostat.

In the following, the standard procedure for electrochemical measurements in this work is described. If there are some differences in regard to this procedure, they will be indicated in the corresponding chapters.

Preconditioning of the membrane electrode assembly (MEA) was done by cyclic voltammetry in the potential range from -0.2 to 0.5 V vs. Ag/AgCl at a sweep rate of 20 mV s⁻¹. Five cycles were enough to obtain a reproducible MEA behaviour. Normally, only the first cycle differs from the subsequent cycles. This procedure was applied prior to steady state, quasi steady state and chronoamperometric experiments.

Steady state experiments were performed potentiostatically with a fixed delay of 5 min at each potential, in the potential range from 0 to 0.5 V vs. Ag/AgCl. The potential step was 25 mV.

Quasi steady state measurements were performed in the same manner as the steady state measurements, but at the sweep rate of 1 mV s⁻¹.

Chronoamperometry. After the preconditioning procedure described above the potential was stopped at the desired set point and the current was recorded over time (30 min in methanol containing solution).

Ohmic drop compensation was done during all these measurements using ohmic resistance values estimated from prior impedance measurements.

Impedance measurements were performed immediately after the chronoamperometric measurement at the same DC potential, over a frequency range between 870 kHz and 10 mHz. The amplitude of the sinusoidal signal was 5 mV (from base to peak).

All potentials were measured and reported versus a saturated silver/silver chloride reference electrode (Ag/AgCl).

2.6. CO stripping voltammetry

After MEA preconditioning (as described above except that N₂ was in the working electrode compartment) CO adsorption was done by flowing 0.1 % CO in Argon (Technische Gase, Westfalen AG, Germany) at a flow rate of 140 ml min⁻¹ through the working electrode compartment, for different adsorption times, while holding electrode potential at 0.0 V vs Ag/AgCl. The gas was then switched to N₂ for 30 min, with a potential still at constant value, to remove CO traces from the gas phase. After 30 min, the potential was scanned from the starting potential to 1.0 V vs. Ag/AgCl and then back to -0.18 V vs Ag/AgCl with a sweep rate of 5 mV s⁻¹.

2.7. Determination of ohmic resistance

As it was mentioned before, prior to other electrochemical measurements the ohmic resistance was determined from impedance spectra. In Figure 2.2 impedance spectra of supported PtRu catalysts¹ in water (a) and 1 M methanol (b) at 60°C are shown. The high frequency region of the impedance spectra (indicated by red arrows in Figure 2.2) is independent on the electrocatalyst tested and it has almost the same value in the presence and in the absence of methanol. This part of the spectra is also independent of potential as shown in Figure 2.2 c. So it was concluded that this resistance is due to the electrolyte resistance, *i.e.* ohmic resistance. As it was mentioned all measurements were corrected for ohmic resistance

¹ For catalyst notation see Appendix II.

determined prior to every measurement during the measurements. The correction was 90 % of the determined value. The difference to 100 % was corrected during data processing.

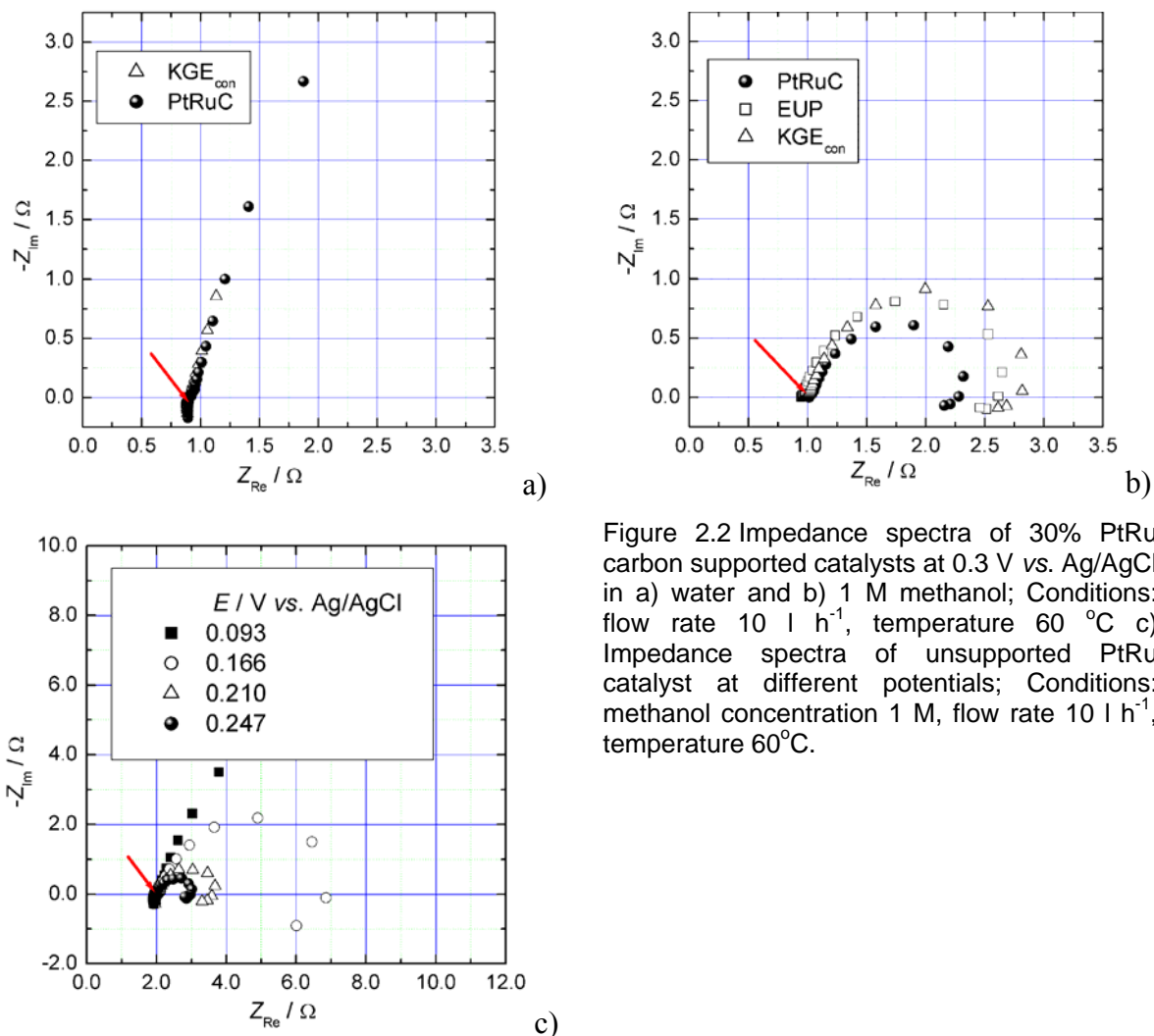


Figure 2.2 Impedance spectra of 30% PtRu carbon supported catalysts at 0.3 V vs. Ag/AgCl in a) water and b) 1 M methanol; Conditions: flow rate 10 l h⁻¹, temperature 60 °C c) Impedance spectra of unsupported PtRu catalyst at different potentials; Conditions: methanol concentration 1 M, flow rate 10 l h⁻¹, temperature 60°C.

2.8. Comparison of steady state and quasi-steady state measurements

In Figure 2.3 comparison between steady state experiments and quasi-steady state experiment is shown. In the steady state experiment current was recorded after 5 min at constant potential. Quasi steady state measurement was performed at constant sweep rate of 1 mV s⁻¹. As can be seen, both approaches give almost the same result. This makes possible to compare activity of an electrocatalyst determined either in a steady state or a quasi steady state experiment.

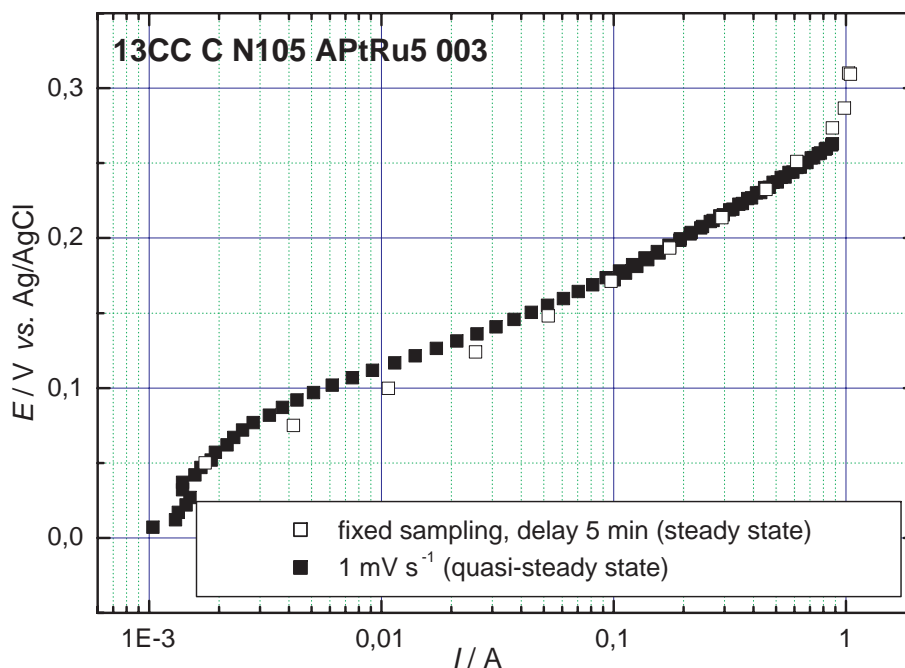


Figure 2.3 Methanol oxidation on unsupported PtRu MEA. Conditions: methanol concentration 3 M, flow rate 10 l h^{-1} , temperature 60°C .

2.9. Determination of geometric surface area

In most of the experiments the total MEA geometric surface area covered by the catalyst layer was 12.56 cm^2 . In the cell (Figure 2.1) the surface area directly exposed to the electrolyte was 2.0 cm^2 (corresponds to surface area of circle with radius $r = 0.8 \text{ cm}$, see Figure 2.1). Due to edge effects the working geometric surface area was bigger than the exposed geometric surface area. Thus, a MEA with a total geometric surface area of 2.0 cm^2 was prepared and compared with the MEA with a total geometric surface area of 12.56 cm^2 . The results are shown in Figure 2.4. Experimentally, the double layer capacitance of MEAs with total geometric surface areas of 2.0 and 12.56 cm^2 was determined from current vs. sweep rate plots using the difference between anodic and cathodic currents at constant potential ($0.15 \text{ V vs. Ag/AgCl}$) in order to eliminate errors due to any occurring faradaic reaction [6]. A value of 0.39 F and 0.59 F for total surface areas of 2.0 and 12.56 cm^2 , respectively were obtained. Since both MEAs are prepared from the same catalyst and with the same metal loading (5 mg cm^{-2}), the difference in the double layer capacitance has to be attributed to the difference in the working geometric surface area. The ratio between double layer capacitances of the MEA with 12.56 cm^2 geometric surface area and the MEA with 2.0 cm^2 geometric surface area was found to be 1.62.

Steady state curves for methanol oxidation of two MEAs with different total geometric surface areas are shown in Figure 2.5.

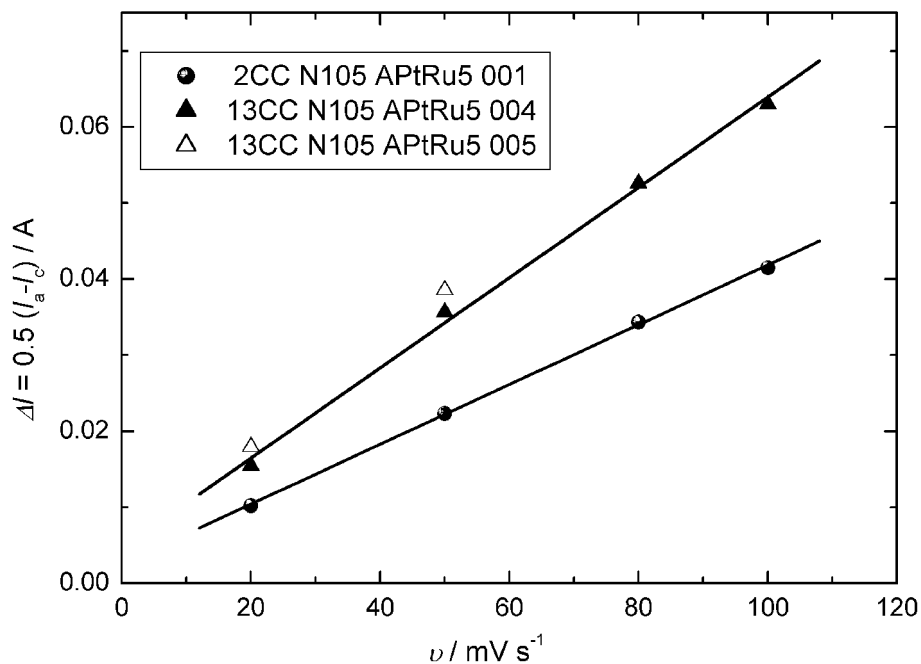


Figure 2.4 Double layer capacitance determination from ΔI vs. sweep rate dependence for three MEAs. Conditions: Water in working electrode compartment; flow rate in working electrode compartment 0 l h^{-1} .

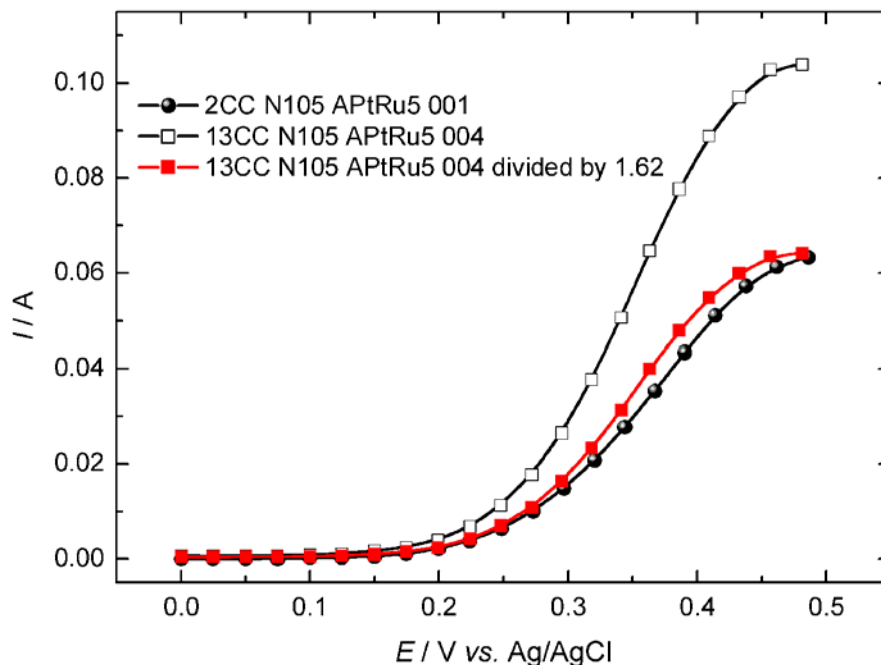


Figure 2.5 Steady state curves for methanol oxidation on two MEAs. Conditions: 1 M methanol in working electrode compartment; room temperature; flow rate in working electrode compartment 10 l h^{-1} .

Currents for an MEA with a total geometric surface area of 12.56 cm^2 are normalized to geometric surface area of 2.0 cm^2 by dividing them by a factor of 1.62 as determined in previous experiments (Figure 2.4). Good agreement between normalized currents for a total geometrical surface area of 12.56 cm^2 and for the MEA with a total geometric surface area of 2.0 cm^2 is obtained. This normalization factor (1.62) was used throughout the whole study wherever the geometric surface area was required.

3. Electrochemical methods for the real surface area determination

In electrochemistry, the term “real surface area” means the electrochemically active surface area under working conditions. Determination of the real surface area is important in order to normalize activities of different electrocatalysts to the same number of reactive surface sites. It is close to the geometric surface area for smooth surfaces with low roughness factors. In this case the current is normalized with respect to the geometric surface area and the normalized activity is expressed as a current density. Technical electrodes do not satisfy these conditions (smooth surface, low roughness factor) due to a necessity to comprise high surface area on low geometrical surface area. So they are porous and with high roughness factors. In this case, activity expressed per geometrical surface area cannot be used in catalyst evaluation because, when comparing two different catalysts, higher current per geometrical surface area can merely mean higher surface area and not higher intrinsic catalyst activity.² Therefore, to evaluate different porous catalysts electric currents should be expressed with respect to the real (active) surface area. For porous electrodes in fuel cells the active surface area refers to the surface area of metal particles, which are at the same time in contact with the electrolyte (in this case Nafion[®]) and the current collector (usually carbon cloth or carbon paper).

In this chapter an attempt is made to evaluate the real surface area of unsupported PtRu catalysts³ in a membrane electrode assembly (MEA) under fuel cell relevant conditions. For the surface area determination CO stripping voltammetry *i.e.* the CO adsorption method, was used. This method is based on several assumptions therefore a system characterization with an unsupported Pt catalyst as a test system was carried out. One of the assumptions is that the CO saturated coverage on PtRu is the same as on pure Pt catalyst. To calculate the Pt-CO saturated coverage at Pt, at first a total number of reactive surface sites on Pt was determined by using the hydrogen adsorption method. So here, both the CO and the hydrogen adsorption

² For porous electrodes, activity can be expressed per catalyst loading as well, *i.e.* per mass of catalyst. This parameter is good in terms of price of the catalyst *i.e.* higher activity per mass of the catalyst does mean better efficiency of catalyst, but does not give an answer in regard to the catalyst intrinsic activity.

³ In Chapter 5 the same method will be applied to supported PtRu catalysts.

method will be described. They are based on adsorption of a probe molecule, followed by electrochemical stripping of the adsorbed molecule and determination of the charge exchanged during the process. The **hydrogen adsorption method** uses charge in the potential region where molecular hydrogen is adsorbed. Hydrogen adsorption/desorption region is usually referred to as “underpotential”⁴ hydrogen adsorption region due to the fact that a layer of adsorbed hydrogen atoms is formed on the surface before the reversible potential for hydrogen evolution is reached. Later the **carbon monoxide adsorption method** will be described.

3.1. Hydrogen adsorption method

The hydrogen adsorption method cannot be generally applied to the real surface area determination, but only for those surfaces where hydrogen is “underpotentially” adsorbed (for example platinum and other platinum group metals, like Rh and Ir). At first, assumptions and limitations of the method will be discussed.

In cyclic voltammetry the region of “underpotential” hydrogen adsorption is characterized by different peaks, which depend on the type of solution, the surface preparation and the exposed crystallographic plane. On polycrystalline platinum in acidic solutions usually two adsorption peaks will be observed (depending on the sweep rate and the present anions) [6]. Two peaks at different potentials represent different adsorption energies of hydrogen adsorption *i.e.* they reflect the surface inhomogeneity and the interaction with immediate species (anions and other H species). Unlike polycrystalline surface, single crystal surfaces are homogenous and under ideal conditions only one peak for hydrogen adsorption should be seen. In Figure 3.1, cyclic voltammograms of three low index single crystal planes in acid medium are shown. As can be seen on Pt(110) and Pt(100) single crystal planes, there is one dominate peak of hydrogen adsorption, while a Pt(111) single crystal plane is more or less featureless. Therefore it can be approximated that two adsorption peaks in the hydrogen region on polycrystalline platinum correspond to hydrogen adsorption on Pt(110) and Pt(100) single crystal faces. So, polycrystalline platinum can be considered as a mix of single crystal planes and defects at the surface.

⁴ When using the term “underpotential” one should keep in mind that underpotential does not exist from a thermodynamical point of view and that in this case hydrogen adsorption is “underpotential” only with regard to the potential of hydrogen evolution for reaction $2\text{H}^+ + 2\text{e}^- = \text{H}_2$. More accurate would be to use the reversible potential for reaction $\text{H}^+ + \text{e}^- = \text{H}_{\text{ads}}$.

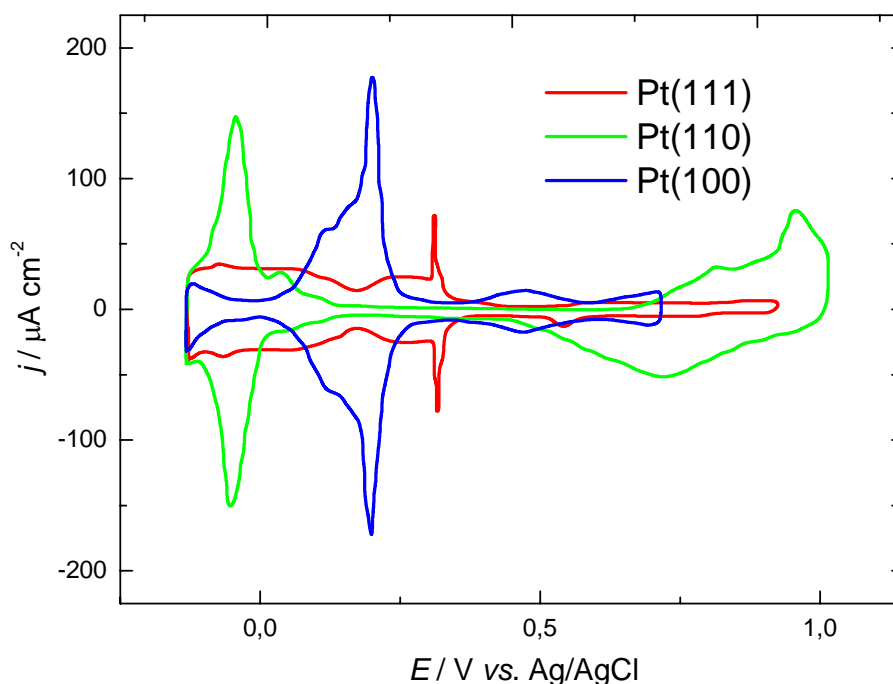


Figure 3.1 Cyclic voltammograms of Pt low index single crystal planes in 0.1 M H₂SO₄. Sweep rate 50 mV s⁻¹. Adopted from reference [7].

Three major assumptions of the method are: 1) the potential at which hydrogen forms a monolayer on the surface is at the onset of hydrogen evolution, 2) the ratio between adsorbed hydrogen and platinum atoms is one to one, and 3) that polycrystalline surface is a mix of single crystal planes with some arbitrary distribution of different single crystal planes in it [8].

From the experimental point of view, it is important to determine the exact potential where a hydrogen monolayer is formed. Although this was a topic of many studies, some uncertainties are still present [8]. One practical approach is described in Figure 3.2. Here instead to look at the exact potential where the hydrogen monolayer is formed, the end-point potential was proposed so that any charge required to complete the hydrogen monolayer at a potential more negative than the end-point potential (yellow colored area in Figure 3.2) is compensated by the contribution from the hydrogen evolution at potentials more positive than the end-point potential (blue colored area in Figure 3.2).

Based on the adsorption isotherms, the hydrogen coverage at the end-point potential is determined to be 0.77 of a monolayer. So a suggestion is to use the potential fixed at 0.08 V vs. RHE as an end-point potential and to consider hydrogen coverage as being 0.77.

The assumption that the ratio between adsorbed hydrogen and platinum atoms is one is experimentally validated only for Pt(100) single crystal planes [9]. For other planes (Pt (111)

[10] and Pt (110) [11]) a contribution of multibonded hydrogen or hydrogen bonded to the underlying layers of platinum atoms is probable. This should be taken as a factor of uncertainty for polycrystalline surfaces. In the case of Pt nanoparticles the influence of hydrogen bonding to underlying Pt layers on Pt nanoparticles can be expected as well. All these factors will lead to surface area overestimation and should be kept in mind.

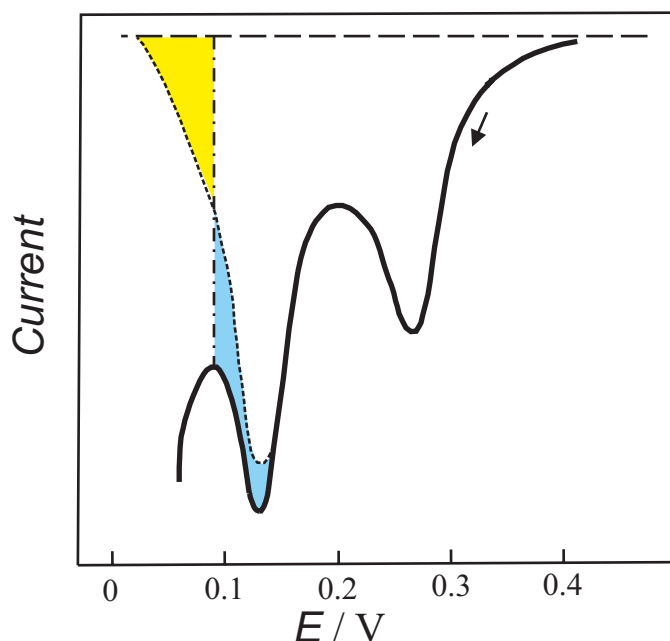


Figure 3.2 Schematic cathodic part of the hydrogen adsorption region of polycrystalline platinum electrode in diluted sulfuric acid solution. The symbols are: solid line - total current; dashed line - double layer charging current; dotted line – total current without influence of hydrogen evolution; dot-dash line – end-point potential. (Adopted from reference [8]).

The distribution of different planes in a polycrystalline surface, also influences the value of charge exchanged. For polycrystalline platinum surface the charge exchanged for one hydrogen atom per platinum atom is assumed to be $210 \mu\text{C cm}^{-2}$. This is a mean value and lies between typical values for single crystal surfaces (for Pt (111) this value is $241 \mu\text{C cm}^{-2}$, for Pt (100) is $209 \mu\text{C cm}^{-2}$ and Pt (110) $200 \mu\text{C cm}^{-2}$)⁵ [8]. Polycrystalline surface is considered to consist mainly of Pt(110) and Pt(100) single crystal plane contributions, while the contribution of Pt(111) crystal plane is less pronounced. Pt nanoparticles have the face centered cubic (f.c.c) structure of Pt and a lattice constant of 0.3927 nm, which is identical to bulk platinum. The surface of the particles is considered to have icosahedral structure with

⁵ These are measured values and they differ from calculated values. For example, for Pt(100) surface the measured value ($209 \mu\text{C cm}^{-2}$) is higher than the calculated value for a hydrogen monolayer considering one hydrogen atom per platinum atom ($147 \mu\text{C cm}^{-2}$) which implies the contribution of hydrogen bonded to the underlying layer of platinum atoms of the (110) plane.

(111) faces exposed [12]. According to these authors icosahedral structure is thermodynamically more stable than the cubo-octahedron structure also suggested by some authors as in reference [13]. According to the latter authors [13] Pt nanoparticles have a cubo-octahedral structure with 100 and 111 single crystal planes exposed. Also contributions of low-coordinated Pt edges and corner atoms are significant (due to the small particle size (between 2-6 nm) the number of surface atoms is large (for example if the particle size is 2 nm the number of surface atoms per total number of atoms in particle is 50 % (when particle size is increasing, the part of surface atoms is decreasing)). A large fraction of surface atoms gives lower Pt-Pt coordination number than for bulk platinum (for example if the particle size is 2 nm, Pt-Pt coordination number is 9.5 while for bulk platinum it is 12), so the contribution of edges and corner atoms is decreasing with increasing particle size. It can be expected that the distribution of single crystal planes in Pt nanoparticles is in a similar manner uncertain as in the case of polycrystalline platinum.

The same problems encountered in the determination of the exchanged charge for nearly a hydrogen monolayer on polycrystalline platinum are true for platinum nanoparticles as well. With the similar level of uncertainty the value of $210 \mu\text{C cm}^{-2}$ used for polycrystalline platinum as a measure of exchanged charge for nearly a hydrogen monolayer, can be accepted for platinum nanoparticles as well and that was done in the following section.

3.1.1. Experimental approach

The method is based on the determination of the amount of charge to remove the adsorbed full hydrogen monolayer. Experimentally this is done by applying cyclic voltammetry to obtain current-potential curves for adsorption and desorption of hydrogen monolayers. The integration of current in the anodic scan gives the amount of hydrogen desorbed according to the following reaction:



The experimentally obtained charge contains also a contribution due to the double layer charging, which should be subtracted. Subtraction is usually made by assuming that double layer charging is the same as in the double layer region.

$$Q_{\text{H}} = \frac{1}{\nu} \int_{-0.115}^{0.220} (I - I_{\text{dl}}) dE \quad (3.2)$$

where Q_H is the charge, I is the total current, I_{dl} the double layer current, E is the potential (V vs. Ag/AgCl) and v the sweep rate.

The electrochemical measurements were performed in a cyclone flow cell (Chapter 2). The working electrode compartment was supplied with N_2 , while counter and reference electrode compartment were fed with 1 M sulfuric acid solution. The catalyst was a Johnson Matthey unsupported platinum catalyst. At first the MEA was conditioned by potential cycling in the potential region between hydrogen and oxygen evolution (from -0.15 to 1.25 V vs. Ag/AgCl) with a sweep rate of 50 mV s^{-1} in N_2 atmosphere. Then, CO was adsorbed (see details later) and swept from the surface. For surface area determination by the hydrogen adsorption method a second voltammogram after CO stripping was used.

Now the method will be demonstrated for surface area determination of an unsupported platinum electrode.

3.1.2. Determination of real surface area of unsupported Pt catalyst

As it was mentioned before, the total number of reactive surface sites on platinum can be determined by the hydrogen adsorption method. The cyclic voltammogram of a Pt-MEA is shown in Figure 3.4

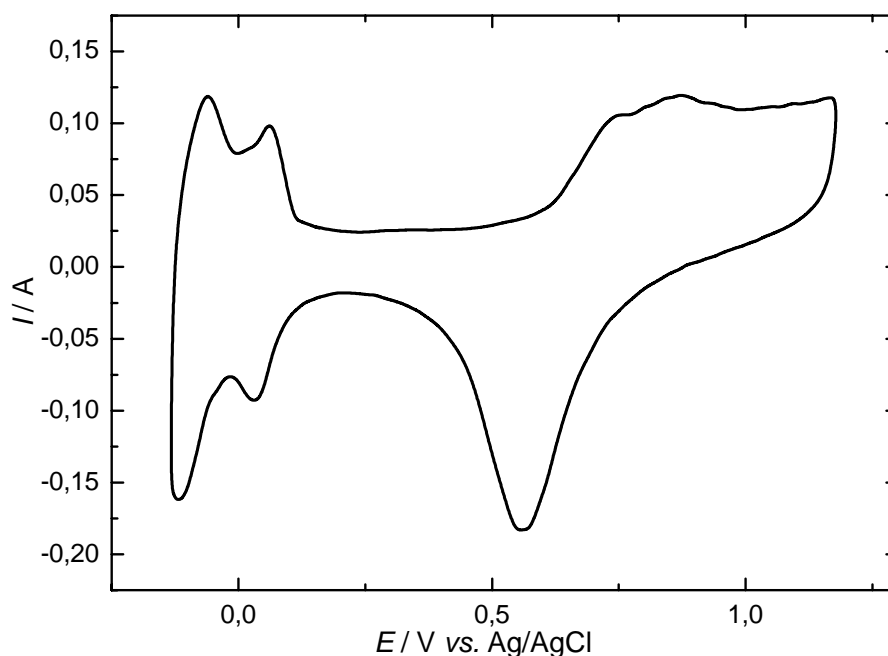


Figure 3.3 Cyclic voltammogram of unsupported Pt MEA at a sweep rate of 50 mV s^{-1} . Conditions: N_2 in working electrode compartment and 1M H_2SO_4 in counter electrode compartment, room temperature.

The Pt MEA cyclic voltammetry behavior is in good agreement with the literature results for polycrystalline platinum in acidic medium [6]. It was mentioned before that two peaks observed in the CV image of polycrystalline platinum can be assigned to hydrogen adsorption on 100 and 110 single crystal planes while hydrogen adsorption on 111 single crystal plane is featureless (Figure 3.1). Similar, hydrogen adsorption/desorption region on Pt nanoparticles (from -0.13 to 0.24 V vs. Ag/AgCl in Figure 3.3) can be rationalized with regard to single crystal plane contributions as shown in reference [13]. If Pt nanoparticles have cubo-octahedral structure with 100 and 111 single crystal planes exposed, the hydrogen CV image will be mainly governed by the 100 plane, because the 111 single crystal planes is featureless [13]. The presence of the 110 single crystal planes can be rationalized by the contribution of low-coordinated Pt edges and corner atoms. In our study the particle size is about 6 nm (determined from the BET surface area) and such large particles behave almost as polycrystalline platinum. According to reference [12] for a particle size of 6 nm the ratio of surface atoms to total atoms is 0.2. For comparison in reference [13] particle size was 3.7 nm and number of surface atoms was calculated to be 30 %, which corresponds to the Pt-Pt coordination number of 11.2 what is close to 12 (the Pt-Pt coordination number for polycrystalline platinum).

Integration limits are chosen in agreement with reference [8] as discussed above. It was assumed that the hydrogen coverage at the end-point potential is 0.77 of a monolayer [8]. The charge required for hydrogen adsorption is calculated (0.363 C) and the value was used in real surface area determination. Correction for double layer charging was done as shown in Figure 3.4. The surface area S in cm^2 was determined as follows:

$$S = \frac{Q_H}{\theta_H \cdot 0.210 \text{ mC cm}^{-2}} \quad (3.3)$$

where Q_H is charge in mC, 0.210 mC cm^{-2} corresponds to a monolayer of adsorbed hydrogen and θ_H is the hydrogen monolayer coverage at end-point potential (0.77) [8].

The calculated Pt-MEA real surface area is $2.2 \times 10^3 \text{ cm}^2$. The specific surface area⁶ was also calculated and the obtained value is $13.5 \text{ m}^2 \text{ g}^{-1}$. As it was mentioned before, the

⁶ Under our experimental conditions the total geometric surface area of MEA was 12.56 cm^2 , while the surface area directly exposed to the electrolyte was 2.0 cm^2 . Some edge effect was encountered and in an independent measurement with a total geometric surface area of 2.0 cm^2 a factor of 1.62 was obtained (Chapter 2). So in specific surface area calculations the value of 3.24 cm^2 for geometric surface area was taken.

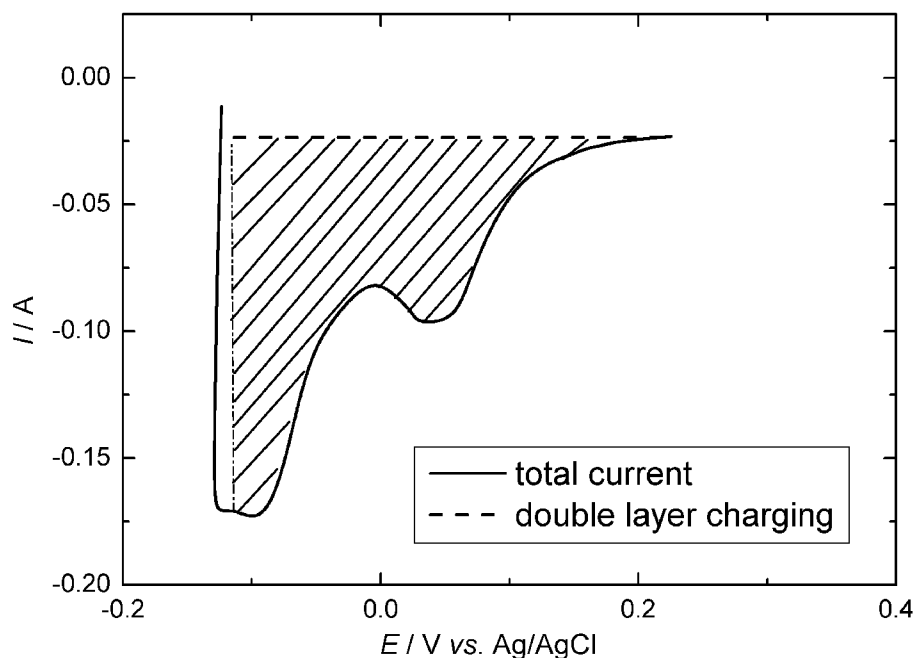


Figure 3.4 Cathodic part of the hydrogen adsorption region of unsupported Pt MEA at a sweep rate of 50 mV s^{-1} . Conditions: N_2 in working electrode compartment, room temperature. Dash-dot line represents lower integration limit.

BET surface area is $26.8 \text{ m}^2 \text{ g}^{-1}$ which means that approximately 40 % of the BET surface area is active under these conditions. Lower surface area under operating conditions than the BET surface area is not surprising and several reasons can be discussed. First, during the ink preparation some particle agglomeration can occur. Second, catalyst particles are wrapped in Nafion and as it was shown before on an example of a smooth platinum electrode, the Nafion film decreases active surface area [14]. Third, in order to realize electronic conductivity, catalyst particles should be connected to each other and to the current collector which will also decrease the available surface area. It can be concluded that only particles, which are connected to both electrolyte and current collector, will contribute to the real surface area.

3.2. CO adsorption method

After the total number of reactive surface sites on Pt MEA was determined by the hydrogen adsorption method, the charge required to oxidize the saturated CO layer on a Pt-MEA was determined from the CO adsorption method and then the saturated CO coverage, that will be later used for surface area determination of supported and unsupported PtRu catalysts, was calculated. But, before going further a few words about CO adsorption method will be addressed.

Basically the CO adsorption method is the same as the hydrogen adsorption method *i.e.* a probe molecule is adsorbed at the surface (at potential where CO oxidation does not occur),

removed from the surface in a potential sweep and then the charge under the oxidation peak is calculated. This method should have some advantages over the hydrogen adsorption method due to its more general applicability⁷. However, many limitations of the method are encountered and will be shortly discussed.

The first uncertainty is connected to the kind of CO bonding at the surface. For example at polycrystalline platinum at least two bonding types (on-top and bridge bonding CO)⁸ are observed [15]. Information about CO bonding is valuable in determining a number of CO atoms per metal atom. For example if CO is on-top bonded, then two electrons will be exchanged per surface site in CO oxidation while for bridge bonded CO, only 1 electron per surface site. Information about the kind of CO bonding on the electrode surface can be obtained from spectroscopy methods (for example Fourier Transform Infra Red (FTIR)) and from scanning electron microscopy (STM), but they are mostly limited to smooth, well-defined surfaces (single crystal electrodes) and high-vacuum studies which are usually not relevant for the electrode surface under real experimental conditions. Recent voltammetric studies have shown that the number of CO molecules per one platinum atom is one and that the CO saturated layer is 90 % of one monolayer [8].⁹

The second uncertainty is CO charge correction in respect to other contributions like double layer charging and charging due to metal oxide formation. The simplest way for the double layer charging correction is, like in the hydrogen adsorption method, to consider that double layer charging is identical as in the absence of the adsorbate (for more rigorous treatments of this problem see reference [8]). The more significant problem is the determination of a charge due to metal oxide formation. This is especially true for less noble metal electrodes like Ru and also Ru alloys like PtRu. In the case of the pure platinum electrode the problem is not so significant since CO oxidation on platinum does not overlap to a great extent with oxide formation on platinum, while in the case of PtRu alloy due to early commence of oxide formation¹⁰, the overlap is significant (for example, the charge to remove a monolayer of adsorbed CO on polycrystalline Ru electrode was determined to be

⁷ The CO adsorption method can be used in many metals and alloys, since CO can be adsorbed in a stable form at practically almost all d-metals.

⁸ Other types of CO bonding are also possible and depend on the nature of metallic surface and defect density.

⁹ This was obtained by comparing the charge from hydrogen and CO adsorption on the same surface and other same conditions.

¹⁰ On PtRu oxide, formation already starts in the “hydrogen region” which is an advantage concerning methanol electrocatalysis, but in this case an obvious disadvantage.

0.550 mC cm⁻² giving a coverage degree higher than 1.0 [16]). A practical approach to problem solution is to consider the oxide formation, being the same with and without CO adsorbed layer. In this case subtraction for additional charge due to oxide formation is the same as subtraction for double layer charging (usually, as a base line is considered line from a second cycle after CO stripping in the same experiment). But, as it was mentioned before, charge due to oxide layer formation can be underestimated in this way, as it was shown in the example with polycrystalline Ru and in a recent study by Jusys *et al.* [17] (see below).

Besides by cyclic voltammetry, the CO charge can be determined by some other methods like IR (Infra-Red) or DEMS (Differential Electrochemical Mass Spectroscopy). A major advantage of these methods over voltametric CO charge determination is their independence on all faradaic and non-faradaic contributions, which have to be subtracted in voltammetric charge determination. But there are some disadvantages.

Using IR spectroscopy, CO coverage on single crystal surfaces is easy to determine, since the surface atomic density is known. For practical electrodes situation it is not so defined due to distribution of surface planes on polycrystalline surface and on dispersed electrodes situation is even less clear. The limitation of the method is that the electrode should possess the necessary reflectivity, which usually is not the case with technical fuel cell electrodes. So far this method was applied to the investigation of dispersed catalysts but only when a dispersed catalyst was supported on IR reflective surface (like highly oriented pyrolytic graphite or gold as a substrate).

More promising, concerning application under technical fuel cell conditions is DEMS. The method is based on the detection of the product by means of a mass spectroscopic technique, which is not affected by the faradaic proportion of the total charge. Calibration is usually made by using porous polycrystalline platinum electrode where it is possible to determine the total number of atoms for CO adsorption (from hydrogen adsorption method) and then to relate it to the total number of sites occupied by CO with the area determined by the adsorbed hydrogen. In a recent contribution by Jusys *et al.* [17] the active surface area of different ternary unsupported catalysts was determined by the means of CO stripping (oxidation of pre-adsorbed saturated CO layer). First calibration was done by CO monolayer oxidation on a smooth polycrystalline platinum electrode. The hydrogen adsorption method¹¹

¹¹ An adsorption charge of 0.210 mC cm⁻² for a full hydrogen monolayer and a hydrogen coverage at the onset of H₂ evolution of 0.77 are assumed.

was used in order to determine the total number of Pt atoms being available for CO adsorption. By comparing the charge from hydrogen adsorption and from CO stripping, the CO surface coverage was determined. In the next step, the CO charge was determined by integrating the mass spectrometric current above the ground level of the $m/z = 44$ signal. This charge was assumed to correspond to the real surface area of the Pt electrode determined by the hydrogen adsorption method. The method is then applied to the surface area determination for unsupported high surface area PtRu catalysts (the assumption was made that the coverage of the saturated CO layer on the metallic parts of the PtRu catalysts is the same as on the smooth polycrystalline Pt). It was shown that the charge obtained from voltammetric CO stripping is about 50 % higher than obtained from the mass spectroscopic current. The difference is ascribed to large and poorly defined faradaic and non-faradaic contributions in the CO voltammetric charge. This result is in accordance with the result for polycrystalline Ru electrodes where the CO surface coverage determined by CV was higher than 1 [16]. The CO stripping surface area obtained by using DEMS was compared with the BET surface area and found to be much lower (for example for PtRu catalyst obtained from E-TEK about 50 % of BET surface area). This ratio was even lower for ternary catalysts. Deviation was taken as an indication that a certain part of the catalyst surface consists of metal oxides¹².

In a study by de Souza *et al.* [18], the CO adsorption method was used for the surface area evaluation of several PtRu catalysts. The CO stripping charge was determined by cyclic voltammetry, DEMS and IR spectroscopy and used to normalize, three reaction rate dependent parameters in methanol oxidation (oxidation current in cyclic voltammetry, formation of CO₂ as measured *via* on line mass spectrometry and *in situ* FTIR spectroscopy). So, using CO stripping as a normalization tool, all methods yielded reasonable agreement of catalysts activity with respect to methanol oxidation.

Dinh *et al.* [19] used the voltammetrically obtained CO charge to normalize activity of three unsupported PtRu catalysts (Johnson Matthey, as received). They obtained that 50 % of the BET surface area was PtRu metal alloy of composition near to 1:1.

Other authors [20] reported for the same Johnson Matthey unsupported catalyst that 80 % of the BET surface area was electrochemically active. These results are obtained for CO stripping at elevated temperature (60 °C), PtRu loading of 4 mg cm⁻² (in former case 5 mg

¹² CO adsorption occurs on metallic surface but cannot take place on oxide-covered surface.

cm⁻²) and for a conditioned catalyst¹³, which can explain the very high catalyst utilization rate.¹⁴

To summarize, many uncertainties are connected to the voltammetric CO stripping charge determination, first due to unknown CO bonding at the surface and second due to undefined non-faradaic and other faradaic charge contributions. Determination of the CO charge based only on voltammetric determination has a more qualitative character, but still enables the comparison of different catalysts' activities (as it was shown in [18] by comparing this method with other methods like DEMS and IR spectroscopy).

3.2.1. Experimental approach

As in the hydrogen adsorption method, the CO adsorption method is based on the determination of the amount of charge to remove the adsorbed saturated CO monolayer. Experimentally this is done by adsorbing CO at an electric potential where no CO oxidation will occur (usually in the hydrogen adsorption/desorption region or at the end of this region) for a certain time, purging the system with an inert gas and applying cyclic voltammetry to obtain the current-potential curve for CO oxidation. Then, the integration of the current in the anodic scan gives the amount of CO oxidized:



The experimentally obtained charge also contains contributions due to the double layer charging and simultaneous oxide formation. Difficulties in accurate double layer and oxide formation charge subtraction (especially for electrodes with early oxide formation commencement) were already discussed. Here two approaches for base line subtraction were tested. In a first approach the base line subtraction was done as in hydrogen adsorption method, *i.e.* with an assumption that double layer charging and oxide formation are the same with and without CO adsorbate. The first cycle after the CO adsorption was integrated, and then the same was done with a second cycle and afterwards subtraction was made. The second approach requires a new base line, which is then subtracted from the CO stripping line and then the area under subtracted CO stripping line is integrated (for more details see later).

¹³ Usually, conditioning is done under humidified H₂ atmosphere where PtRu serves as a hydrogen oxidation reaction catalyst (the aim is to reduce surface of the as-received catalyst [19] and in that way to increase number of available seats for methanol adsorption and oxidation).

¹⁴ Progressive reduction of the catalyst surface was observed at the elevated temperatures [19].

The method will be demonstrated on the surface area determination of *unsupported Pt* and *PtRu catalysts*. As it was said before, the unsupported Pt catalyst was used as a kind of test system for the determination of CO saturated surface coverage, while a main goal was the determination of the surface area of unsupported and supported PtRu catalysts (see also Chapter 5).

Details for MEA's preparation, and cell details are the same as for other measurements in the here used cyclone flow cell configuration. Metal loading was 5 mg cm^{-2} for both unsupported Pt and PtRu catalysts.

CO adsorption was carried out as described in Chapter 2. In addition in experiments performed in this Chapter the potential of CO adsorption was varied (in most of the experiments the potential was $0.0 \text{ V vs. Ag/AgCl}$, and in some cases $-0.1 \text{ V vs. Ag/AgCl}$). Positive potential limit was also varied (from 0.45 up to $1.05 \text{ V vs. Ag/AgCl}$) and a sweep rate (usually was 5 mV s^{-1} but in some experiments was $10, 20$ or 50 mV s^{-1}).

3.2.2. Unsupported Pt catalyst

Figure 3.5 shows a stripping scan for adsorbed CO on unsupported Pt catalyst. CO was adsorbed at $0.0 \text{ V vs. Ag/AgCl}$ for 30 min. The CO stripping peak potential is at $0.536 \text{ V vs. Ag/AgCl}$. The value reported in Gasteiger *et al.* [16] study, for a smooth, bulk Pt electrode equilibrated at 1 atm CO is $0.583 \text{ V vs. Ag/AgCl}$. The value found in the present work is about 50 mV more negative. A similar effect was observed during methanol oxidation where the onset of methanol oxidation on Pt nanoparticles was 50 mV more negative compared to smooth bulk polycrystalline electrode [14]. The effect can be rationalized in terms of a higher Pt particle affinity to OH adsorption what in turn increases the rate of CO oxidation. It is similar to PtRu catalyst where Ru donates OH species and significantly increases the rate of methanol oxidation. Dinh *et al.* [19] in a similar study obtained for the same Pt catalyst as in this study a CO peak potential of $0.583 \text{ V vs. Ag/AgCl}$ (the same value as in H. Gasteiger *et al.* [16]). The observed difference in this case can be due to a different experimental set-up (in our case real potentiostatic control was achieved using a reference electrode with a stable and well-defined potential while in the case of the cited work the counter electrode was used at the same time as a reference electrode).

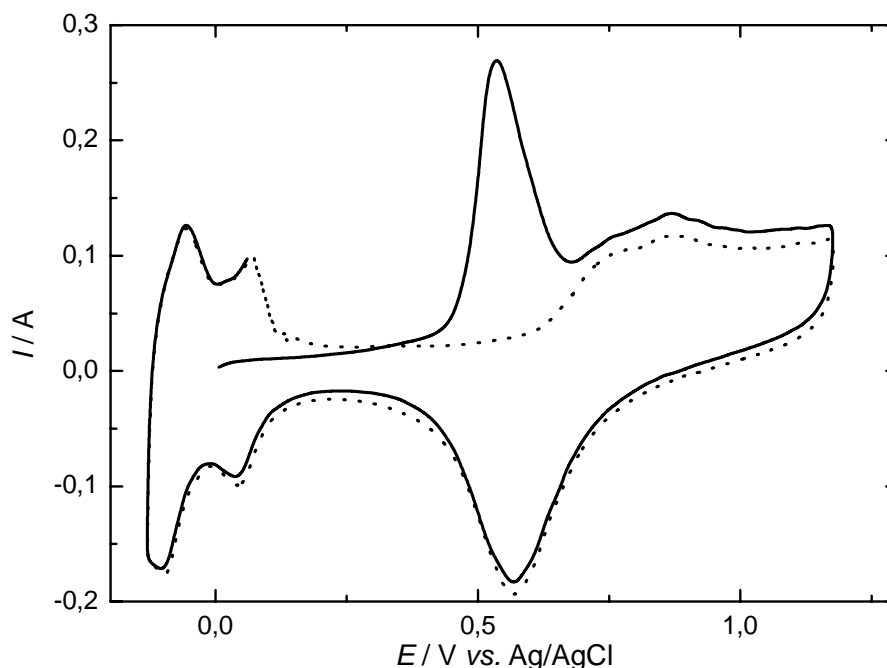


Figure 3.5 Cyclic voltammograms of unsupported Pt MEA for CO stripping. Dashed line: after CO removal. Conditions: CO adsorption at 0 V vs. Ag/AgCl, adsorption time 30 min, sweep rate 50 mV s⁻¹.

The simplest approach for a base line subtraction is to consider double layer charging and oxide formation the same as in the absence of CO, *i.e.* to use the second cycle in the same experiment for base line subtraction and to contribute the difference between the first and the second cycle only to CO oxidation. So the area under the CO stripping peak in the potential region from 0.325 V to 1.2 V vs. Ag/AgCl in a first positive going sweep and from 1.2 to -0.126 V vs. Ag/AgCl in a first negative going sweep, was calculated and corrected for the area obtained after integration under the curve registered during the second cycle in the same potential region. The obtained charge was 1.04 C. The CO surface area S_{CO} in cm² was determined as follows:

$$S_{CO} = \frac{Q_{CO}}{0.420 \text{ mC cm}^{-2}} \quad (3.5)$$

where Q_{CO} is CO stripping charge (in mC) determined after 30 min of CO adsorption, and 0.420 mC cm⁻² corresponds to a monolayer of adsorbed CO. The CO surface area calculated from equation (3.5) is 2.5 x 10³ cm². This value is higher than the surface area determined from the hydrogen adsorption method and it was assumed that the hydrogen adsorption method gives the maximum number of surface reactive sites. Thus, the CO stripping curve was re-examined and it was noticed that a large contribution to the final CO stripping charge is given by a charge in the potential region from 0.8 to 1.2 V vs. Ag/AgCl, the so called O-

region. This charge can be attributed to CO oxidation, but also to oxidation of impurities being adsorbed during CO adsorption or to the difference in oxide formation on a surface preconditioned in a different way (by prolonged reduction at constant potential (correspond to first cycle after CO adsorption) or by potential cycling (correspond to second cycle after CO adsorption)). In a blind experiment (Figure 3.6), performed under the same conditions as the CO stripping experiment, except in absence of CO, the difference between the first and the second cycle was also observed. Based on this experiment some adsorption of impurities can not be completely excluded (see hydrogen region in Figure 3.6 where a small suppression of the hydrogen desorption peak is observed compared to the second cycle), but also some changes in oxide formation are possible. The similar effect was observed on polycrystalline platinum [21]. Also, de Souza *et al.* [18], registered some differences in O-region between first and second cycle, but no online CO₂ mass signal was detected in the same potential region. It was concluded that the difference observed in the O-region is more likely due to oxidation of impurities or some differences in oxide formation than due to CO oxidation.

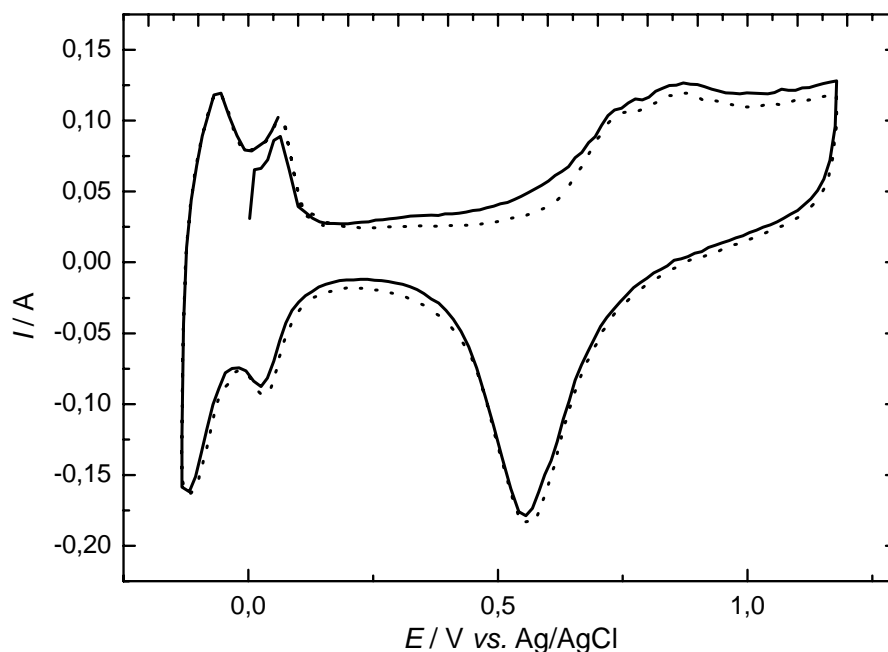


Figure 3.6 Cyclic voltammograms of Pt MEA in N₂. First cycle full line, second cycle dash line. Conditions: delay at 0.0 V vs. Ag/AgCl 45 min, sweep rate 50 mV s⁻¹, flow rate in working electrode compartment 120 ml min⁻¹, room temperature.

Now the integration was made within the new integration limits from 0.326 V to 0.674 V vs. Ag/AgCl (O-region is excluded) and the values of 0.629 C for CO stripping charge and 1.5×10^3 cm² for CO surface area were obtained. The CO saturated coverage was calculated by the following equation:

$$\theta_{\text{CO}}^{\text{sat}} = \frac{S_{\text{CO}}}{S} \quad (3.6)$$

where S_{CO} is the CO surface area (equation (3.5)) and S is the surface area determined by the hydrogen adsorption method (equation (3.3)). The value obtained is $\theta_{\text{CO}}^{\text{sat}} = 0.680$. This value is in good agreement with a CO coverage factor determined on polycrystalline platinum surface [17] and on single crystal platinum surface (Pt(111)) [22].

CO adsorption was performed at different adsorption times in order to check when the saturated CO coverage is achieved (Figure 3.7).

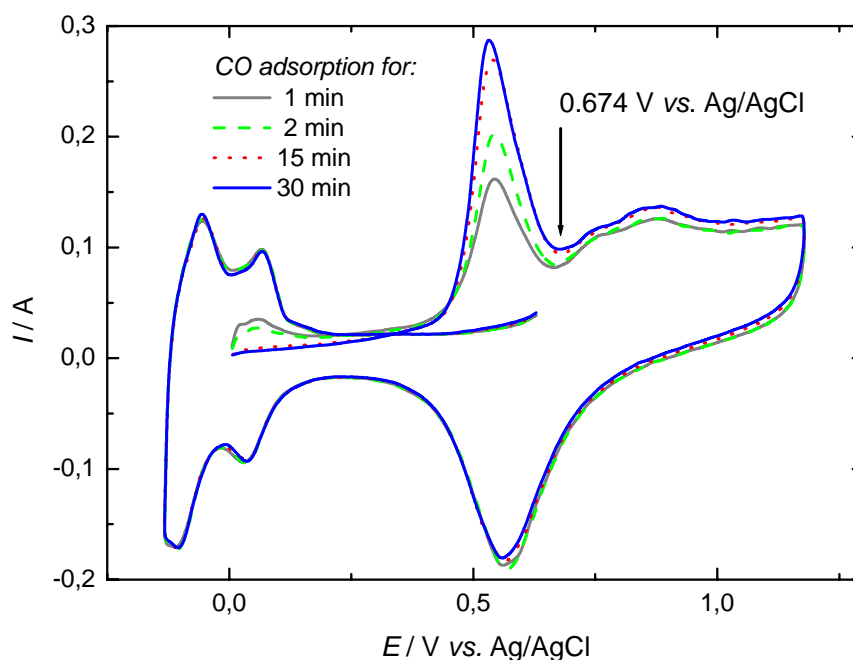


Figure 3.7 CO stripping voltammetry of unsupported Pt MEA after CO adsorption at 0 V vs. Ag/AgCl for different adsorption times. During CO stripping N_2 in working electrode compartment (flow rate 120 ml min^{-1}). Sweep rate 50 mV s^{-1} . Room temperature.

Evidence for saturation coverage of the electrode surface with adsorbed CO is the complete blocking of the pseudo capacitive currents in the potential region below 0.2 V vs. Ag/AgCl (Figure 3.7) [16]. A high CO coverage is obtained even after 1 min of CO adsorption and after 15 min saturated CO monolayer is formed. The difference in the charge obtained after 30 min of CO adsorption is almost in the region of experimental error. Currents observed in the O-region are not due to oxidation of adsorbed CO but are related to other processes, as discussed before.

The CO stripping charge as a function of adsorption time at constant adsorption potential is shown in Figure 3.8. As discussed, the CO saturated monolayer is formed almost after 15 min of adsorption.

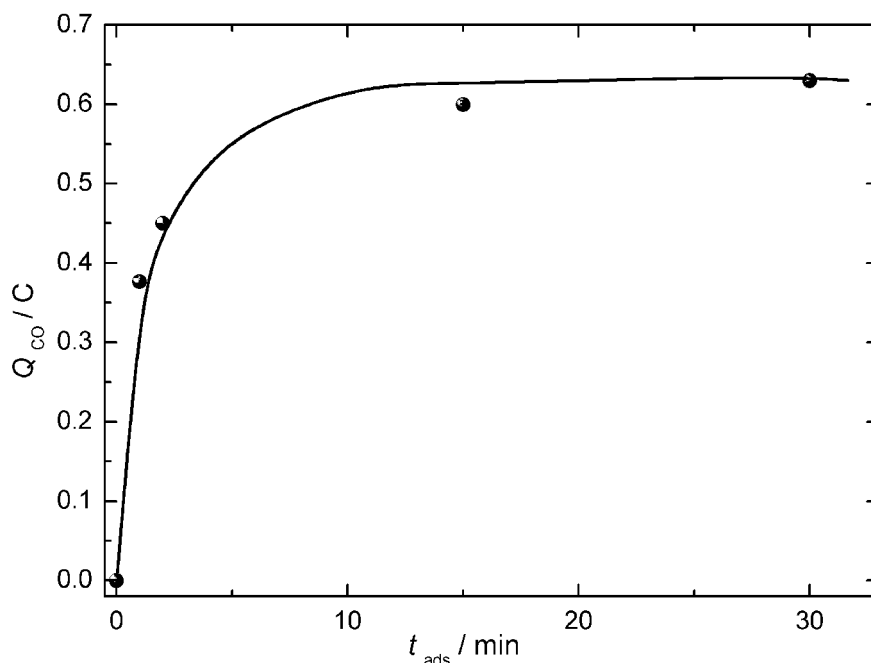


Figure 3.8 CO stripping charge for unsupported Pt MEA as a function of time of CO adsorption. The adsorption potential was 0.0. V vs. Ag/AgCl. Sweep rate 50 mV s⁻¹. Room temperature.

3.2.3. Unsupported PtRu catalyst

It was already mentioned that the voltammetric determination of CO charge on a PtRu catalyst is connected with many uncertainties. The major one is the accurate determination of double layer charging and Faradaic charging due to oxide formation. However, although voltammetric determination of CO charge does not yield the real surface area, it can be used as a good parameter for surface area normalization in comparing activities of different catalysts as it was shown in reference [18]. Now results obtained for unsupported PtRu catalysts will be discussed.

CO stripping voltammetry of unsupported Pt and PtRu catalysts are shown in Figure 3.9. CO stripping conditions were identical (adsorption potential, adsorption time, sweep rate etc). As expected PtRu was more active with respect to CO oxidation than Pt (the CO oxidation onset potential is more negative as well as peak potential (for PtRu peak potential is 0.425 V vs. Ag/AgCl and for Pt 0.536 V vs. Ag/AgCl)). While on the Pt catalyst CO

electrooxidation occurs in a relatively narrow potential range on PtRu it is spread over a broad potential range. Observed phenomena more likely reflect the structure of this particular PtRu catalyst than it is PtRu catalyst characteristic in general. A sharp and narrow-shaped CO stripping peak was obtained on smooth PtRu catalysts with different Pt:Ru compositions [16], on E-TEK unsupported catalyst [17] and on Johnson Matthey unsupported Pt-Ru catalyst [19] (nominally the same catalyst as in this study). In the present study, MEA's prepared from Johnson Matthey catalysts from three different lots were tested. All catalysts were used as received. Concerning CO oxidation, they behaved differently. Real catalysts are a mixture of PtRu alloy, Pt-oxides and Ru-oxides [27]. The ratio between alloy and oxide phases can vary even for the same nominal PtRu composition (Chapter 5). The difference between the present and literature results can be assigned to catalyst non-homogeneity.

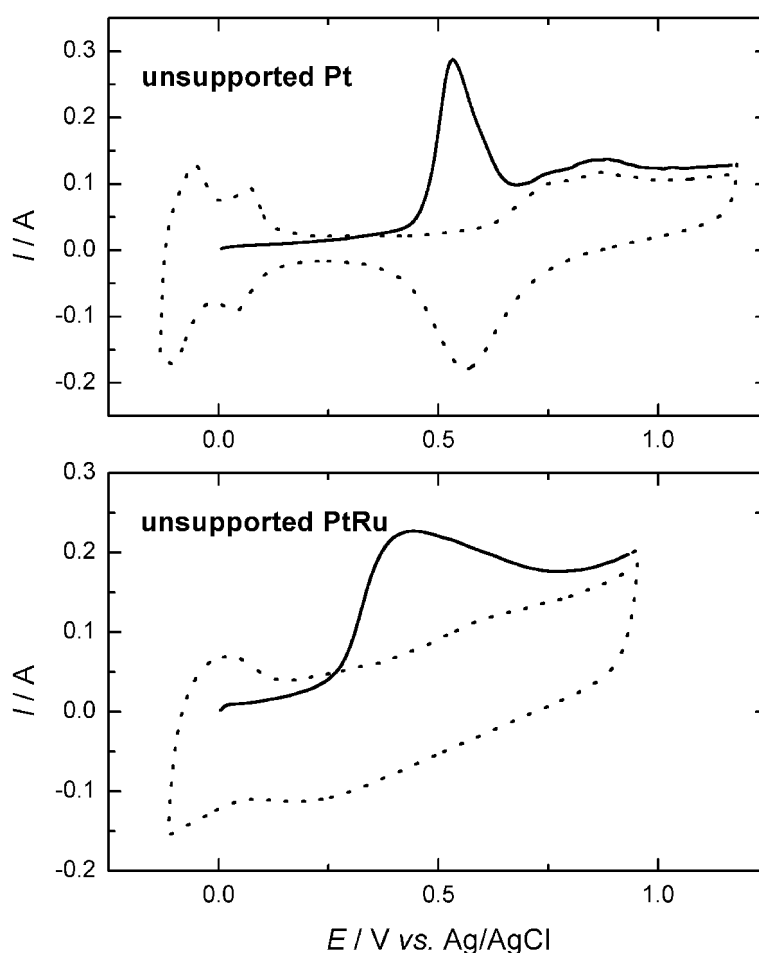


Figure 3.9 Cyclic voltammograms for CO stripping of unsupported Pt and PtRu MEA's. Dotted lines: after CO removal. Conditions: CO adsorption at 0 V vs. Ag/AgCl, adsorption time 30 min, sweep rate 50 mV s⁻¹.

In order to establish conditions for CO stripping on PtRu electrode the influence of several parameters was checked (potential region, sweep rate, adsorption potential, time of

adsorption). Now, the influence of these parameters on voltammetric CO charge determination will be discussed in more detail.

Potential region. Concerning the potential region for CO stripping, the cathodic potential limit is not an issue and usually is set to be the same as a potential for hydrogen evolution. The anodic potential limit is more sensitive issue due to the possibility of Ru dissolution [23]. In our experiments the positive potential limit was extended towards more positive potentials (starting from 0.5 to 1.0 V vs. Ag/AgCl) and no significant Ru dissolution was observed, even during prolonged cycling. As it was shown in reference [16] and found as well in the present experiments, extended positive potential limit is obligatory in order to capture entire CO oxidation wave on the PtRu catalyst. The CO charge as a function of the positive potential limit (other conditions are the same) is shown in Figure 3.10. Integration limits were chosen and the base line subtraction was done in a similar manner as in the case of platinum (see Figure 3.11 where integration limits are indicated by red arrows).

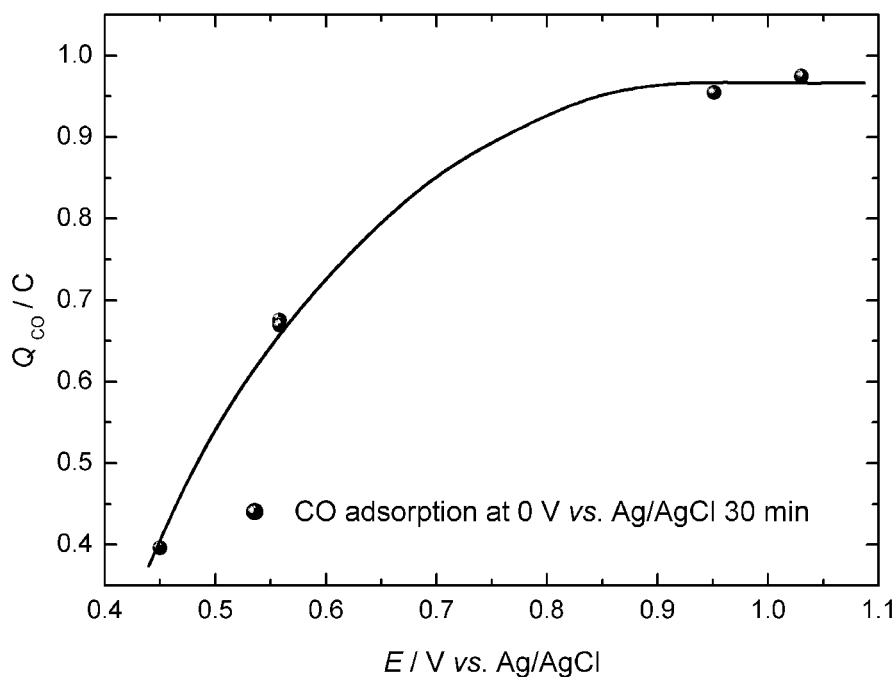


Figure 3.10 CO charge as a function of positive anodic limit. Sweep rate 50 mV s^{-1} . N_2 in working electrode compartment (flow rate 120 ml min^{-1}).

Sweep rate. The influence of sweep rate was studied with respect to the CO stripping peak potential and charge. With an increase of the sweep rate, the CO stripping peak potential is increasing (Figure 3.12). A slope of the peak potential dependence on log of sweep rate is 120 mV dec^{-1} , which corresponds to a theoretical case of oxidation of irreversibly adsorbed species [24].

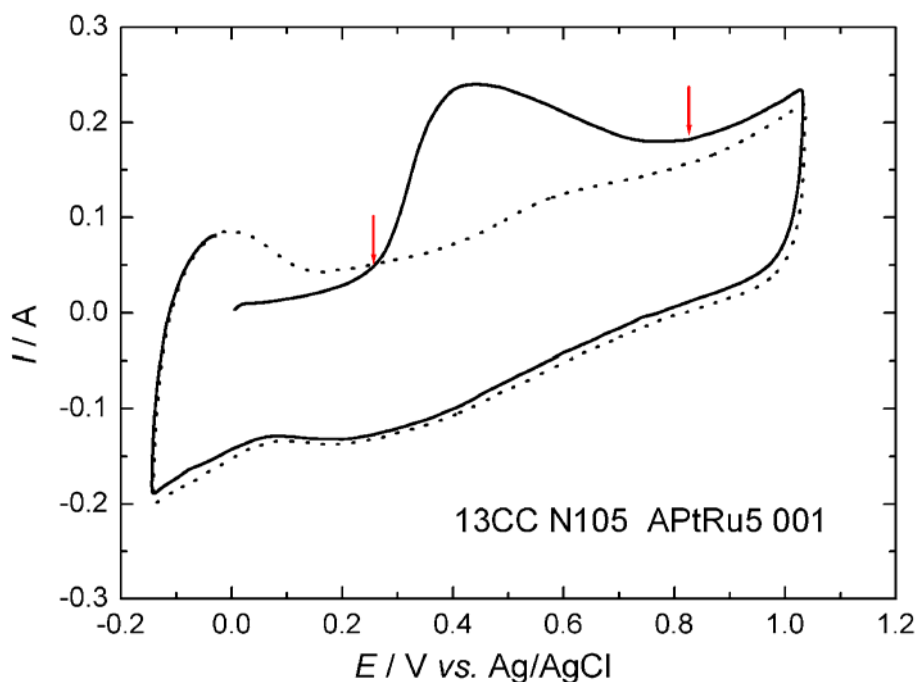


Figure 3.11 Cyclic voltammograms for CO stripping of unsupported PtRu MEA. Dotted line: after CO removal. Conditions: CO adsorption at 0 V vs. Ag/AgCl, adsorption time 30 min, sweep rate 50 mV s^{-1} .

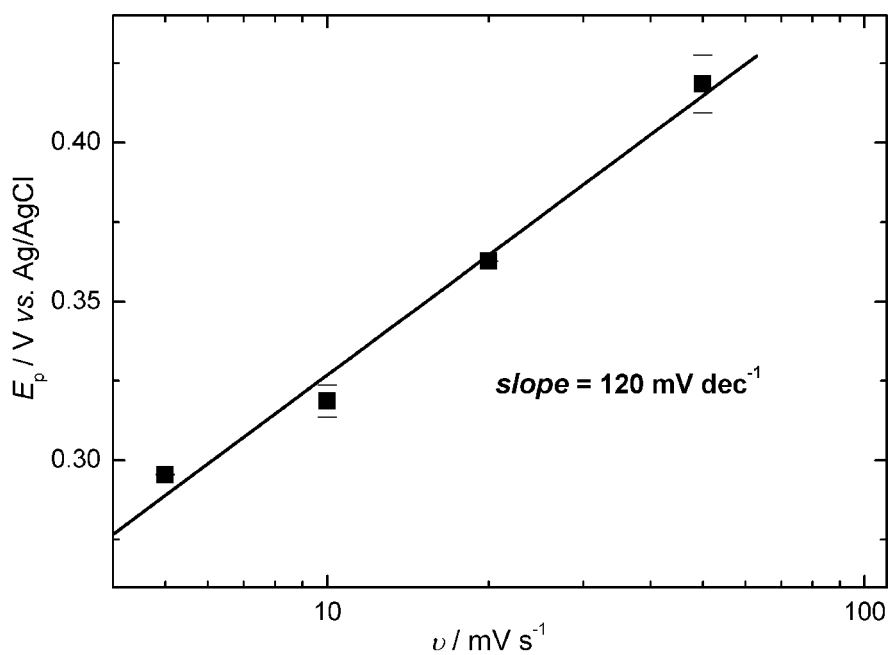


Figure 3.12 CO stripping peak potential vs. log of sweep rate. Conditions: CO adsorption at 0 V vs. Ag/AgCl for 30 min, N_2 in working electrode compartment, flow rate 120 ml min^{-1} .

With an increase of the sweep rate the CO stripping charge decreases. The maximum charge was determined for the lowest sweep rate of 5 mV s^{-1} (Figure 3.13, upper line). Integration limits were as indicated in Figure 3.11 and for base line subtraction, a second cycle after removal of CO was used. CO stripping charge was determined in a similar manner

as for platinum *i.e.* at first, the areas under the first positive going sweep and under the second positive going sweep (after CO stripping) in Figure 3.11 were determined. Then, the area from the second positive going sweep is subtracted from the area determined in the first positive going sweep and divided by sweep rate in order to obtain CO stripping charge. The resulting charge is plotted in Figure 3.13 as a function of sweep rate. As can be seen in Figure 3.13, the charge is decreasing with the sweep rate. Problems with the base line subtraction and uncertainties related to the base line subtraction in case of PtRu catalysts were already discussed. Briefly, oxide formation on PtRu catalyst overlaps with CO oxidation and proceeds in a different way with and without adsorbate and this cannot be ignored. In addition, it is assumed that oxide formation on PtRu depends on a sweep rate (Ru forms non stoichiometric oxides (RuO_xH_y), which undergo solid state surface redox transition [25]). This reaction involves proton injection/ ejection and is responsible for a large pseudo-capacitance of RuO_xH_y and overlaps with CO stripping as well. It was assumed that the base line deviation, caused by oxide formation, is more pronounced at the more positive potentials than at the more negative potentials, with respect to 0.3 V vs. Ag/AgCl. The reasons are as follows: a) CO and OH adsorption are competitive reactions. CO adsorption is favored at lower overpotentials. CO saturated coverage is assumed to be 0.68 (as determined in experiment with platinum electrode). As potential increases, OH begins to be adsorbed and surface coverage by OH increases. CO removal occurs in surface reaction between CO and OH adsorbed [26]. In course of time (or potential) CO surface coverage decreases while OH surface coverage increases. OH adsorption takes place at surface sites set free. Nafion[®] will also compete for the same surface sites but its influence was neglected here. Additionally, the oxide formed (for example Ru(OH)) can undergo further transformation to higher oxides (for example Ru(OH)₂ etc).

Therefore, here a rough approach for base line subtraction is proposed. A new base line is constructed as an extension of the CO stripping line (see Figure 3.14 red line). An assumption is that total CO charge is proportional to CO charge consumed until a potential that corresponds to one half of the height of the peak current (half peak potential in the following text) is reached. The approach was at first tested on platinum in order to determine which part of the total CO stripping charge is oxidized until the half peak potential.

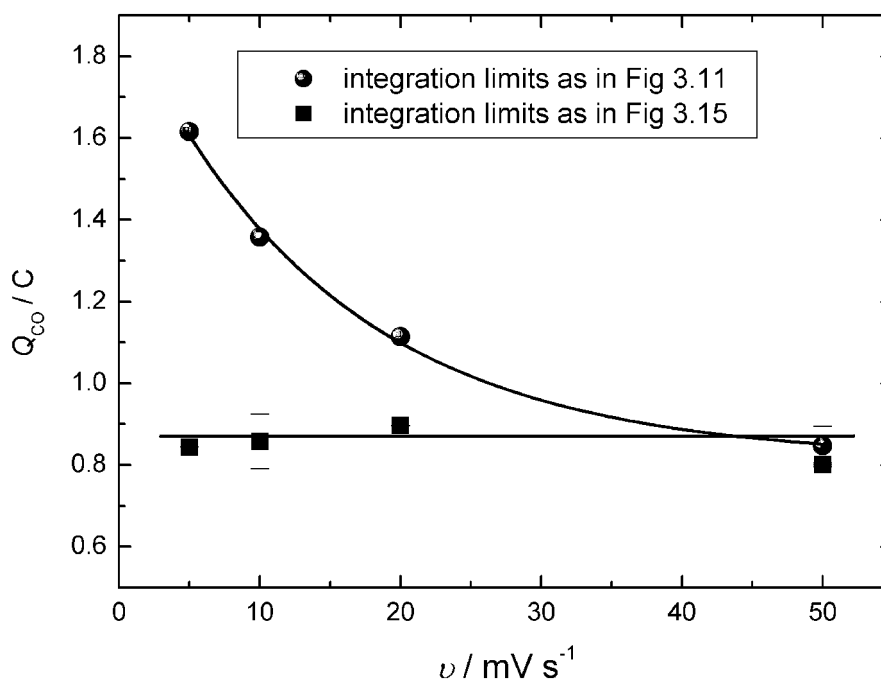


Figure 3.13 CO stripping charge as a function of sweep rate for different integration limits.

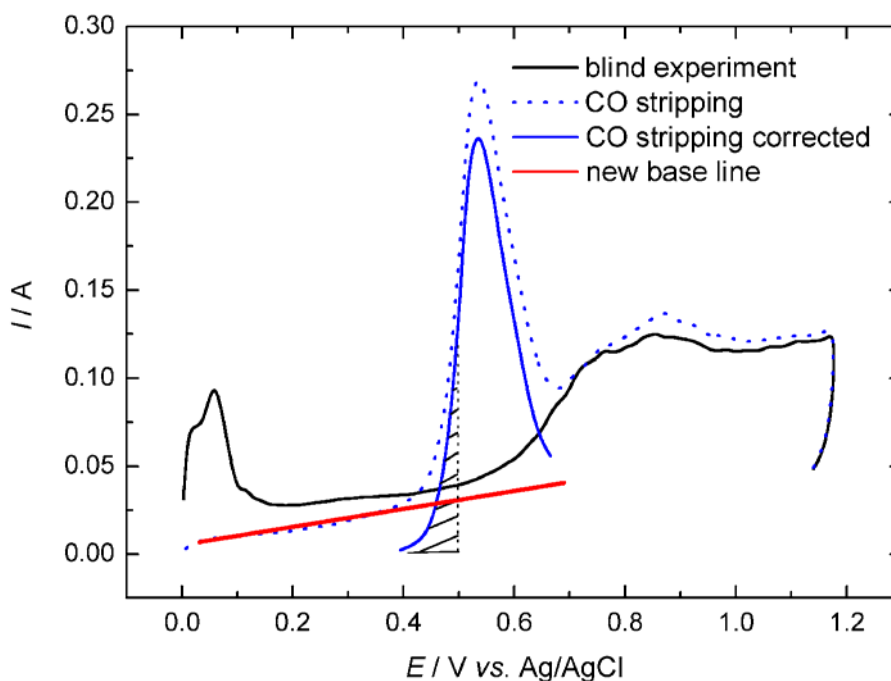


Figure 3.14 Schematic representation of base line correction in the case of Pt MEA. Conditions: the same as in Figure 3.5.

The result of integration (hatched area in Figure 3.14) was divided by the sweep rate and the value of 0.0604 C was obtained. The total CO stripping charge was determined to be 0.629 C. It follows that 9.6 % of the total CO adsorbed is oxidized until the half peak potential is reached.

In the case of PtRu catalyst a new base line is constructed in a similar manner, as shown in Figure 3.15 (full red line). Then, the base line is subtracted from the CO stripping line (first positive going sweep). As a result a new CO stripping line is formed (blue line in Figure 3.15). An area under the new CO stripping line (blue line) is integrated, but only until half peak potential (hatched area in Figure 3.15). The assumption was made that the 9.6 % of total CO adsorbed is consumed until the half peak potential is reached and this charge is multiplied by approximately factor 10 in order to obtain the total CO charge. Obtained results are shown in Figure 3.13 and as can be seen, data are scattered around a mean value of 0.87 C and no dependence on the sweep rate is observed. This is confirmation that the integration up to the half peak potential gives reliable data for the total CO charge.

Adsorption potential. Most of the experiments were performed at an adsorption potential of 0 V vs. Ag/AgCl, while in some of them CO was adsorbed some at more negative potential -0.1 V vs. Ag/AgCl. No significant influence on CO charge, CO stripping peak potential and onset of the CO oxidation was obtained, by varying the adsorption potential.

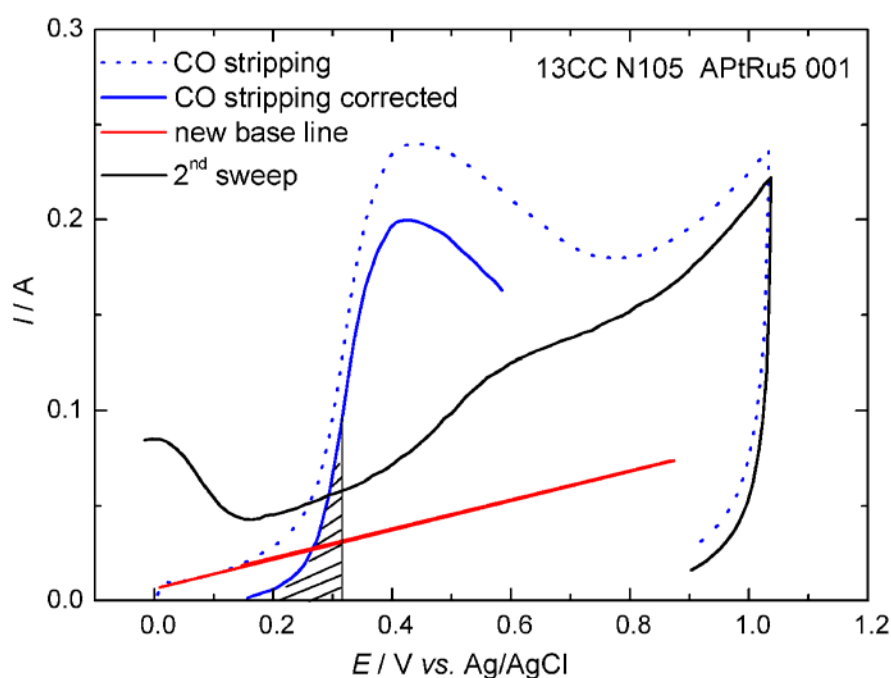


Figure 3.15 Schematic presentation of the proposed method for base line subtraction in voltammetric CO charge determination in the case of PtRu MEA. Conditions: same as in Figure 3.11.

Time of CO adsorption. CO was adsorbed at constant potential, while the adsorption time was varied. It was found that CO saturated coverage was achieved in approximately 120 min (Figure 3.16). The adsorption time for obtaining the CO saturated coverage was significantly greater than in the case of platinum. One reason can be that kinetics of CO adsorption on pure platinum and on platinum ruthenium alloy are different. Also as a less

noble metal than platinum, ruthenium should be more oxidized under the applied conditions. CO adsorption was performed at potentials more negative than oxide reduction on PtRu e.g. at sweep rate of 10 mV s^{-1} potential of PtRu oxide reduction is at approximately $0.25 \text{ V vs. Ag/AgCl}$ - Figure 3.17. Because of that first an oxide present at the surface will be reduced and after that CO adsorption will take place.

The saturated CO coverage corresponds to a CO stripping charge of 0.817 C . The real surface area can be obtained from the following equation:

$$S = \frac{Q_{\text{CO}}}{\theta_{\text{CO}}^{\text{sat}} \cdot 0.420 \text{ mC cm}^{-2}} \quad (3.7)$$

where S is the real surface area, Q_{CO} is the CO stripping charge in mC, $\theta_{\text{CO}}^{\text{sat}}$ is the saturated CO coverage, and 0.420 mC cm^{-2} is the charge for the oxidation of nearly a CO monolayer.

The calculated value is $2.86 \times 10^3 \text{ cm}^2$. Normalized value with respect to the metal loading it is $17.7 \text{ m}^2 \text{ g}^{-1}$. Taking into account that the geometric surface area is 3.24 cm^2 , the BET surface area for this catalyst is much larger (according to supplier: $62.56 \text{ m}^2 \text{ g}^{-1}$). Deviation can be due to the same reasons as discussed in the case of platinum. Additionally, a more oxidized catalyst will have a lower CO stripping area as found in literature as well [19].

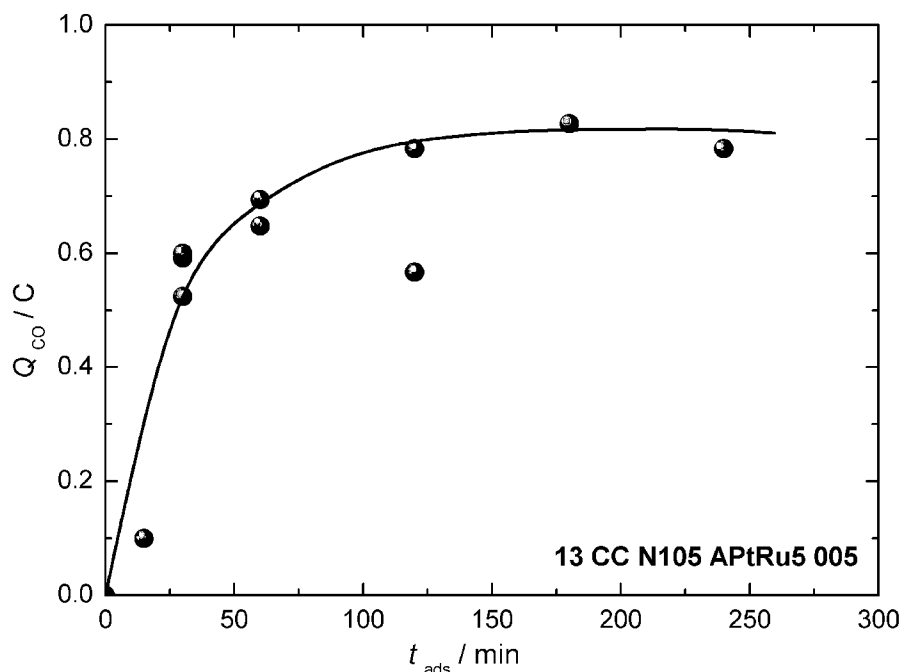


Figure 3.16 Voltammetric CO stripping charge as a function of adsorption time. Conditions: Adsorption potential 0 V vs. Ag/AgCl , sweep rate 5 mV s^{-1} , flow rate 120 ml min^{-1} , room temperature.

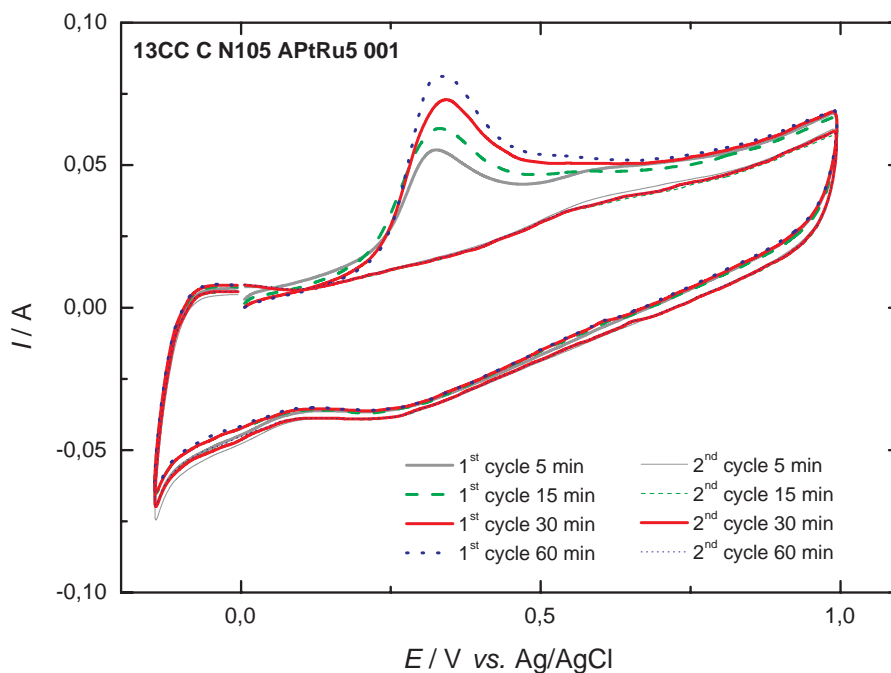


Figure 3.17 CO stripping voltammetry of unsupported PtRu MEA as a function of adsorption time. Conditions: Adsorption potential 0 V vs. Ag/AgCl, sweep rate 10 mV s^{-1} , flow rate 120 ml min^{-1} , room temperature.

3.3. Conclusions

The real surface area of the unsupported platinum catalyst within the MEA was determined by hydrogen and carbon monoxide adsorption methods. It was assumed that the hydrogen adsorption method gives the total number of reactive surface sites. The saturated CO coverage was calculated by comparing the surface areas determined by the carbon monoxide and hydrogen adsorption methods. A value of 0.68 was obtained. Later this value was used for the calculation of the surface area of unsupported PtRu catalysts (and carbon supported PtRu catalysts, see Chapter 5). The assumption was made that CO saturated coverage is the same, for both the platinum and the metallic parts of the various PtRu catalysts being investigated.

The carbon monoxide method was applied to the surface area determination of unsupported PtRu catalysts. The influence of the positive potential limit, the sweep rate, the CO adsorption potential and the time was investigated. It was shown that the positive potential limit has to be extended up to 1.0 V vs. Ag/AgCl in order to capture the whole CO stripping wave. The CO charge was decaying with the sweep rate when a base line subtraction was performed as in the case of platinum, *i.e.* with the assumption that oxide formation and double layer charging are the same, with and without adsorbate. It was

suggested to use a new constructed base line for base line subtraction. When the corrected CO stripping line was integrated up to the half peak potential and multiplied with the factor determined in a similar experiment with unsupported platinum calculated CO stripping charge became independent of the sweep rate. CO adsorption was performed at two different potentials and no significant influence was observed. It was established that CO saturated coverage was achieved after about 2 h.

3.4. Outlook

A method for base line subtraction and CO stripping charge determination was proposed. But this method is based on several assumptions and on experimental observations. It should be reasonable to calibrate this kind of voltammetric CO stripping charge determination by a method which is not sensitive to non-Faradaic and other Faradaic contributions (like DEMS or IR as already used in the literature) with an attempt to determine the CO voltammetric charge in a more quantitative manner. This would be valuable for a fast screening of the real surface area of a porous catalyst under technically relevant conditions, because the traditional electrochemical techniques are simpler and available in most fuel cell labs.

Also a mathematical model for CO stripping under investigated conditions would be of interest.

4. Kinetics of methanol oxidation

Literature data about the kinetics of electrochemical methanol oxidation are numerous. The reaction was thoroughly investigated on platinum (polycrystalline and single crystal platinum electrodes, dispersed supported and unsupported platinum) [28-31] and different types of PtRu alloys (bulk alloys [32,33], supported [23,34,35] and unsupported PtRu [36,37] catalysts, Ru deposited on platinum [38] etc.) with different techniques. In this chapter an overview of literature results concerning methanol oxidation is given, but without the attempt to comprehend all published data. The basic idea was to give a cross section of the research starting from the seventies, to underline some of the most striking results in this field and to show how the understanding and the knowledge about the mechanism of methanol oxidation was growing through several decades. At the beginning two important references from the seventies should be emphasized. The first one is a famous paper from Bagotzky *et al.* [28] where the first complete reaction scheme of methanol oxidation is given and which in essence is still regarded to be valid. The other one is an equally famous paper from Watanabe and Motoo [39], where the concept of bi-functional catalysis, already known in the field of heterogeneous catalysis, was first introduced in the field of electrocatalysis in order to explain the enhancement of methanol oxidation at a PtRu alloy compared to pure Pt. In the following years research efforts were aiming to identify some of the proposed intermediates in methanol oxidation by spectroscopic techniques, mass spectroscopy, electrochemical techniques, isotope labelling studies and others. Another branch of research was oriented to explain the enhancement of the reaction rate by Ru, to determine the optimal PtRu composition, to find better synthetic routes for catalyst preparation (see Chapter 5) and to investigate structural effects. After giving a literature overview, own experimental data on the kinetics of methanol oxidation under fuel cell relevant conditions (temperature 60°C, methanol concentration 1 M, unsupported PtRu catalyst in a membrane electrode assembly (MEA)) are presented. Based on these data rate expression for methanol oxidation kinetics is derived. This rate expression is suitable for implementation in a mathematical model of the whole DMFC. Most of the experiments presented in this Chapter were performed at an unsupported PtRu catalyst (from Johnson Matthey supplier) with a PtRu loading of the

electrode 5 mg cm^{-2} . However this loading is rather high and would increase the production costs of the DMFC significantly. But loading can be varied in the fuel cell. Also the catalyst dispersion at the same metal loading can be increased if the catalyst is supported on a conductive support. Relevance of varying the metal loading and a comparison between supported and unsupported catalysts at the same metal loading are given at the end of this chapter in order to evaluate the importance of these parameters (metal loading and catalyst dispersion) on selected reaction mechanism for methanol oxidation.

4.1. Mechanism of methanol electrooxidation – Literature overview

As pointed out above, the first complete reaction scheme for methanol oxidation on platinum was formulated by Bagotzky *et al.* [28] in 1977. According to these authors methanol oxidation occurs through the following steps:

a) Methanol adsorption at the electrode surface followed by methanol dehydrogenation (also called dissociative electrosorption [6]):



b) water dissociative adsorption:



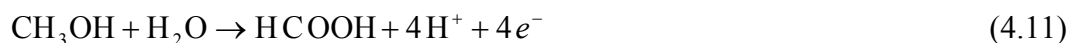
c) surface reaction between species produced in steps a) and b):



In equations (4.1) to (4.9) the index “x” denotes a valence bond with the platinum surface. OH stands for adsorbed OH species on the electrode surface and $\overset{\text{C}}{\text{C}} = \overset{\text{O}}{\text{O}}$ stands for the bridge bonded CO species on the surface.

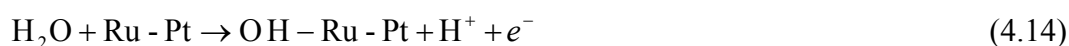
The electrochemical steps are the steps (4.1) to (4.4), while the other steps (from (4.5) to (4.9)) are heterogeneous chemical steps. In methanol dehydrogenation (step “a”) the removal of the first proton is the rate determining step (r.d.s), while the subsequent steps are fast. As a consequence, $\overset{\text{C}}{\text{C}}\text{-OH}$ is the only species resulting from step “a” (at low overpotentials where the formed species can not be further oxidized, *i.e.* upon methanol adsorption at open circuit potential).

According to this mechanism, in the overall reaction 6, 4 and 2 electrons can be exchanged and as final products CO_2 (equation 10), HCOOH (equation 4.11) and/or CH_2O (equation 4.12) are formed respectively:

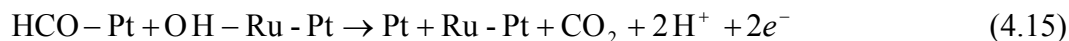


The distribution of the reaction products depends on the potential, temperature and coverage of the surface with H_{ads} , OH_{ads} , other organic adsorbed species ($\overset{\text{C}}{\text{C}}\text{H}_2\text{OH}$, $\overset{\text{C}}{\text{C}}\text{HOH}$, $\overset{\text{C}}{\text{C}}\text{-OH}$, $\overset{\text{C}}{\text{C}} = \overset{\text{O}}{\text{O}}$) and foreign particles (e.g. adsorbed metal atoms). For example, depending on the OH_{ads} surface concentration $\overset{\text{C}}{\text{C}}\text{HOH}$ can be oxidized in two different ways. If the OH_{ads} concentration is low, then mainly CO_2 will be formed. At high OH_{ads} concentrations the main products will be HCHO and HCOOH .

At about the same time (in 1975) Watanabe and Motoo [39] gave the first explanation of the enhancement of the methanol oxidation rate at PtRu alloys. They introduced the concept of bi-functional catalysis where Pt is responsible for methanol dehydrogenation and Ru for the adsorption of OH species:



and finally



where Pt represents the clean platinum substrate, while Pt-Ru represents platinum having adsorbed ruthenium. HCO is proposed as an active intermediate. It requires only one adsorption site on the surface and is bonded at the platinum substrate *via* a C atom.

During the eighties a scientific discussion was focused on the following topics: a) the nature of intermediates formed (with hydrogen (HCO or COH) or without hydrogen (CO)), b) whether these species are necessary intermediates or “poisons”, c) whether CO is linearly or bridge bonded, d) the source of oxygen in the reaction, e) the activity of pure metals *vs.* alloys in methanol oxidation and etc. Results are summarized in a review paper by Parsons and VanderNoot [29] and in the following text they will be briefly presented.

In these years, due to the significant progress in instrumental analytics, the experimental identification of the final products and intermediates in methanol oxidation became feasible. As final products CO₂, H₂CO and HCOOH were identified by means of mass spectral measurements and gas chromatography absorbance measurements. For intermediate identification following techniques were used: a) in-situ spectroscopic techniques (like electrochemically modulated infra-red spectroscopy (EMIRS), infra-red reflection absorption spectroscopy (IRRAS)), b) differential electrochemical mass spectroscopy (DEMS), c) cyclic voltammetry, d) isotope labeling combined with mass spectroscopy. In principle two groups of intermediates were identified: a) species containing hydrogen (HCO or COH) and species without hydrogen (CO). Intermediates with hydrogen were detected by DEMS, while those without hydrogen were detected by EMIRS. Discrepancies between two groups of techniques are caused by different experimental conditions. DEMS was applied to porous electrodes, while EMIRS was done at mirror smooth electrodes. Also the time scale for DEMS is shorter while for EMIRS is longer. Thus, it was concluded that DEMS yields the short living intermediates, while EMIRS the long living ones. Cyclic voltammetry was used to evaluate the charge being necessary to oxidize the intermediates in methanol oxidation. The experiment was typically performed in the following way: First methanol was adsorbed for a fixed period of time, the solution was replaced by a supporting electrolyte and then the adsorbed species were oxidized in a potential sweep. The number of exchanged electrons was varied depending on the methanol concentration and adsorption time. Lower methanol concentrations and shorter adsorption

times give 3 electrons exchanged in methanol adsorption and oxidation, which is an evidence for adsorbed intermediates containing hydrogen. Higher methanol concentrations and longer adsorption times give between 1 and 2 exchanged electrons which suggest formation of a mixture of CO and species containing C, H and O. In experiments with isotope labeling hydrogen containing intermediates were identified but without full agreement between different authors whether the intermediate is CHO or COH.

The next important topic during the eighties was whether CO, CHO and COH are reactive intermediates or poisons¹⁵. Finally it was concluded that CO is a poison, while CHO is an intermediate.

CO can appear on the electrode surface in two forms: bridge bonded and linearly bonded. Bridge bonded CO is the more abandoned species at lower methanol concentrations and more negative potentials, while linearly bonded predominates at higher methanol concentrations and more positive potentials.

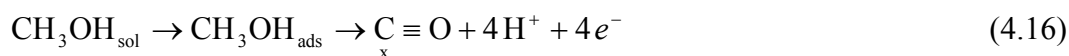
The role of surface oxides was also discussed. It was concluded that surface oxides serve primarily as oxygen source.

Concerning electrode materials, it was concluded that a PtRu alloy shows a better performance in methanol oxidation than pure Pt. Higher activity of the alloy was hypothesized to be due to: a) a modified electronic nature of the surface, b) a modified physical structure, c) a blocking of the poison formation reactions, d) adsorbing oxygen or hydroxyl ions, which can take place in the main oxidation reaction.

At the beginning of the nineties Gasteiger *et al.* [32] investigated methanol oxidation on PtRu bulk alloys by cyclic voltammetry at room temperature. In their study well defined PtRu alloys with different PtRu compositions were investigated. They found that a PtRu alloy with 10 % Ru gives the highest enhancement at the methanol oxidation activity compared to pure Pt at room temperature. The result contrasted results of Watanabe and Motoo [39], where a PtRu alloy with a PtRu composition of 50:50 was declared to be the best. The discrepancy between new and old results was attributed to the ruthenium depletion at the surface caused by electrode preconditioning in extended potential limits, resulting in a lower Ru surface composition than nominal. Thus, the importance of surface characterization was emphasized.

¹⁵ A poison is defined as a species that is strongly adsorbed on a surface and cannot be easily oxidized.

It was postulated [32] that the balance between the rate of methanol adsorption and the rate of oxidative removal of dehydrogenated fragments determines the activity of the PtRu catalyst. The following mechanism was proposed:



where “x” denotes the valence bond with the platinum surface and “y” the valence bond with the ruthenium surface.



The mechanism presented above is based on the Bagotzky mechanism [28], and bi-functional catalysis proposed by Watanabe and Motoo [39].

Besides this historical context, the proposed mechanism involves the following evidences: a) “poisons” identified by different in situ techniques, and b) UHV (ultra high vacuum) studies of methanol adsorption on Pt and Ru.

The mechanism (4.16 – 4.19) predicts linearly bonded CO as the main product of methanol dehydrogenation. This came out as a result of in-situ infrared spectroscopy techniques as discussed above [29]. In UHV studies methanol adsorbs on both clean Pt and Ru surface and produces adsorbed CO and H species (at Pt adsorbed CO and H are produced at temperatures higher than 170 K and at Ru at temperatures higher than 230 K). The driving force for low temperature methanol decomposition into adsorbed CO and H is a very large heat of adsorption of both species on Pt and Ru surfaces (for platinum surface heat of adsorption of CO and H are 125.4 kJ mol⁻¹ and 74.4 kJ mol⁻¹, respectively). The values for Ru are within 20 % of the above-mentioned values for Pt. If strongly adsorbed molecules precover the electrode surface, then the favorable lowering of the overall free energy upon decomposition of methanol will be reduced by the adsorption energy of preadsorbed surface species. This explains why methanol does not adsorb on Ru under fuel cell conditions. For methanol to be adsorbed, the surface should be free from other adsorbates. For example, methanol adsorption on Pt will start after desorption of adsorbed H is finished and on Ru it will not take place at all, if OH species are adsorbed on the surface.

The catalytic effects of bimetallic systems can be due to: a) blocking of surface sites to prevent formation of strongly bound poisons, b) bi-functional catalysis, c) an electronic interaction between the catalyst's components. Here possibility a) was discarded since a 10 % PtRu alloy has a very open structure. Possibility c) was also ruled out because UHV study showed that the surface diffusivity and adsorption of CO on both Pt and Ru are similar. Therefore, the enhancement of methanol oxidation was explained using statistical interpretation of the bi-functional action of the alloy surface, as outlined in the following.

To explain higher activity of PtRu alloy with 10 % of Ru than PtRu alloy with 50 % Ru, statistical analysis can be employed. It was assumed that for methanol adsorption on platinum 3-fold Pt sites are needed and the probability of their finding on a 10 % Ru alloy is higher than on a 50 % Ru alloy. It was concluded that on a Ru-rich alloy the rate determining step is methanol dehydrogenation, while on a 10 % Ru alloy the reaction between adsorbed intermediates is slow. Consequently, the reaction order with respect to methanol on a Ru-rich PtRu alloy should be close to 1 and for PtRu alloys with a low Ru content the reaction order should be close to 0.

The improvement of the catalyst activity of a 10 % Ru alloy over a 50 % Ru alloy can be interpreted in terms of the Bagotzki mechanism [28] as well. Namely, a Ru-rich PtRu alloy has a high concentration of OH species and the probability of 3-fold platinum sites is lower compared to a Pt rich alloy, so the probability of forming side products in methanol oxidation is higher (see reaction 4.5 and 4.6). This was later verified in Kabbabi *et al.* study [33].

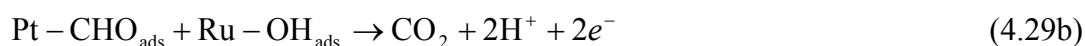
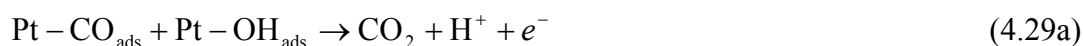
The study by Q. Fan *et al.* is interesting [40] because it shows how the distribution of final products changes depending on the methanol/water vapour ratio and the anode potential. These authors investigated the methanol oxidation at Pt and PtRu catalysts in the direct methanol fuel cell by in-situ Fourier transform infrared-diffuse reflection spectroscopy (FTIR-DRS). Different final products were identified. At low methanol/water - ratio the primary product was CO₂. At a higher methanol/water - ratio formaldehyde was identified as the only product at more negative potentials, while methylformate and formic acid at more positive potentials. The following mechanism for methanol oxidation was proposed:





This mechanism predicts homogenous chemical reactions between formed products and methanol: formaldehyde and methanol react and form dimethoxymethane; formic acid and methanol give an ester.

In their study Kabbabi *et al.* [33] conducted combined cyclic voltammetry and FTIR at well defined platinum ruthenium alloys with different compositions. Higher current densities in methanol oxidation were obtained at PtRu alloys with a low Ru content (10-15 *at %*), which is in accordance with Gasteiger *et al.* [32]. CO, but also small amounts of HCHO and HCOOH were measured by FTIR. It was found that the distribution of reaction products varies with the PtRu composition with less complete methanol oxidation on a PtRu alloy with 50:50 *at %* Pt:Ru. The following mechanism for methanol oxidation was proposed:



Reaction 4.29b is faster than 4.29a and occurs at lower potentials. Formation of adsorbed OH species on the ruthenium surface is postulated as a rate determining step (equation 4.28b). This assumption is supported by the low amount of linearly bonded CO at the surface which indicates that all CO produced in step 4.27 is consumed in steps 4.29a or 4.29b.

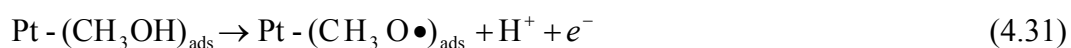
Very comprehensive reviews on methanol oxidation on platinum and platinum ruthenium alloys were written by Hamnett in 1997 [30] and in 1999 [31].

The mechanism of methanol oxidation was evaluated using different physical and electrochemical techniques on both platinum and on platinum ruthenium alloys. Results of electrochemical studies performed on single crystals and polycrystalline platinum electrodes

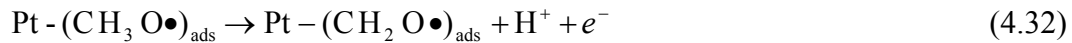
during the nineties and earlier were summarized. Influence of anion adsorption on methanol oxidation was examined. A pronounced influence of anion adsorption on methanol oxidation on low index single crystal surfaces was observed. The maximum reaction rate was obtained in the presence of perchlorate ions, while the minimum rate in the presence of sulphate ions. These results were commented as being a consequence of competitive adsorption of methanol and anions from the supporting electrolyte, which is similar to the review paper by Parson and VanderNoot [29]. Also new studies confirmed findings from previous studies and showed that the nature of chemisorbed intermediates changes with time and the coverage of the surface but that linearly bonded CO seems to be the final product on almost every surface and at longer adsorption times. Spectroscopic studies pointed out that chemisorption of methanol gives rise to linearly or bridge bonded CO and that the proportion in which those two species are present at the surface is determined by the crystallographic face exposed. At lower methanol concentration another adsorbed intermediate is also present and it is identified as COH. Also some evidences are found that there is an additional pathway for methanol oxidation that goes through soluble or weakly adsorbed intermediates such as formic acid, formaldehyde or CO adsorbed at metastable sites like CO adsorbed at edges of CO islands.

Concerning the role of ruthenium in promoting methanol oxidation on a platinum ruthenium alloy, it was concluded that the electronic effect and increase of the coverage of the PtRu surface by oxy-species are important. From FTIR studies it was seen that the coverage by CO_{ads} on a PtRu alloy is reduced compared to pure platinum and an increase in the absorption frequency of the bound CO is also seen. CO is less strongly adsorbed on a PtRu surface due to a reduction in the back π -bonding from Pt to the CO π^* orbital. The reduction in the π -back bonding will lead to a higher positive charge on the carbon atom rendering it more liable to a nucleophilic attack by water and permitting CO oxidation at lower potentials. The second effect is the increase in the coverage of the PtRu surface by oxy-species. An increase of the amount of Pt-O species in the presence of Ru was proved by XPS.

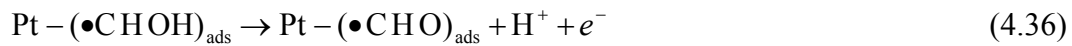
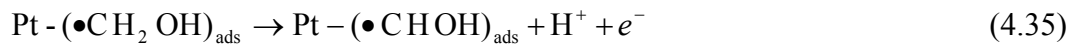
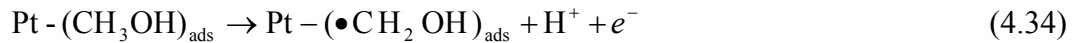
Another review paper on the reaction mechanism at platinum based catalysts was published in 2001 by Leger [41]. Besides the reactions proposed by Bagotzki [28], the scission of the first hydrogen atom from the OH group in methanol was also introduced into the mechanism:



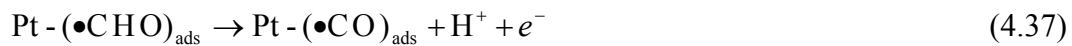
Further transformation of formed species is enabled through scission of H atoms bound to a C-atom in the following reactions:



CHO can be also formed in the following reactions:



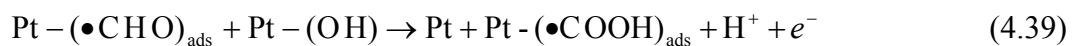
$\bullet\text{CHO}$ is considered to be an active intermediate and can react further giving adsorbed CO which is considered to be a poisoning intermediate on platinum



or can directly transform into CO_2



or first react in the following manner



and then undergoes conversion to CO_2



At more positive potentials adsorbed CO can be oxidized through the reactions:



In case of a PtRu alloy the dissociative adsorption of water (e.g. equation 4.28b) takes place on Ru sites at lower potentials and the oxidation of formyl like species occurs through reactions described above but OH is adsorbed on Ru sites.

So in contrast to Bagotzki [28] who postulates the COH intermediate, Leger [41] postulated a CHO intermediate as a major reactive intermediate. As can be seen from the above equations, CHO is obtained as a product of methanol dehydrogenation no matter if the scission of the first hydrogen was from a O-H group or from C-H.

Summarizing the literature results, methanol oxidation at PtRu alloys occurs through the following steps:

- a) methanol dissociative adsorption
- b) water dissociative adsorption
- c) reaction between species formed in steps “a” and “b”

Below temperature of 60°C step “a” occurs only on platinum [42]. Step “b” can take place both on platinum and ruthenium, but on ruthenium this reaction is facilitated at lower potentials (water dissociative adsorption takes place at 0.3 V lower overpotentials on Ru than on Pt [31]). Methanol dissociative adsorption can give different dehydrogenated intermediates as proposed in the reaction mechanisms shown above (COH (according to Bagotzki [28]), or CHO (HCO) according to Leger [41], Watanabe and Motoo [39]). In Parsons and VanderNoot [29] paper broad discussion about the nature of intermediates was given and more authors stated CHO rather than COH as the intermediate. Theoretical calculations have shown that the heat of formation of COH species on a PtRu alloy is more negative than for CHO species and that the former should be favored on a PtRu surface [43]. Irrespective the nature of this intermediate, the final product of methanol dehydrogenation is always CO, linearly or bridge bonded to the surface, as detected in several studies. So, Kabbabi *et al.* [33] detected linearly bonded CO on PtRu alloys with different PtRu compositions but in lower extent than on pure platinum. Adsorbed CO was also detected in a infrared study by Kardash *et al.* [42] on a PtRu alloy with 10 at % Ru. The coverage by CO on PtRu alloy with only 10 at % Ru was high and almost the same as on pure platinum, but CO oxidation commences at lower overpotentials than on platinum itself. For the PtRu alloy with a Ru content of 50 at %, the CO adsorption band was almost at the level of noise. Also in the DEMS study Jusys *et al.* [36] CO_{ads} was identified as a stable adsorbed product of methanol dehydrogenation based on the electron yield of 1.9 electrons per CO₂ at PtRu

unsupported catalysts. Methanol conversion to CO₂ is higher at lower overpotentials, while at higher overpotentials the production of methylformate starts. This is in accordance with the Bagotzki mechanism [28] where the CHOH transformation can produce CO₂ at low OH concentrations and other products at high OH concentrations. The same conclusion was drawn by Wang *et al.* [38], where it was shown that the formation of methylformate¹⁶ on PtRu starts at the same potential as on platinum, but increases with potential more strongly than on platinum (due to the higher amount of OH adsorbed on the surface). CO is oxidized on the surface and CO₂ was found as the main oxidation product. Besides CO₂ a small amount of other products is also identified. Kabbabi *et al.* [33] measured HCHO and HCOOH by FTIR and found that the proportion of these products is increasing with increasing Ru content in PtRu alloys. CO₂ as well as formaldehyde and formic acid were found by Wang *et al.* [38] in their DEMS at Pt-based catalysts. It was concluded that Ru promotes methanol oxidation to CO₂ via CO adsorbed intermediates leading to a higher current efficiency of CO₂. The identified by-products of methanol oxidation support a parallel mechanism, but a parallel path that does not go through adsorbed CO is less dominant at PtRu alloys than at pure Pt [38].

The previous discussion was focused on presenting different mechanisms of methanol oxidation and evidences for these mechanisms obtained mainly from non-electrochemical studies. Besides these non-electrochemical studies, many typical electrochemical studies were performed in order to understand the mechanism of methanol oxidation. They were concentrated on the determination of the Tafel slope, the reaction order with respect to methanol and H⁺ and the activation energy. However, not many studies were performed on a rate expression for the kinetics of methanol oxidation at PtRu catalysts. Moreover, most works were not performed under conditions being relevant to real fuel cell operation. Some of the literature results are briefly discussed below.

Tafel slope values were reported to be 115 mV dec⁻¹ in a temperature range from room temperature to 40°C [23] and between 155 and 168 mV dec⁻¹ in a temperature range from room temperature to 60°C [34] at supported PtRu catalysts, from 130 to 140 mV dec⁻¹ in a temperature range from 100 –130°C at unsupported PtRu catalysts [27]. The reaction order with respect to methanol was reported to be 0.5 and potentially independent [23]. In another study, the reaction order with respect to methanol was found to be in the range from 0.48 to

¹⁶ Methylformate is formed in reaction between formic acid and methanol (equation 4.26).

0.78, potential - dependent and also dependent on whether water or sulphuric acid anions were present in the solution (higher values were obtained when sulphuric acid was replaced by water) [34]. Apparent activation energies of 29 kJ mol^{-1} for unsupported PtRu blacks [37], $35\text{-}40 \text{ kJ mol}^{-1}$ [34] and about 70 kJ mol^{-1} [23] for carbon supported PtRu were reported. Different rate determining steps (r.d.s) were suggested: reaction between adsorbed CO and OH species [23,32], formation of adsorbed OH on the ruthenium surface [33], slow methanol adsorption [44], dissociative adsorption of methanol [45], mixed control by methanol adsorption and activation step [34]. At high overpotentials the reaction is limited by methanol adsorption [46] leading to reaction limiting current. This is in accordance with findings from Gojkovic *et al.* [23] who showed, that in this region the current is not mass-transfer controlled. Also in the Tafel region the reaction order with respect to H^+ was -0.5 suggesting OH participation in the r.d.s. At higher overpotentials no influence of the H^+ concentration was found, indicating no OH participation in the r.d.s. In an own previous study [35] external (in the liquid phase) and internal (in the back diffusion layer) the influence of mass transfer resistances was estimated from dimensionless parameter groups and it was shown that they are five to ten times smaller than the overall reaction resistance.

In the following, own experimental data on the kinetics of methanol oxidation are presented. Catalyst characterisation was performed by *in-situ* methods: CO stripping voltammetry and cyclic voltammetry in the absence of methanol and will be discussed first.

4.2. Catalyst characterization

Cyclic voltammograms at an unsupported PtRu catalyst in the absence of methanol are shown in Figure 4.1. When the higher anodic limit was $0.5 \text{ V vs. Ag/AgCl}$, cyclic voltammetric features in anodic and cathodic scan direction were almost symmetrical. Cyclic voltammograms can be used as a “fingerprint” of an electrode surface [16, 37, 47]. According to the literature [37], the absence of hydrogen adsorption at potentials being more positive than $0.0 \text{ V vs. Ag/AgCl}$ resembles Ru like features. Similar features as in our case were obtained in reference [37] for unsupported PtRu catalysts with a Ru content of approximately 52 *at %* and higher. Also in reference [16] a similar voltammogram was obtained for PtRu bulk alloys with a Ru content of 46 *at %* and higher. However, cyclic voltammetry cannot be used as a definite tool for surface composition determination, but just as an indication¹⁷. The

¹⁷ See also Chapter 5.

reason is the uncertainty whether the catalyst is predominately a PtRu alloy with a Pt:Ru composition close to the nominal value and with a small fraction of Ru metal, hydrous Ru oxide and Pt oxide [19] or a mixture of a Pt-rich phase, Ru-oxides, Pt-oxide and a small quantity of Ru metal phase [48]. If the positive potential limit was extended up to 1.0 V vs. Ag/AgCl, oxide formation was recorded in a positive going sweep followed by its reduction in the negative going sweep. Although reported in some studies [23], electrode cycling in these extended potential limits did not cause ruthenium dissolution as was judged from the cyclic voltammetry behaviour. According to Long *et al.* [48], the broad capacitive features in Figure 4.1 are characteristic for a RuO_xH_y phase.

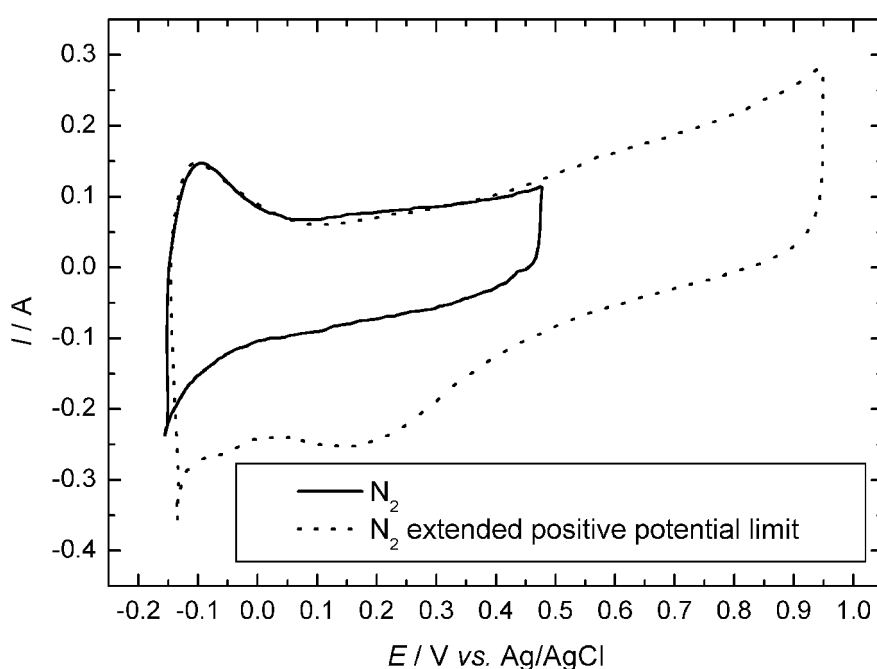


Figure 4.1. Cyclic voltammograms of unsupported PtRu catalyst at 22°C. N_2 in working electrode compartment. Sweep rate 50 mV s^{-1} . Flow rate in working electrode compartment 120 ml min^{-1} .

Experimentally, the double layer capacitance was determined from a current vs. sweep rate plot using the difference between anodic and cathodic currents at constant potential (0.1 V vs. Ag/AgCl) in order to eliminate errors due to a faradaic reaction [6] (Figure 4.2). A value of 1.1 F was obtained. Typical double layer capacitances for metal surfaces are in a range from 16 to $50 \mu\text{F cm}^{-2}$ [49]. In our case the double layer capacitance normalized per BET surface area would be $108 \mu\text{F cm}^{-2}_{\text{BET}}$. The value is probably underestimated since under fuel cell conditions usually only a part of the BET surface area is utilized (reported values are between 5 – 80 % of BET) [19,50].

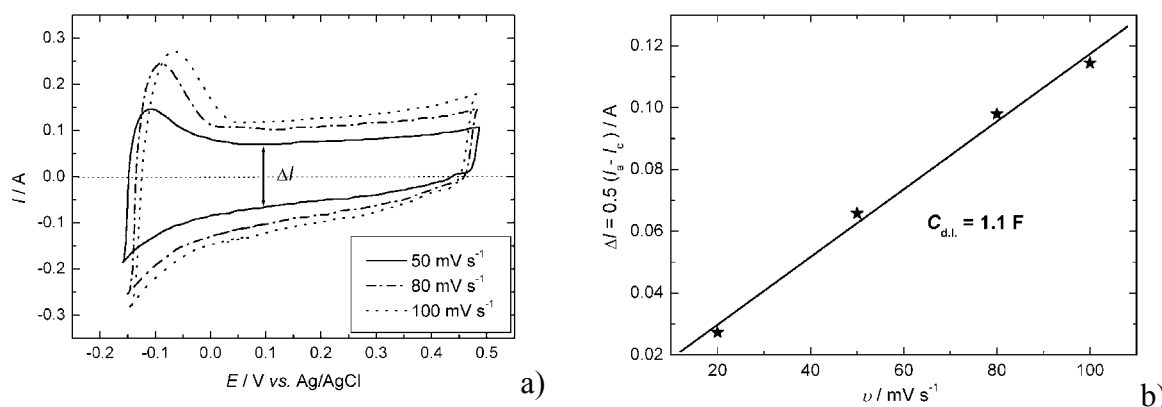


Figure 4.2 a) Cyclic voltammograms of unsupported PtRu catalyst at 22°C at different sweep rates. b) ΔI vs. sweep rate dependence. Conditions: Water in working electrode compartment; flow rate in working electrode compartment 0 l h^{-1} .

The double layer capacitance of hydrous ruthenium oxide depends on annealing temperature and preparation procedure, but can be as high as 720 F g^{-1} [48]. Normalized per BET surface area and taking into account that, as a maximum, one half of the total area corresponds to the Ru surface area (nominal PtRu composition is 1:1), the maximum pseudocapacitance for all ruthenium present as ruthenium hydroxide would be $685 \mu\text{F cm}^{-2}_{\text{BET}}$. The value found in this work lies between values for bare metal surface and for the capacitance of hydrous ruthenium oxide. This estimation suggests that a certain part of Ru in our catalyst is present in the form of Ru oxide.

The CO stripping voltammogram of the unsupported PtRu catalyst is shown in Figure 4.3. In a first positive going sweep the previously adsorbed CO is swept from the surface. The second sweep did not show any traces of CO. CO was adsorbed at 0 V vs. Ag/AgCl. The area under the peak in Figure 4.3 was integrated (see Chapter 3) and the CO stripping charge was determined. A value of $46 \mu\text{C cm}^{-2}_{\text{BET}}$ was obtained. Such a low value suggests a high level of overall catalyst oxidation [19]. Thus, only about 16 % of the catalyst's BET surface is active for CO adsorption (taking the value of $420 \mu\text{C cm}^{-2}$ for a monolayer of adsorbed CO and assuming saturated CO coverage of 0.68 (see Chapter 3)).

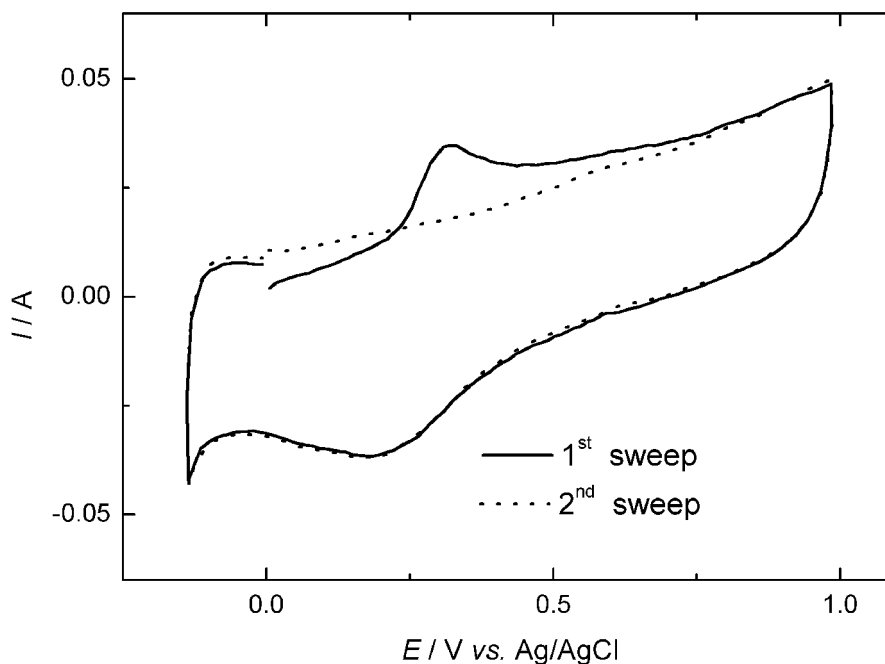


Figure 4.3. CO stripping voltammogram of unsupported PtRu catalyst. Conditions: sweep rate 5 mV s^{-1} , CO adsorption potential 0 V vs. Ag/AgCl , adsorption time 120 min , N_2 in the working electrode compartment, flow rate in working electrode compartment 120 ml min^{-1} , temperature 22°C .

4.3. Activity in methanol oxidation – Experimental findings

4.3.1. Influence of flow rate

Polarisation curves for methanol oxidation at unsupported PtRu catalyst are shown in Figure 4.4. The flow rate in the working electrode compartment was varied between 10 and 20 l h^{-1} . The methanol concentration in the working electrode compartment was 1.0 M , while in the counter electrode compartment was 0 M . The data were collected in steady state experiments. Before data sampling the electrode was preconditioned, by potential cycling with a sweep rate of 20 mV s^{-1} until a steady state voltammogram was obtained. A small increase of current on flow rate in a potential region more positive than $0.2 \text{ V vs. Ag/AgCl}$ was observed. In order to quantify this influence the relevance of the mass transfer resistance within the catalyst layer (CL) was evaluated by means of the Damköhler number of second kind Da_{II} (equation 4.43). Estimation was done for the flow rate of 10 l h^{-1} , since diffusion limitations should be more pronounced at lower flow rates.

$$Da_{II} = \frac{d^{CL} \cdot j / (6F)}{c_{\text{CH}_3\text{OH}} \cdot D_{\text{CH}_3\text{OH}}^{CL}} \sim \frac{\text{resistance of diffusion in CL}}{\text{resistance of electrochemical reaction}} \quad (4.43)$$

d^{CL} is thickness of catalyst layer (ca. $35 \mu\text{m}$), j - current density applied ($1.78 \times 10^3 \text{ A m}^{-2}$ for flow rate 10 l h^{-1}), $c_{\text{CH}_3\text{OH}}$ - methanol bulk concentration (1.0 M) and $D_{\text{CH}_3\text{OH}}^{CL}$ - methanol

diffusion coefficient in CL ($3.197 \cdot 10^{-9} \text{ m}^2 \text{ s}^{-1}$ at 60°C [51]). It was assumed that the methanol diffusion coefficient is the same as in the bulk phase. Using the data given above, Damköhler number of $Da_{II} \approx 0.036$ was calculated. This value is significantly below one, which indicates that the rate limiting process in the catalyst layer is the electrochemical reaction, and not pore diffusion.

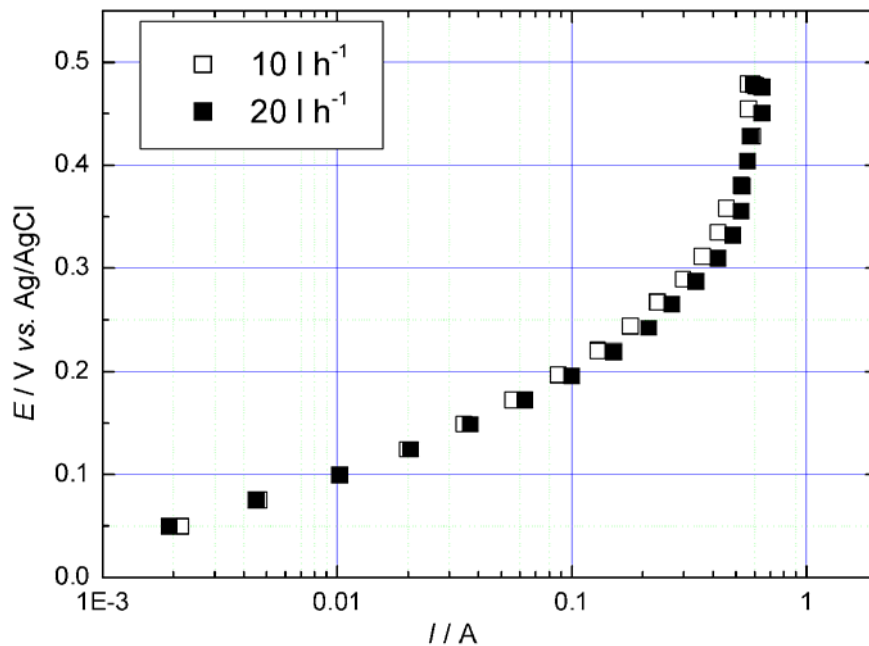


Figure 4.4 Steady state polarisation curves for methanol oxidation at unsupported PtRu catalyst. Conditions: fixed delay 5 min, 1.0 M methanol in working electrode compartment, 60.9°C , different flow rates in working electrode compartment.

The relevance of the mass transport resistance in the back diffusion layer (BDL) was estimated by means of the following Biot number:

$$Bi_m^{\text{BDL/CL}} = \frac{D^{\text{CL}} / d^{\text{CL}}}{D^{\text{BDL}} / d^{\text{BDL}}} \sim \frac{\text{resistance of diffusion in BDL}}{\text{resistance of diffusion in CL}} \quad (4.44)$$

where D^{CL} is the methanol diffusion coefficient in CL (ca. $10^{-9} \text{ m}^2 \text{ s}^{-1}$), d^{CL} the thickness of catalyst layer (ca. $35 \mu\text{m}$), D^{BDL} the methanol diffusion coefficient in BDL (ca. $10^{-9} \text{ m}^2 \text{ s}^{-1}$) and d^{BDL} the thickness of back diffusion layer (ca. $100 \mu\text{m}$). Assuming that the diffusion coefficients in the two layers are of similar magnitude, one can see that the diffusion layer resistance is of higher importance due to the fact that the BDL is about 3 times thicker than the CL, *i.e.* $Bi_m^{\text{BDL/CL}} \approx 3$.

In a similar manner, the relevance of the external film resistance can be estimated in relation to the resistance exerted by the back diffusion layer. For this purpose, the following Biot number was applied:

$$Bi_m^{L/BDL} = \frac{D^{BDL} / d^{BDL}}{k_m} \sim \frac{\text{resistance of external film diffusion}}{\text{resistance of diffusion in BDL}} \quad (4.45)$$

where k_m is the external film mass transport coefficient. The mass transfer coefficient can be calculated from the following correlation equation, which was determined for the cyclone flow cell [3]:

$$Sh = 0.0136 \cdot Re^{2/3} Sc^{1/3} \quad (4.46)$$

Equation (4.46) is valid for $Re > 10^3$ and $Sc \geq 1$. The Reynolds number is defined as [3]:

$$Re = \frac{\omega r^2 \rho}{\mu} \quad (4.47)$$

where ρ is fluid density in kg m^{-3} , μ the viscosity in Pa s^{-1} , r the electrode radius (here $r = 8.0$ mm) and ω can be expressed as:

$$\omega = \frac{4r_{in}^{1/2}}{\pi r^{3/2} d_{in}^2} \cdot V \quad (4.48)$$

In equation (4.48), r_{in} is the cyclone radius at the middle of the cyclone inlet tube (here $r_{in} = 29.7$ mm), d_{in} the diameter of the inlet tube (here $d_{in} = 4.0$ mm) and V the volumetric flow rate. For flow rate 10 l h^{-1} , the Reynolds number is $Re = 7200$.

The Schmidt number in equation (4.46) is defined as:

$$Sc = \frac{\mu}{\rho \cdot D} \quad (4.49)$$

where D stands for the diffusion coefficient of methanol in water. Using the value for $D = 3.197 \times 10^{-9} \text{ m}^2 \text{ s}^{-1}$ [51], the mass transfer coefficient at a flow rate of 10 l h^{-1} is calculated to be $k_m = 1.1 \times 10^{-5} \text{ m s}^{-1}$. Using the values given above, one gets a Biot value of $Bi_m^{L/BDL} \approx 3$, which indicates that the diffusion resistance in the BDL is three times greater than the diffusion resistance in the external film layer even for the lowest flow rate applied (10 l h^{-1}).

Multiplying Da_{II} with the Biot numbers defined above yields the reaction rate in relation to the mass transfer rates:

$$DaII \cdot Bi_m^{BDL/CL} \approx 0.11 \sim \frac{\text{resistance of diffusion in BDL}}{\text{resistance of electrochemical reaction}} \quad (4.50)$$

$$DaII \cdot Bi_m^{BDL/CL} \cdot Bi_m^{L/BDL} \approx 0.33 \sim \frac{\text{resistance of external film diffusion}}{\text{resistance of electrochemical reaction}} \quad (4.51)$$

According to the estimated dimensionless parameter groups, all external and internal mass transfer resistances are three to ten times smaller than the reaction resistance. Similar results were obtained in previous work [35] at room temperature where the increase of the current in a more positive potential region (from 0.3 to 0.5 V vs. Ag/AgCl) was obtained in experiments at enhanced flow rate, but only in comparison to quiet electrolyte. The current increase by stirring was about 20 % which was consistent with the mass transfer resistance evaluation by using dimensionless criteria. This showed that external and internal mass transfer resistances were about five to ten times smaller compared to the reaction resistance. Varying the flow rate (from 10 to 30 l h⁻¹) did not lead to a significant increase of the observed current since the resistance of external film diffusion was comparable with the resistance of diffusion in back diffusion layer, *i.e.* $Bi_m^{L/BDL} \approx 1$. For $Bi_m^{L/BDL} \approx 3$ the influence of the flow rate is even less and the differences observed (Figure 4.4) are in order of magnitude of the experimental error (see for example Figure 4.6). In conclusion, according to these data, the limiting current being observed in the potential region from 0.3 to 0.5 V vs. Ag/AgCl is not governed by mass transfer.

4.3.2. Influence of methanol concentration

The influence of the methanol concentration was investigated in the concentration range from 0.03 to 3 M methanol in water at 60.9°C (Figure 4.5). The flow rate in the working electrode compartment was 10 l h⁻¹. In these experiments, methanol was supplied to both compartments (working and counter) with the same concentration in order to avoid a methanol concentration gradient at the MEA. When the methanol concentration in the counter electrode compartment was 0, the concentration of methanol in the catalyst layer was significantly different from the bulk concentration and the observed currents were lower (Figure 4.6). It was shown above that every layer (catalyst, back diffusion and external film) imposes some diffusion limitations due to its finite thickness.

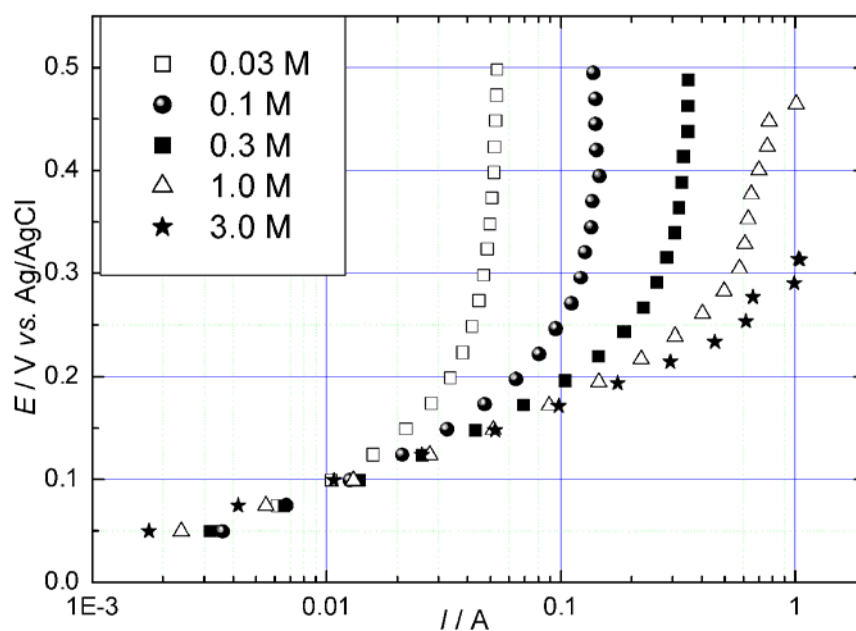


Figure 4.5. Tafel plots for methanol oxidation at unsupported PtRu catalyst. Conditions: fixed delay of 5 min, methanol concentrations from 0.03 to 3 M both in the working and counter electrode compartments, 60.9°C; flow rate in working electrode compartment 10 l h⁻¹.

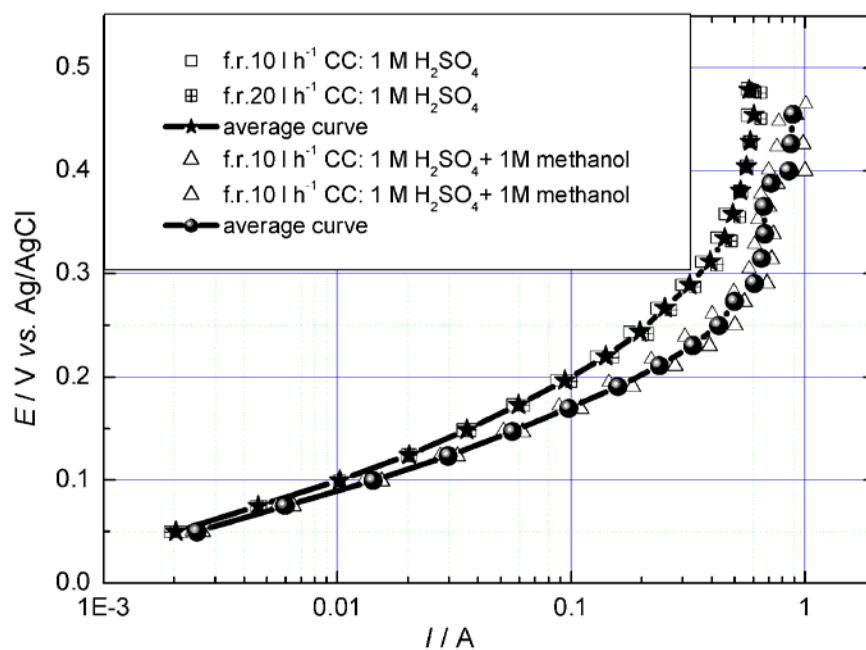


Figure 4.6 Tafel plots for methanol oxidation at unsupported PtRu catalyst. Conditions: fixed delay of 5 min, methanol concentrations in working electrode compartment 1M; methanol concentration in counter electrode compartment (CC) in one case 0 and in second case 1M, 60.9°C; flow rates in working electrode compartment indicated in Figure.

The influence of methanol concentration was especially pronounced at higher potentials (from 0.2 to 0.5 V vs. Ag/AgCl), assigned to as the limiting current region, than at lower potentials (from 0 to 0.2 V vs. Ag/AgCl) assigned to as the activation controlled region. In the latter region, Tafel slopes were determined to be 113 mV dec⁻¹ for 0.03 M solution and

69 mV dec⁻¹ for 3 M methanol solution. In order to obtain a formal reaction order with respect to methanol, the methanol oxidation rate at constant potential was plotted as a function of the methanol concentration in logarithmic coordinates. As can be seen from Figure 4.7, in the activation controlled region (at 0.15 V vs. Ag/AgCl) the reaction order changes from about 0.3 at low concentrations to 0 at higher concentrations, while at the beginning of the limiting current region (at 0.3 V vs. Ag/AgCl) the variation of the reaction order is less pronounced and the mean value is about 0.7.

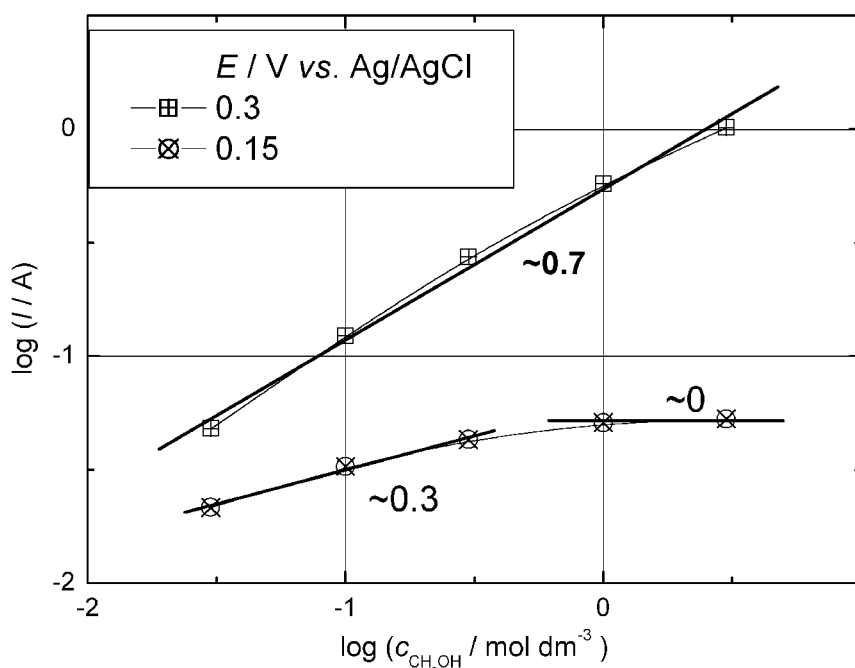


Figure 4.7. Methanol oxidation currents at constant potentials as a function of methanol concentration at 60.9°C. Data taken from Figure 4.5. Conditions: same as in Figure 4.5.

4.3.3. Electrochemical impedance spectroscopy

Kinetic parameters of an electrochemical reaction can be extracted from electrochemical impedance spectra as well. In order to do that, experimental data should be simulated by equivalent circuits and/or mathematical models. In this work an attempt was to simulate steady state potentiostatic data, so impedance spectra are presented and used in a qualitative way. Here, they are used as another piece of evidence for selection of the mechanism for methanol oxidation. Thus, a set of impedance spectra in the activation controlled region and in a frequency range from 2 kHz - 10 mHz at 60°C was recorded and the spectra are presented in Figure 4.8.

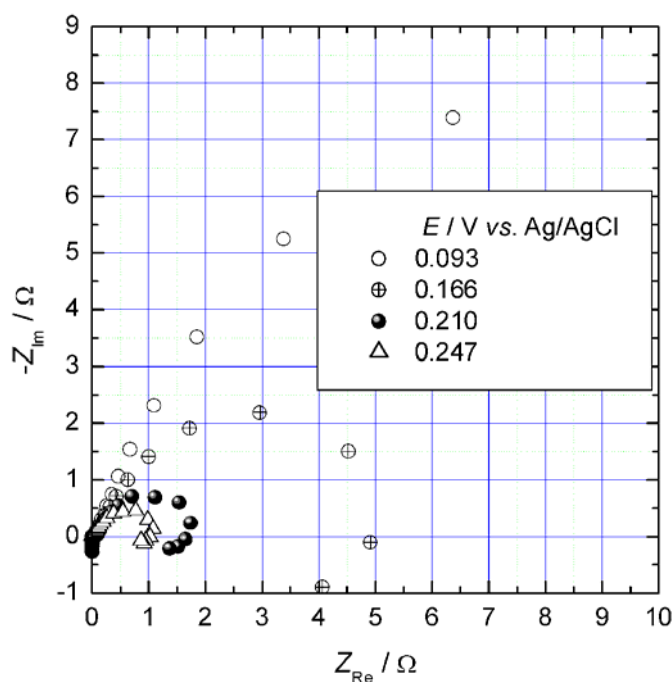


Figure 4.8 Experimental impedance plots for an unsupported PtRu catalyst at different potentials. Conditions: 1 M methanol in working electrode compartment; flow rate 10 l h^{-1} ; 60°C , frequency range 2 kHz – 10 mHz.

All impedance spectra and the potentials given in Figure 4.8 are compensated for the ohmic drop contribution. Impedance plots (except at lowest potential value *i.e.* 0.093 V vs. Ag/AgCl) consist each of a depressed semicircle and a low frequency inductive loop. Depressed semicircles characterise surfaces with a high roughness [52]. Increasing the potential, the diameter of the semicircle decreases which indicates that the charge transfer resistance for methanol oxidation becomes smaller. Pseudo-inductive behaviour in the low frequency region has been reported in literature for methanol oxidation at smooth polycrystalline platinum [53], at carbon-supported Pt-nanoparticles [54] and at Pt/Ru fuel cell anodes [55]. Such pseudo-inductive patterns are known to be typical feature of systems with adsorbed intermediates or with a transition between a passive and an active state [56]. It is explained that an initially adsorbed CO layer generated from methanol dehydrogenation covers the reaction sites. When some of the weakly adsorbed CO is oxidized, adsorption and subsequent methanol oxidation takes place on the adsorption sites which are set free. Thus, pseudo-inductive patterns could diagnose the process of CO removal from the surface.

4.3.4. Influence of temperature

The influence of temperature on the kinetics of methanol oxidation was investigated in the temperature range from 22.8 °C to 60.05 °C (Figure 4.12). In these experiments the methanol concentration was kept constant (1 M) in both compartments (working and counter electrode) and the flow rate in working electrode compartment was 10 l h⁻¹. In the activation controlled region (from 0.05 to 0.25 V vs. Ag/AgCl) straight lines with slopes from 94 mV dec⁻¹ at room to 83 mV dec⁻¹ at 60.05 °C were obtained. In the higher potential region (from 0.25 to 0.5 V vs. Ag/AgCl) limiting current behaviour was observed.

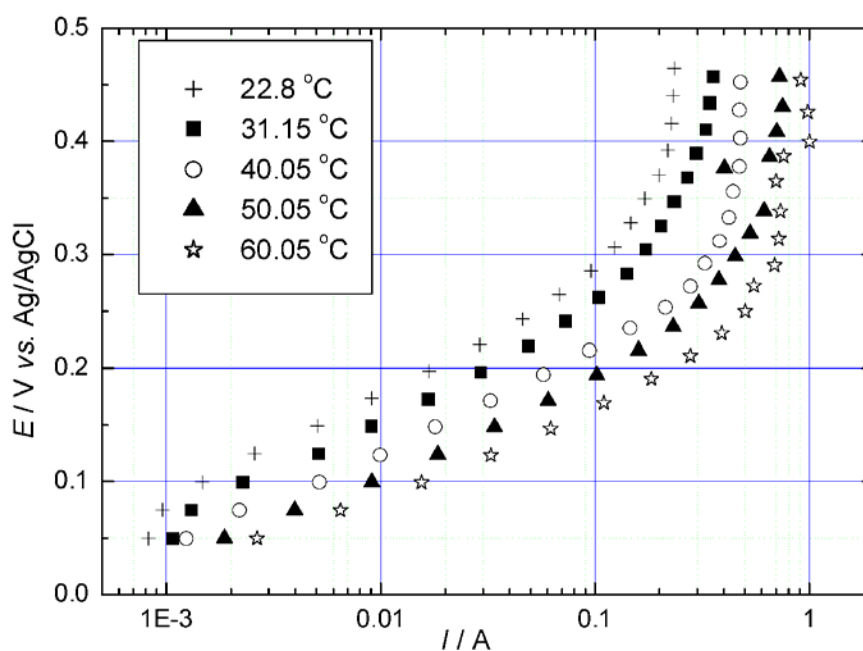


Figure 4.9 Tafel plots for methanol oxidation at unsupported PtRu catalyst. Conditions: fixed delay 5 min, methanol concentration 1 M both in working and counter electrode compartments.

Corresponding Arrhenius plots for the recorded currents in the activation controlled region and in the limiting current region are given in Figure 4.10. The apparent activation energies are calculated from the slopes of the lines in Figure 4.10.

In Table 4.1 the apparent activation energies are given with standard deviations. The calculated mean value in the activation controlled region is 56 ± 2 kJ mol⁻¹. Values reported in literature are 29 kJ mol⁻¹ at unsupported PtRu with 52 at % Ru [37], 35-40 kJ mol⁻¹ [34] and 70 kJ mol⁻¹ [23] at carbon supported PtRu with nominally 50 at % Ru, 60 kJ mol⁻¹ at a PtRu alloy with 46 at % Ru and 30 kJ mol⁻¹ at a PtRu alloy with 7 at % Ru [45]. Low values of the apparent activation energies are ascribed to heterogeneous electrocatalytic processes [37], mixed activation-adsorption control [34] or CO surface diffusion [45]. High apparent

activation energy values are ascribed to dissociative adsorption of methanol [45] or to the reaction between adsorbed CO and OH [23] as rate determining step.

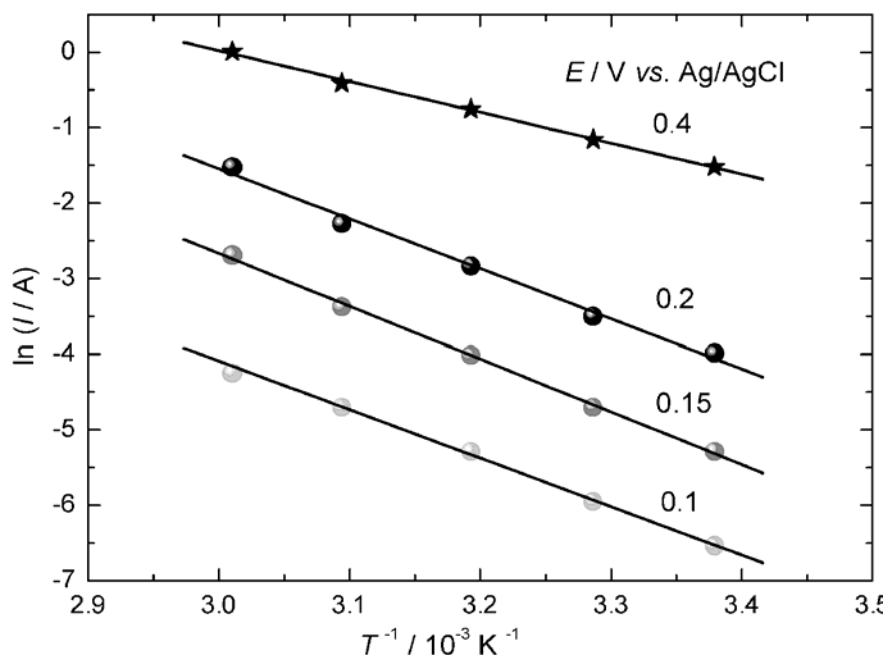


Figure 4.10 Arrhenius plots for methanol oxidation at unsupported PtRu catalyst based on the data in Figure 4.9. Conditions: fixed delay 5 min, methanol concentration 1 M both in working and counter electrode compartments, temperature range 22.8 - 60.9°C.

Table 4.1 Calculated values of apparent activation energy at different potentials.

<i>E</i> / V vs. Ag/AgCl	<i>E_a</i> / kJ mol ⁻¹
0.10	58±4
0.15	54±3
0.20	55±7
0.40	34±3

Assigning the apparent activation energy to a single rate determining step in a complex reaction mechanism is difficult without taking into account additional kinetic parameters (like apparent reaction order, Tafel slope, surface coverage of adsorbed species, etc.). In reference [45], the low coverage with CO_{ads} at a PtRu alloy with 46 *at* % Ru and an apparent activation energy of 60 kJ mol⁻¹ were in favor of the methanol dissociative electroadsorption as rate determining step ((CH₃OH)_{sol} → → CO_{ads} + 4H⁺ + 4e⁻). A high coverage by CO_{ads}, but a low apparent activation energy value in case of PtRu alloy with 7 *at* % Ru in the same study [45] hypothesized CO_{ads} surface diffusion from Pt to Ru site where the OH_{ads} nucleation occurs as rate determining step. In reference [37], an apparent activation energy of 29 kJ mol⁻¹ is assigned to a heterogeneous electrocatalytic process as r.d.s, which is according

to the authors' reaction scheme the dissociative adsorption of methanol, *i.e.* the same r.d.s as in reference [45] for an alloy with a high Ru content (46 at %). In [34] a low apparent activation energy, a Tafel slope of 155-168 mV dec⁻¹ and a formal reaction order with respect to methanol of 0.5 determined the mixed activation-adsorption control¹⁸ and the activation controlled step to the reaction between CO_{ads} and OH_{ads} (like in [23])). Finally in reference [23], a transfer coefficient of 0.5, a reaction order with respect to methanol of 0.5, a strong correlation between the methanol oxidation rate and the pseudocapacitive current of OH adsorption on Ru was found. The apparent activation energy of 70 kJ mol⁻¹ leads to the conclusions that the reaction between CO_{ads} and OH_{ads} is the r.d.s.

4.4. Mechanism and rate expression for methanol oxidation

Based on the experimental findings in this work:

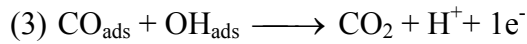
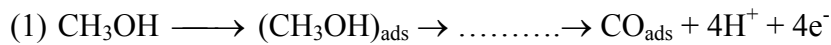
- limiting current is not governed by external mass transport,
- Tafel slope ($\sim 70 - 113 \text{ mV dec}^{-1}$),
- reaction order with respect to methanol in activation controlled region: between 0.3 at lower methanol concentrations and 0 at higher methanol concentrations and in limiting current region: ~ 0.7 ,
- pseudo inductive loop in the low frequency region which implies that adsorbed intermediates are involved,

and literature findings:

- methanol oxidation occurs through several steps *i.e.* methanol adsorption, transformation of methanol adsorbate by H-atom extraction and intermediate formation,
- CO was detected by FTIR [23], [57] and by Single Potential Alteration Infrared Spectroscopy (SPAIRS) [58] as a stable intermediate,
- OH species formation by water dissociative adsorption,
- reaction between adsorbed OH and adsorbed CO, CO₂ evolution and finally the surface is set free for a new methanol adsorption step to take place,

¹⁸ In this study the meaning of adsorption control step was not clearly specified; indirectly it can be concluded that the adsorption controlled step refers to methanol dissociative adsorption (like in references [37] and [45]).

the following mechanism of methanol oxidation is selected (see Gasteiger *et al.* [32]):



In order to derive a rate expression for this methanol oxidation mechanism the following assumptions are applied:

- Langmuir adsorption isotherm is valid for all species.
- Steady state conditions are applied, *i.e.* $\frac{dX}{dt} = 0$ for all dynamic state variables.
- Water dissociative adsorption, *i.e.* step 2 of the mechanism is in electrochemical equilibrium.
- In the mechanism presented above the first reaction is a consecutive reaction, for which the first step (potential independent physical methanol adsorption) is considered to be the r.d.s.
- According to the bifunctional mechanism, it is assumed that methanol adsorbs only at Pt, while OH is formed only on Ru adsorption sites (formation of Pt-OH_{ads} occurs at potentials higher than 0.5V). Thus, $(1-\theta_{\text{CO}})$ is the fraction of the Pt surface being free for methanol adsorption and $(1-\theta_{\text{OH}})$ is the fraction of Ru adsorption sites being free for water decomposition.

Before proceeding further, it should be mentioned that a similar mechanism of methanol oxidation was used in reference [59] to derive a rate expression for methanol oxidation but, with different assumptions. The major difference is that in reference [59] at high overpotentials methanol diffusion to the surface was proposed to be the *r. d. s.*, while in our case it is methanol adsorption.

Now rate expressions for each step are formulated:

$$r_1 = k_1 \cdot c_{\text{CH}_3\text{OH}} (1 - \theta_{\text{CO}}) \quad (4.52)$$

$$r_2 = k_2 \cdot c_{\text{H}_2\text{O}} \cdot (1 - \theta_{\text{OH}}) \cdot e^{\alpha_2 FE / RT} - k_{-2} \cdot c_{\text{H}^+} \cdot \theta_{\text{OH}} \cdot e^{-(1-\alpha_2) FE / RT} \quad (4.53)$$

$$r_3 = k_3 \cdot \theta_{\text{CO}} \cdot \theta_{\text{OH}} \cdot e^{\alpha_3 FE / RT} \quad (4.54)$$

For simplicity the charge transfer coefficient α_3 in the following text is replaced by α .

According to assumption b):

$$Q \frac{d\theta_{\text{CO}}}{dt} = r_1 - r_3 = 0; \quad \text{or} \quad k_1 c_{\text{CH}_3\text{OH}} (1 - \theta_{\text{CO}}) = k_3 \theta_{\text{CO}} \theta_{\text{OH}} e^{\alpha FE/RT} \quad (4.55)$$

where Q is charge necessary to oxidize full monolayer of CO adsorbed. It is introduced in order to have dimension homogenous expression (r_1 and r_3 in equations (4.52) and (4.53) are expressed as currents).

According to assumption c):

$$k_2 c_{\text{H}_2\text{O}} (1 - \theta_{\text{OH}}) e^{\alpha_2 FE/RT} = k_{-2} c_{\text{H}^+} \theta_{\text{OH}} e^{-(1-\alpha_2) FE/RT} \quad (4.56)$$

$$\text{or } B = \frac{k_2 c_{\text{H}_2\text{O}}}{k_{-2} c_{\text{H}^+}} = \frac{\theta_{\text{OH}}}{1 - \theta_{\text{OH}}} e^{-FE/RT} \quad (4.57)$$

where B is constant, since water and H^+ concentrations are constant.

From these equations the intermediate adsorbed species can be determined as a function of potential, concentration and temperature:

$$\theta_{\text{CO}} = \frac{k_1 \cdot c_{\text{CH}_3\text{OH}}}{k_1 \cdot c_{\text{CH}_3\text{OH}} + k_3 \cdot \theta_{\text{OH}} \cdot e^{\alpha FE/RT}} \quad \text{and} \quad \theta_{\text{OH}} = \frac{B \cdot e^{FE/RT}}{1 + B \cdot e^{FE/RT}} \quad (4.58)$$

Equation (4.55) reflects the stationarity of the process. So, the overall reaction rate can be expressed by r_1 or r_3 , and the electric current (6 electrons) is given by:

$$I = 6r_3 = 6k_3 \frac{(k_1/k_3) c_{\text{CH}_3\text{OH}}}{1 + \frac{(k_1/k_3) c_{\text{CH}_3\text{OH}} (1 + B \cdot e^{FE/RT})}{B \cdot e^{(1+\alpha) FE/RT}}} \quad (4.59)$$

Equation (4.59) is used to determine the reaction order with respect to methanol:

$$a_{\text{CH}_3\text{OH}} = \frac{\partial \log I}{\partial \log c} = 1 - \left(1 + \frac{B \cdot e^{(1+\alpha) FE/RT}}{(k_1/k_3) c_{\text{CH}_3\text{OH}} (1 + B \cdot e^{FE/RT})} \right)^{-1} \quad (4.60)$$

Equation (4.60) shows that this reaction order depends on both concentration and potential and can have values between 0 (high concentrations, negative potentials) and 1 (low concentrations, positive potentials), which is in accordance with our experimental results (values between $a_{\text{CH}_3\text{OH}} = 0$ for 3M and 0.3 for 0.03M at 0.15V; about 0.7 at 0.3V).

A similar determination of the Tafel slope gives:

$$\text{Tafel slope} = \frac{\partial E}{\partial \log I} = \frac{2.3RT}{F} \frac{(B \cdot k_3 / (k_1 c_{\text{CH}_3\text{OH}})) e^{(1+\alpha)FE/RT} + (1 + B \cdot e^{FE/RT})}{1 + \alpha(1 + B \cdot e^{FE/RT})} \quad (4.61)$$

Equation (4.61) yields values between $2.3RT/(1+\alpha)F = 44 \text{ mV}$ (60°C , $\alpha = 0.5$) at low overpotentials ($B \cdot e^{FE/RT} \ll 1$; $(B \cdot k_3 / (k_1 c_{\text{CH}_3\text{OH}})) e^{(1+\alpha)FE/RT} \ll 1$) and infinity at very high overpotentials.

For the intermediate region ($B \cdot e^{FE/RT} \gg 1$, but $(k_3 / (k_1 c_{\text{CH}_3\text{OH}})) e^{\alpha FE/RT} \ll 1$), a Tafel slope of $2.3RT/\alpha F = 132 \text{ mV}$ (60°C , $\alpha = 0.5$) should appear.

4.5. Simulated vs. experimental data

Simulated and experimental curves at different methanol concentrations are shown in Figure 4.7. According to the model and the chosen parameters ($B=10$ and $k_1/k_3 = 10$) the slope of the $E - \log(I)$ correlation changes from 44 mV dec^{-1} at low overpotentials, to infinity at high overpotentials. In the region of the low slope value, the model predicts no concentration dependence *i.e.* the reaction order with respect to methanol is zero. Under certain conditions (depends on the ratio of the rate constants k_1 and k_3 and methanol concentration) a slope of 132 mV dec^{-1} in the intermediate potential region should appear (at low methanol concentrations this slope is not obvious Figure 4.11). Finally, the reaction rate becomes limited only by the kinetics of methanol adsorption, which is assumed to be potential independent. The comparison of the experimental and the simulated curves reveals good qualitative agreement.

From the data in Figure 4.11, values for simulated reaction order can be determined (see Figure 4.12). Again a good qualitative agreement is obtained, when comparing the experimental with the simulated results (Figure 4.12).

As discussed above, assigning the apparent activation energy to one single step in a reaction mechanism is often difficult. In our case, in assigning the different apparent activation energies to different reaction steps in the selected mechanism, analysis of the rate equation (4.59) proved helpful. At first, the rate expression (4.59) is simplified in different potential regions. The following cases can be distinguished:

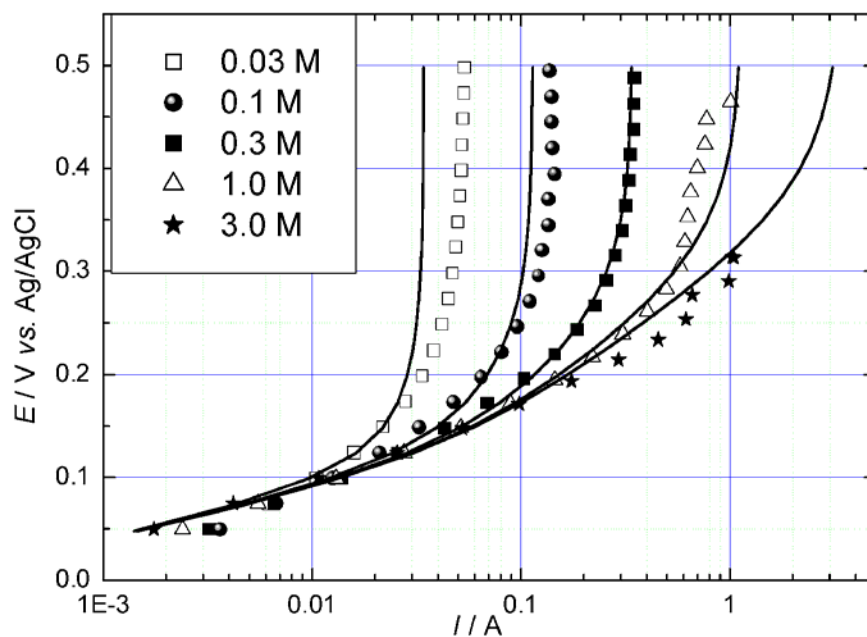


Figure 4.11. Experimental and simulated (full lines) steady state curves for methanol oxidation. Conditions experimental data (same as in Figure 4.5); simulated data: methanol concentrations from 0.03 to 3 M, 60.9°C, $B=10$, $k_1/k_3 = 10$.

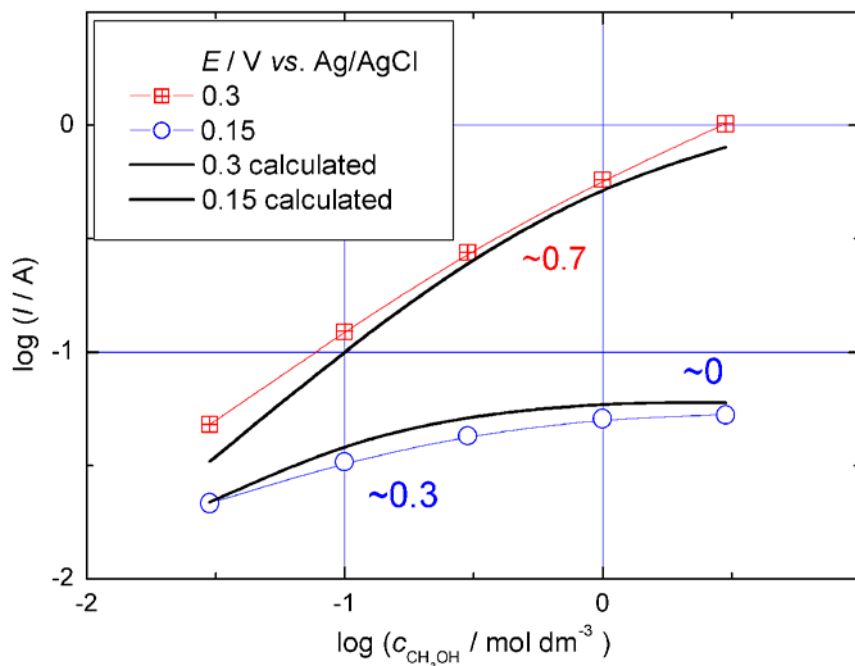


Figure 4.12 Experimental and simulated (full lines) methanol oxidation currents at constant potentials as a function of methanol concentration at 60.9°C. Data taken from Figures 4.5 and 4.8. Conditions: same as in Figures 4.5 and 4.8.

a) very low overpotentials ($B \cdot e^{FE/RT} \ll 1$; $B \cdot e^{(1+\alpha)FE/RT} \ll k_1 c_{\text{CH}_3\text{OH}} / k_3$). The rate equation simplifies to:

$$I = 6Fk_3 \cdot B \cdot e^{(1+\alpha)FE/RT} \quad (4.62)$$

and the apparent activation energy is the sum of the activation energy of process (3), *i.e.* reaction between CO_{ads} and OH_{ads} , and the enthalpy of adsorption of process (2), *i.e.* formation of OH_{ads} . So in this potential region these processes determine the overall reaction rate. The reaction order with respect to H^+ should be -1.

b) moderate overpotentials ($B \cdot e^{FE/RT} \gg 1; e^{\alpha FE/RT} \ll k_1 \cdot c_{\text{CH}_3\text{OH}} / k_3$) the rate expression becomes:

$$I = 6Fk_3 \cdot e^{\alpha FE/RT} \quad (4.63)$$

and the apparent activation energy coincides with $E_{a,3}$. No influence of the pH value is expected.

c) at very high overpotentials ($B \cdot e^{FE/RT} \gg 1; e^{\alpha FE/RT} \gg k_1 \cdot c_{\text{CH}_3\text{OH}} / k_3$) the limiting current is deduced:

$$I = 6Fk_1 c_{\text{CH}_3\text{OH}} \quad (4.64)$$

and the apparent activation energy is $E_{a,1}$.

To summarize, according to the here proposed model, at moderate overpotentials (from 0.05 to 0.25 V *vs.* Ag/AgCl) the reaction rate is dominated by activation control (step 3 in the reaction scheme) and the obtained activation energy value of $56 \pm 2 \text{ kJ mol}^{-1}$ seems reasonable for such a reaction step. At very high overpotentials (from 0.25 to 0.5 V *vs.* Ag/AgCl) the reaction is dominated by the kinetics of methanol adsorption, *i.e.* the overall reaction is under reaction control (step 1 in the reaction scheme) and the obtained apparent activation energy of $34 \pm 3 \text{ kJ mol}^{-1}$ is reasonable for such an adsorption process.

Calculated and experimental curves for methanol oxidation as a function of temperature are shown in Figure 4.13. The rate constants for the calculated curves are determined by using the experimental values for the activation energies. As pointed out before, the model predicts Tafel slope values ranging from (40-44) mV dec^{-1} to infinity. The low Tafel slope value, at low overpotentials is not shown in the calculated plots, since it was not experimentally validated. As it was mentioned above at moderate overpotentials the appearance of another Tafel slope whose value depends on the ratio of the rate constants k_1 / k_3 and the methanol concentration is possible (Figure 4.13). When comparing experimental and simulated curves in Figure 4.13, a good agreement is gained.

Finally, concluding from the given temperature and concentration investigations, the rate determining step changes in different potential regions and at different concentrations. In Table 4.2 a summary of the predicted kinetic parameters according to the reaction scheme is given.

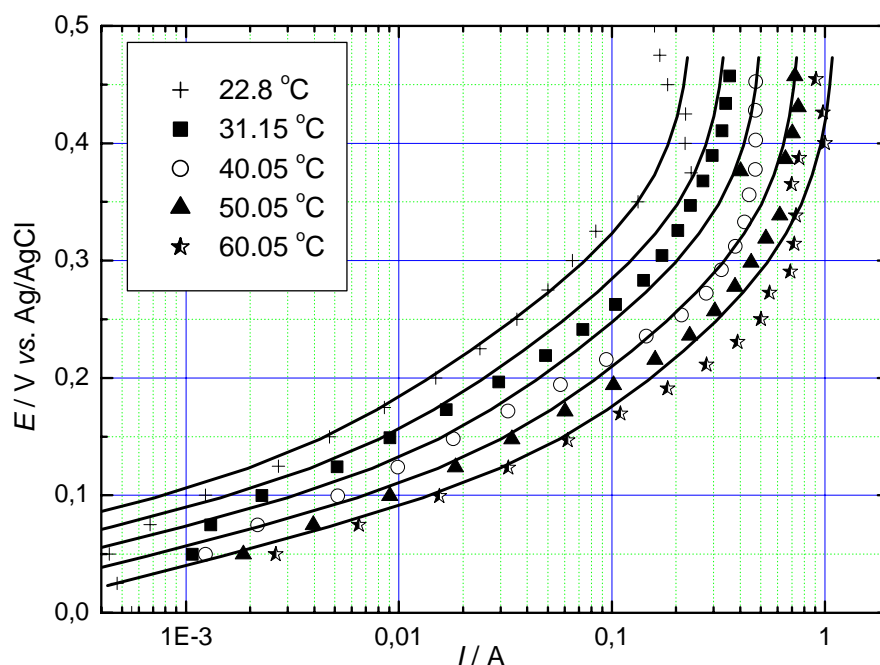


Figure 4.13 Experimental and simulated (full lines) steady-state curves for methanol oxidation. Conditions: experimental data: same as in Figure 4.9; simulated data: methanol concentration 1 M, $B = 10$, $k_1/k_3 = 10$ at 60 °C. Activation energies $E_1 = 34 \text{ kJ mol}^{-1}$; $E_3 = 56 \text{ kJ mol}^{-1}$; $\Delta H_{\text{ads}} = 0$.

In the preceding text all experimental data were collected in experiments using unsupported PtRu catalyst with a metal loading of 5 mg cm^{-2} . This metal loading is rather high and would increase the costs of the DMFC. The metal loading can be varied in a fuel cell. In a next section the influence of the metal loading on methanol oxidation will be shown by comparing the MEA performance towards methanol oxidation for two metal loadings (1 and 5 mg cm^{-2}). When the catalyst is supported on a cheap electron conducting support (like carbon black) a high catalyst dispersion can be achieved at low metal loading. One aim is to create a metal active surface area with a reduced metal loading¹⁹ and consequently lower costs. Thus, a comparison between supported and unsupported PtRu catalyst with the same metal loading (1 mg cm^{-2}) will be also given. The question is whether these two parameters influence the cell performance only through a change of the active surface area or whether

¹⁹ In general, supported catalysts are characterized by lower particle size, compared to unsupported catalysts, even when they are prepared by the same method, as will be shown in Chapter 5.

there are some additional effects that should be encountered in the reaction mechanism (for example a change of the mechanism in the case of supported catalyst due to catalyst support effects).

Table 4.2: Kinetic parameters to be expected for the reaction scheme in different potential regions

overpotential region	“low”	“moderate”	“high”
Tafel slope/ mV dec^{-1}	44	132	infinity
reaction order of CH_3OH	0	0	1
reaction order of H^+	-1	0	0
app. activation energy $E_{a, \text{app}}$	$E_{a,3} + \Delta H_{\text{ads}}$	$E_{a,3}$	$E_{a,1}$
rate determining step	(3), (2)	(3)	(1)

4.6. Influence of PtRu loading

The influence of the PtRu loading on methanol oxidation was investigated for two different metal loadings 1 and 5 mg cm^{-2} . Typical metal loadings applied in the literature are: 5 mg cm^{-2} in [19,34], but also lower metal loadings (2 mg cm^{-2}) like in [60]. Thus, the chosen metal loadings in this work can be considered as lower and higher limit of typical metal loadings used in the literature.

4.6.1. Catalyst characterisation

In this case, the catalyst characterisation was performed by means of cyclic voltammetry in absence of methanol (only water in the working electrode compartment). In Figure 4.14 cyclic voltammograms of an MEA with 1 mg cm^{-2} metal loading, two MEAs with 5 mg cm^{-2} loading and an average curve for MEAs with 5 mg cm^{-2} , normalized with respect to metal loading are shown. As can be seen, in the whole potential region normalized currents for 5 mg cm^{-2} metal loading are lower than for 1 mg cm^{-2} metal loading. It can be concluded that increasing the metal loading increases the active surface area in a fuel cell but not in a linear way *i.e.* five times greater metal loading does not result in a five times greater surface area. In other words under the applied conditions the catalyst utilisation is higher at lower metal loadings.

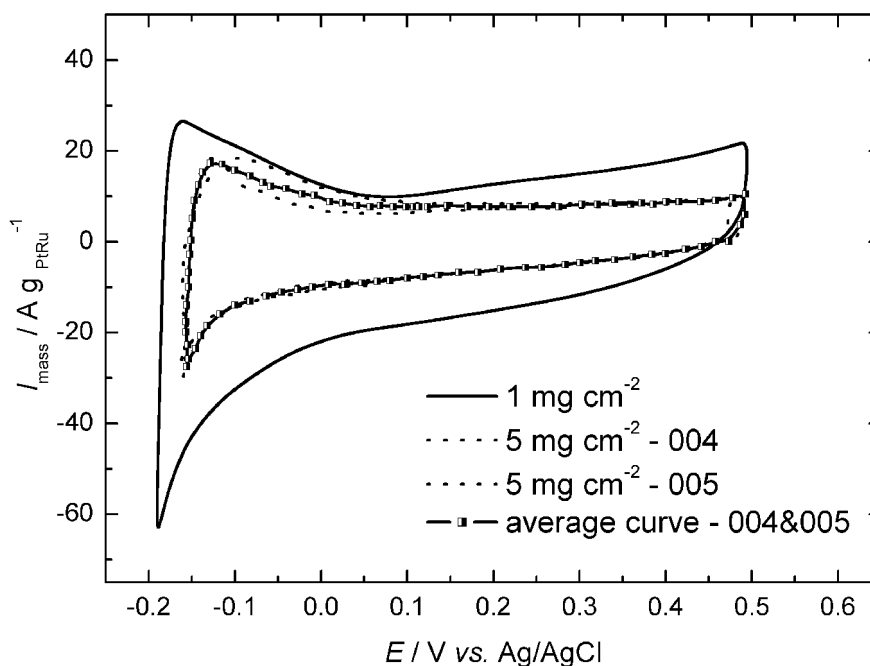


Figure 4.14 Cyclic voltammograms of MEAs with two different metal loadings at 22°C. Water in working electrode compartment. Sweep rate 50 mV s⁻¹. Flow rate in working electrode compartment 0 l h⁻¹.

4.6.2. Activity towards methanol oxidation

The activity towards methanol oxidation for two different loadings was checked at room temperature. In Figure 4.15 data for the MEA with 1 mg cm⁻² loading are collected under quasi steady state conditions (slow sweep of 1 mV s⁻¹), while for 5 mg cm⁻² metal loading under steady state conditions with a fixed delay of 5 min. Comparison between slow sweep and steady state conditions is justified as it was shown in Chapter 2. As in the case of the MEA characterisation in the absence of methanol (Figure 4.14) currents in Figure 4.15 are normalized with respect to the metal loading. Similar to the CV results in Figure 4.14 the normalized currents for 5 mg cm⁻² metal loading are lower in the whole potential range where methanol oxidation takes place than currents for lower metal loading (1 mg cm⁻²). Thus, the same conclusion as for Figure 4.14 can be drawn, *i.e.* under these conditions the catalyst utilisation is lower for higher metal loading.

4.7. Influence of support

The support can increase the catalyst dispersion by preventing particle agglomeration. Also some kind of metal/support interaction can exist as well. In this work supported and unsupported commercial PtRu catalysts with the same metal loading of 1 mg cm⁻² were characterised by cyclic voltammetry in the absence of methanol. Their activity towards methanol oxidation at room temperature (22°C) was investigated and compared.

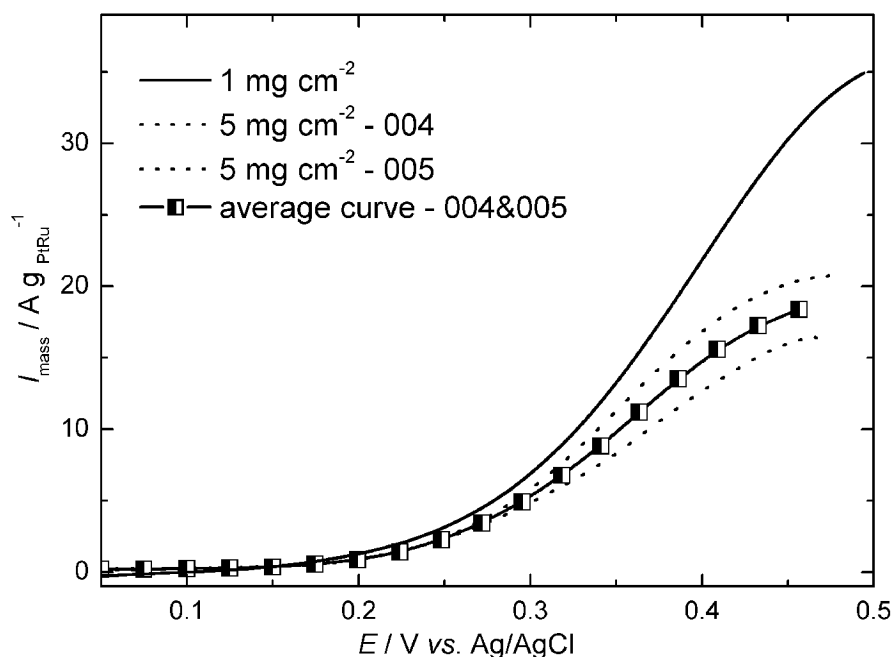


Figure 4.15 Cyclic voltammograms of MEAs with two different metal loadings at 22°C. 1 M methanol in working electrode compartment. Data are collected in a slow sweep (1 mV s^{-1}) for 1 mg cm^{-2} and under steady state conditions with fixed delay of 5 min for 5 mg cm^{-2} metal loading. Flow rate in working electrode compartment: 10 l h^{-1} .

4.7.1. Cyclic voltammetry in the absence of methanol

Cyclic voltammogram of supported and unsupported PtRu catalysts with the same PtRu loading of 1 mg cm^{-2} is shown in Figure 4.16. Currents for the supported catalyst are greater than for the unsupported sample in the whole investigated potential region. This is due to the contribution of a capacitive current that originates from the carbon support. Besides higher currents, in the case of the supported catalyst, hydrogen adsorption/desorption region is more pronounced. This may indicate a difference of the surface composition of the supported and unsupported sample (as also discussed in section 4.2 and discussed later in Chapter 5). Thus, in agreement with the previous discussion the supported sample has a surface enriched in platinum. This fact has importance for the catalyst activity towards methanol oxidation.

4.7.2. Activity towards methanol oxidation

The activity towards methanol oxidation was compared for supported and unsupported PtRu catalysts with the same PtRu loadings of 1 mg cm^{-2} at room temperature. As can be seen from Figure 4.17 the supported sample shows greater currents in the potential region where methanol oxidation takes place (starting approximately from $0.25 \text{ V vs. Ag/AgCl}$). This result is expected since some catalyst agglomeration can take place in the case of the unsupported sample which leads to a lower surface area.

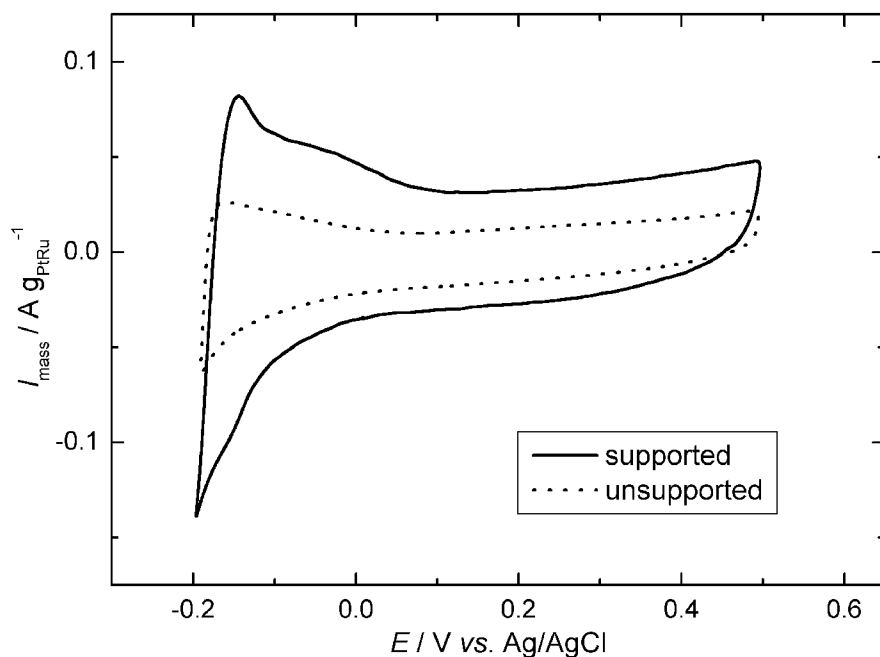


Figure 4.16 Cyclic voltammograms of MEAs prepared with supported and unsupported PtRu catalysts with the same metal loading at 22°C. Water in working electrode compartment. Sweep rate 50 mV s⁻¹. Flow rate in working electrode compartment 0 l h⁻¹.

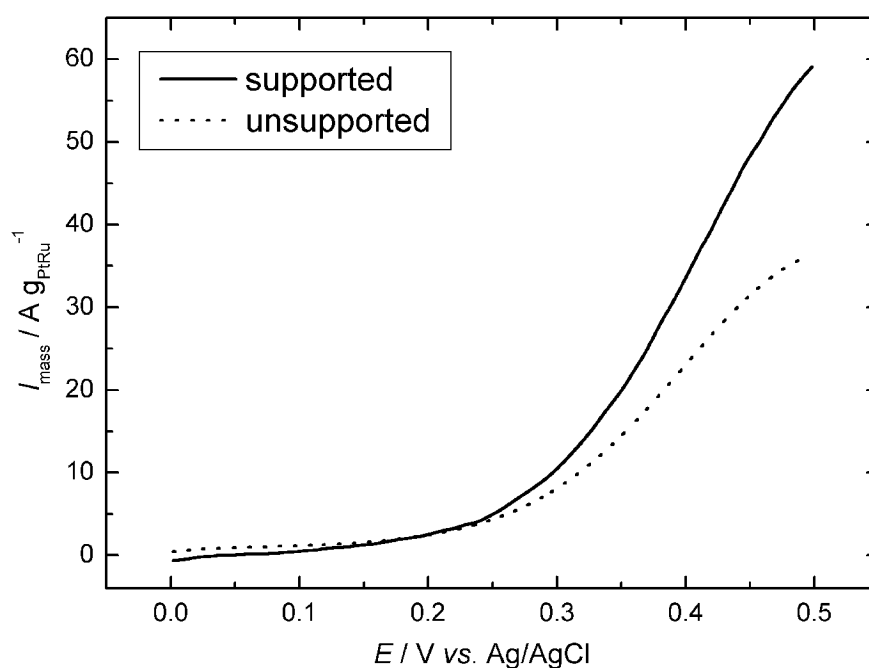


Figure 4.17 Cyclic voltammograms of MEAs prepared from supported and unsupported PtRu catalysts with a same PtRu loading of 1 mg cm⁻². Conditions: sweep rate 1 mV s⁻¹, 1 M methanol in working electrode compartment, flow rate 10 l h⁻¹, temperature 22 °C.

4.8. Conclusions

In this Chapter experimental data on the kinetics of methanol oxidation on unsupported PtRu catalyst under fuel cell relevant conditions are presented and discussed. A mechanism for

methanol oxidation is selected and a rate expression for methanol oxidation is derived. The following conclusions can be drawn:

- Catalyst characterization by cyclic voltammetry and CO stripping indicates that some amount of the catalyst is in the form of Ru-oxide.
- No influence of the flow rate was observed under the applied experimental conditions (methanol concentration 0.03 M, temperature 60.9 °C, flow rates between 10 and 20 l h⁻¹).
- The experimentally obtained reaction order with respect to methanol in the activation controlled region changes from 0.3 at low concentrations to 0 at higher concentrations, while in the limiting current region the reaction order is 0.7 in the whole concentration range.
- The apparent activation energy for methanol oxidation was determined to be 56±2 kJ mol⁻¹ in the activation controlled region and 34±3 kJ mol⁻¹ in the limiting current region.
- A rate expression for methanol oxidation is derived, and simulated plots at different methanol concentrations and temperatures are presented. The model showed good qualitative description of the experimental data.
- An influence of the metal loading and support was found only with respect to real surface area.

4.9. Outlook

In the model presented above it was assumed that Langmuir adsorption isotherm is valid for all species. The model can be improved by using another type of isotherm, which includes surface non-homogeneity and interactions between species on the catalyst surface.

The possibility of mass transfer limitations should be considered more in detail, as well.

The model could be further validated by comparing simulated and experimental impedance spectra.

5. Relation between catalyst synthesis and activity in methanol electrooxidation

The state of the art catalyst for methanol oxidation is based on a PtRu system, as discussed in detail in Chapters 1 and 4. The enhancement of the PtRu over the Pt catalyst activity can be explained by the theory of bifunctional catalysis where both the electronic effect (Ru promotes adsorption of methanol at lower potentials by providing a number of kinetically more active sites for methanol chemisorption [31]) and the ability of Ru to be oxidized at lower overpotentials than platinum itself are arguments to understand the role of Ru as a promoter. Under operating conditions of the direct methanol fuel cell (DMFC) both supported and unsupported high surface area PtRu catalysts, can be used. In Chapter 4 the kinetics of methanol oxidation on a commercial unsupported PtRu catalyst was investigated. The activity of unsupported and supported samples was also compared. It was shown that the supported catalyst has some advantages compared to the unsupported one.

In the present section, the activities of the several carbon supported catalysts synthesized by three variations of the colloidal salt reduction method towards methanol oxidation will be presented and discussed. Metal salt precursors, reducing agents and stabilizing agents were varied. In general, they can influence the mean particle size, the particle size distribution, the bulk and the surface Pt:Ru composition, the oxidation state of Pt and Ru, the extent of PtRu alloying, the distribution of the catalyst crystal surfaces and the catalyst morphology etc. These factors in turn can change the catalyst activity for methanol oxidation and contribute to different activities of catalysts with nominally the same Pt:Ru composition. Although all catalysts in this study were synthesized by the colloidal method, for the sake of completeness, a short overview of other methods for nanoparticle preparation will be given too. Catalysts are developed at the Max-Planck-Institut für Kohlenforschung in Mülheim an der Ruhr. The preparation procedure will be described here only in brief, while all details of the synthesis will be given elsewhere [61,62]. The synthesized catalysts were characterised by means of energy dispersive X-ray analysis (EDX), X-ray diffraction (XRD), transmission electron microscopy (TEM), cyclic voltammetry and CO stripping voltammetry.

Then, the activity towards methanol oxidation was compared under steady state conditions at room temperature ($21 \pm 0.5^\circ\text{C}$) and at $60 \pm 0.5^\circ\text{C}$, in “long” term stability tests (chronoamperometry) and by using electrochemical impedance spectroscopy. At the end the influence of conditioning and leaching on catalyst activity, as well as a comparison between supported and unsupported samples is given.

5.1. Methods for nanoparticle preparation

In general, the wet chemistry preparation routes can be divided into two major groups: *salt-impregnation methods* and *colloidal methods*.

The salt – impregnation route is based on the co-reduction of Pt and Ru precursors (for example H_2PtCl_6 , RuCl_3 , $\text{Pt}(\text{NH}_3)_2(\text{OH})_2$ etc) by using liquid phase reducing agents (like HCOOH , N_2H_4 , NaBH_4) or a gas phase reducing agent (H_2) [63-66]. The reduction of PtRu bimetallic precursors [67] and PtRu molecular cluster precursors [68] by hydrogen is also reported in the literature. Alternatively, a precursor of one constituent metal can be first impregnated onto a carbon support and then serve as a nucleation centre for the growth of a binary phase [69]. Pt-decorated particles can be obtained by reduction of a Pt precursor on unsupported Ru particles; which serve as nucleation centres [70]. This method can be used for the synthesis of monometallic and up to quaternary electrocatalysts. Disadvantages of this method are: a) it allows the synthesis of supported catalysts only; b) it requires a high surface area of carbon blacks that can have some disadvantages during fuel cell operation²⁰, and c) it does not allow high metal catalyst dispersion on the support in the presence of high noble metal loadings.

The colloidal route is based on the formation of metal colloids. Metal colloids are nanoparticles ranging from 1 to 50 nm and being shielded from agglomeration by protecting covering. Metal colloids can be obtained by different wet chemical synthesis methods: “top-down” and “bottom-up” [71]. The “top-down” method is based on “tearing down” bulk samples and stabilizing resulting particles (for example: mechanical grinding of bulk metals and stabilizing of resulting nanoparticles by colloidal protecting agents etc). The “bottom-up” method relies on a chemical reduction of metal salts in the presence of a stabilizing agent, on electrochemical synthesis, or on the decomposition of low valent transition metal complexes.

²⁰ High surface area carbon blacks can lead to low catalyst utilisation due to a significant amount of micropores. This is a consequence of the electrolyte’s limited access to the interior of the micropores and/or to mass transport limitations of the reactants.

Details about these methods are given in reference [71]. No matter which of the methods is used, metal colloid synthesis always takes place in the presence of a stabilizing agent, which serves partly to control the growth of primarily formed nanoclusters and mainly to prevent them from agglomeration²¹. This method can be used for the preparation of monometallic, bimetallic and trimetallic nanoparticles. Advantages of this method compared to the salt-impregnation method are: a) the size and the composition of the nanoparticles can be tailored independently of the support, b) due to the stabilizing/protecting shell particle sizes smaller than 2 nm can be obtained as well as a uniform particle size distribution, c) both unsupported and supported nanoparticles can be synthesized, d) a good catalyst dispersion even for high noble metal loadings and consequently high surface areas can be obtained. Disadvantages are: a) the protecting/stabilizing shell blocks some part of the metallic surface and consequently decreases the available surface area for the electrochemical reaction, b) the price and complexity of the overall synthesis is higher.

In the following, a “bottom-up” method of metal colloid synthesis based on *chemical reduction of metal salts* will be more elaborated. In general, metal salts are reduced in presence of a stabilizing agent and zerovalent metal colloids are generated. The approach was first published by Faraday in 1857, while the first reproducible standard recipes were established by Turkevich in 1951 ([71] and reference therein). The formation of metal colloids is explained by a mechanism where nucleation, growth and agglomeration are the major steps. This mechanism is first proposed by Turkevich, and in essence is still valid. Schematic representation of nanostructured metal colloid formation *via* the salt-reduction method is illustrated in Figure 5.1.

The first step in metal colloid formation is nucleation. During nucleation, the metal salt is reduced to give zerovalent metal atoms, which then can collide with metal ions or another metal atom in the solution to form irreversible seeds of stable metal nuclei. The diameter of the seed nuclei depends on the strength of the metal-metal bonds, the difference between the redox potentials of the metal salts and the reducing agent applied²². The next step is metal colloid particle formation. In general, particle formation proceeds *via* two steps: growth and agglomeration. Growth can be rationalized through collision of already formed nuclei with

²¹ To accomplish this, a large variety of stabilizers are used, like: donor ligands, polymers and surfactants.

²² For example, for silver it was shown experimentally that stronger reducing agents produce smaller nuclei in the seed [71] and references therein).

reduced metal atoms. Agglomeration is defined by the collision of already formed seeds. Although the processes during nucleation and particle growth are difficult to analyze separately, it is accepted that the size of the resulting metal colloids is determined by the relative rates of nucleation and particle growth. During the last decades, wet chemical reduction procedures were applied to synthesize metal colloids from practically all transition metals in combination with different types of stabilizers and the whole range of chemical reducing agents²³.

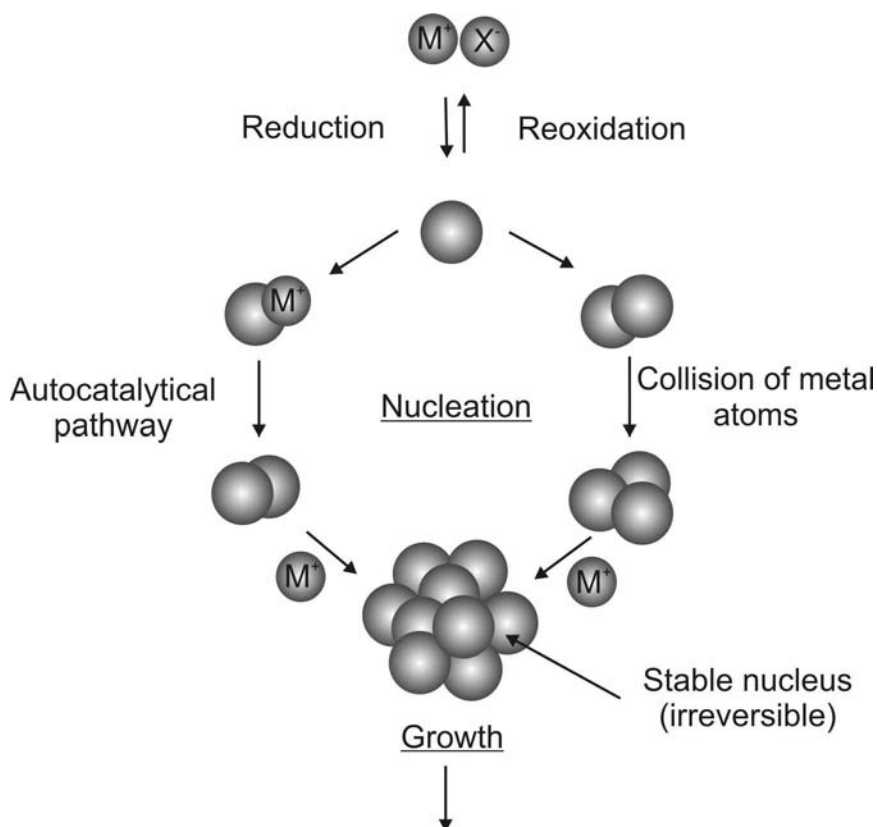


Figure 5.1 Formation of nanostructured metal colloids *via* the salt-reduction method (adopted from [71]).

Bimetallic colloids can be obtained by controlled co-reduction of two different metal ions. In general, the process can be presented as follows:



where Me1 is the first metal salt, Me2 is the second metal salt, Red is the reducing agent, Me1Me2(colloid) is the bimetallic colloid and Ox stands for a by-product formed after oxidation of the reducing agent.

²³ Hydrogen, carbon monoxide, formic acid, formaldehyde, hydrazine, BH_4^- etc are often mentioned in literature as reducing agents ([71] and reference therein).

As it was mentioned before, the colloidal synthesis method yields quite monodisperse metal colloid particles with a small average particle size ≤ 2 nm (if the particle size deviates by less than 15 % from the average value than a dispersion is referred as “monodisperse”). So, the most important aspect of the synthesis is **particle size control**. According to the literature, the essential factors controlling the particle size are the strength of the metal-metal bond, the molar ratio of metal salts, the colloidal stabilizer and the reducing agent, the extent of conversion, the temperature and the pressure applied [71].

To prevent agglomeration of the nanoparticles, protective agents are required. There are two basic **modes of stabilization**: *electrostatic* and *steric* stabilization.

The electrostatic stabilization (see Figure 5.2 a) is based on the Coulombian repulsion between the particles.

Steric stabilization (see Figure 5.2 b) is based on the steric coordination of organic molecules, which act as protective shields on the metallic surface. The nanometallic particles are separated from each other preventing coagulation. The main classes of protective groups according to the literature are polymers, solvents such as THF, long-chain alcohols, surfactants, organometallics etc. Lipophilic protective agents yield metal colloids that are soluble in organic media (“organosols”), while hydrophilic agents yield water-soluble colloids (“hydrosols”).

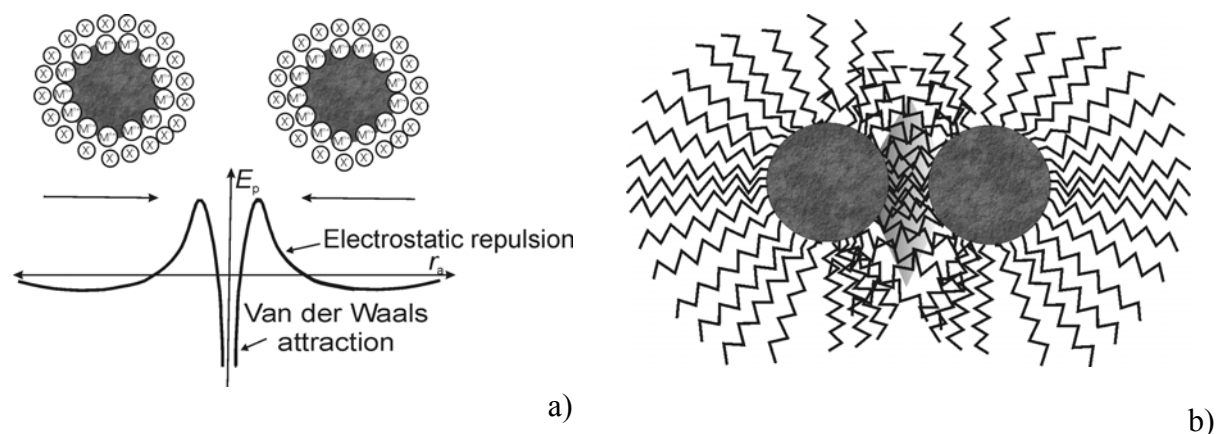


Figure 5.2 a) Electrostatic and b) Steric stabilization of metal colloids. Adopted from [71].

5.2. Experimental

5.2.1. Catalyst synthesis

As mentioned before, three variations of the salt reduction method were used. They are denoted as: EUP, KGE and WNF. All variations should give a nominal Pt:Ru composition of 1:1.

In general, the syntheses consist of these steps:

- a) *Weighing of salt precursors.* For the EUP and KGE variations the salt precursors were the same *i.e.* platinum (II) chloride (PtCl_2) and ruthenium (III) chloride (RuCl_3). Ruthenium (III) chloride is hydrophilic and therefore care should be taken that the weighing step and salt transfer into a reaction flask are fast. All syntheses were done under an Argon atmosphere (to prevent Ru oxidation by atmospheric oxygen as well as influence of water). Therefore, the reaction flask where reactants were transferred to was also under Argon atmosphere. For the WNF variation salt precursors were bis (cycloocta-1,5-diene) platinum(II) ($\text{Pt}(\text{COD})_2$) and tris (acetylacetonate) ruthenium(III) ($\text{Ru}(\text{acac})_3$).
- b) *Suspending of salt precursors in a solvent.* For all syntheses the solvent was tetrahydrofuran (THF). THF is kept under Argon atmosphere and is weighed before being suspended with the salt precursors, by means of a calibrated dropping funnel, which was always deaerated in advance. To achieve good mixing conditions, a magnetic bar is always added into the reaction flask. After the solvent is added, the dispersion is mixed to get a homogenous solution of reactants.
- c) *Addition of reducing agent.* In general, the reducing agent can be added gradually during several hours (done in the case of EUP and KGE syntheses) or at once (as done in WNF synthesis). The mode of addition depends on the metal colloid stabilization mode. The temperature of the reaction mixture depends on the strength of the reducing agent.
- d) *Solvent evaporation.* After the reaction is completed, *i.e.* metal colloids have been formed, the solvent is evaporated (usually by vacuum evaporation).
- e) *Depositing.* This step is omitted when the goal is to obtain an unsupported catalyst. The procedure is as follows: 1) as-synthesized metal colloids are dissolved in tetrahydrofuran (THF); 2) carbon support (Vulcan XC-72) is suspended in THF as well; and 3) suspension of carbon in THF is mixed with the metal colloid solution in THF and stirred. Carbon is added in the amount to get the catalyst with metal loading 30 %. Alternatively, depositing can be

done during step “b”, *i.e.* “salt precursor suspension in a solvent”, as it was done in the KGE variation.

f) *Solvent evaporation.* Same as for the step “d”.

g) *Leaching.* As-synthesised metal colloids are stabilized with a protective shell. As was mentioned before, a protective shell prevents particle from agglomeration, *i.e.* it enables a uniform particle size distribution and a small particle size, but on the other hand it decreases the active surface area, which can give a lower catalyst performance during fuel cell operation. Therefore, the protective shell should be leached out.

h) *Washing.* After leaching of the catalyst is washed in order to remove possible organic and inorganic impurities.

i) *Conditioning.* Conditioning is done as a final step before fuel cell operation is started in order to improve the catalyst performance. The effect of conditioning will be discussed in the text below where electrochemical performances of conditioned and unconditioned samples of the same KGE supported catalyst are compared. Here the procedure is described briefly. A schematic presentation of the conditioning apparatus is shown in Figure 5.3. The heart of this apparatus is the heating furnace. This furnace consists of a heating jacket of nearly one meter length and an inner quartz tube of the same length. The outer surface of the heating jacket is insulated to prevent heat transfer and heat loss from its surface. The temperature of the inner and the outer surface of the heating jacket are measured by means of a temperature controller, as shown in Figure 5.3. Between the outer surface of the quartz tube and the inner surface of the heating jacket lies a gas line, marked as a long wavy line in Figure 5.3. In this way, gas is heated before it enters the reaction tube (see Figure 5.3). The reaction tube is made of quartz and/or glass and lies in the middle of the heating furnace. Samples for conditioning are placed in sample porcelain boats of approximately 10 cm length inside the reaction tube. For conditioning, usually three different gases are used: Ar, O₂/Ar mixture and H₂²⁴. Usually the procedure is as follows: a) after the safety conditions are satisfied, *e.g.* it is ensured that there is no leaking of gases at the joints, and that temperature is at the desired level; b) samples are inserted in the reaction tube; c) argon flow is applied for 30 min; d) gas is changed to a O₂/Ar mixture for another 30 min, and then e) a H₂ stream is applied for another 30 min, and at the

²⁴ Argon serves to remove volatile compounds left after synthesis in the catalyst sample, the O₂/Ar mixture serves to oxidize organic impurities (O₂) and to remove them via the Argon flow. During this step the catalyst surface will oxidize, therefore in a final step reduction should be carried out. This is done by applying a H₂ flow. Since H₂ makes an explosive mixture with air, at the end the reaction tube is flashed with argon.

end d) gas is changed to argon for additional 5 min. After this procedure is completed, the reaction tube is taken off, cooled down to room temperature and samples are taken out.

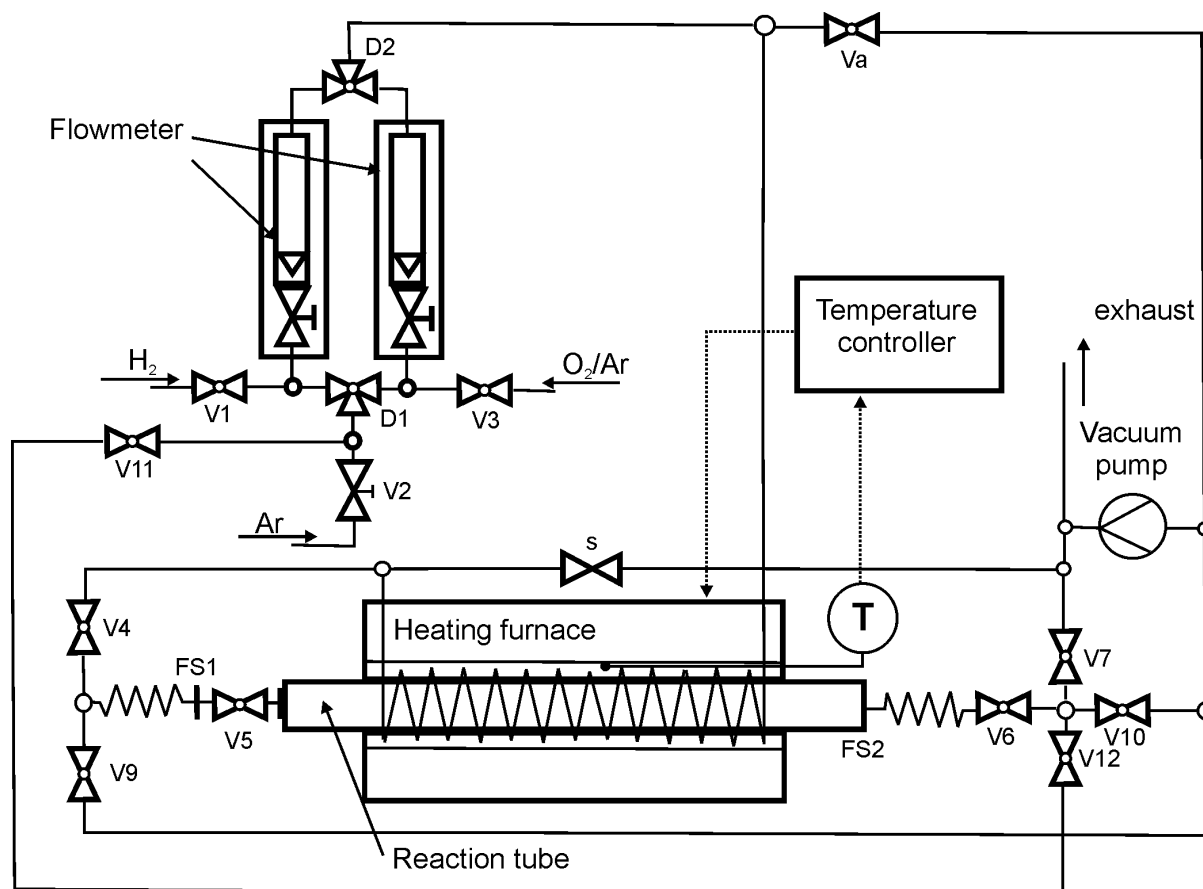


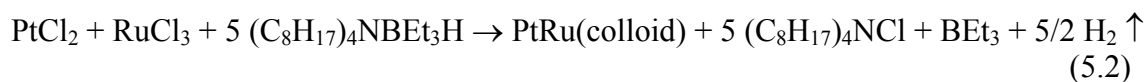
Figure 5.3 Schematic representation of the conditioning apparatus.

It should be mentioned that the conditioning procedure could vary depending on the type of catalyst.

Now, a closer insight to the synthetic methods applied is given.

EUP variation. In short, this variation is described as a preparation of a PtRu “organosol”. The metal salt precursors are: platinum (II) chloride (PtCl_2) and ruthenium (III) chloride (RuCl_3). The solvent used is THF. The reducing agent is $(\text{C}_8\text{H}_{17})_4\text{NBEt}_3\text{H}$, where BEt_3H^- is the reductant and $(\text{C}_8\text{H}_{17})_4\text{N}^+$ is the stabilizing agent. The applied method is a variation of the salt reduction method, which originally uses BH_4^- as a reducing agent. The disadvantage of using BH_4^- as a reducing agent was the formation of transition metal borides along with nanometallic particles [71]. Here, triethylboron is recovered unchanged from the reaction and borides do not contaminate the product. As mentioned before, the stabilizing agent is $(\text{C}_8\text{H}_{17})_4\text{N}^+$. The mode of stabilisation is steric stabilisation. After the reduced metal nucleus is formed, the metal core is protected by a monolayer shell of surfactant molecules.

PtRu metal colloids prepared by this method are described as “organosol”, since a lipophilic protective agent yields a metal colloid being soluble in organic media. The synthesis can be represented as follows:



The temperature at which the synthesis was performed was 40°C.

As-synthesized $(\text{C}_8\text{H}_{17})_4\text{N}^+$ protected metal colloids contain around 10 *mass* % of metal.²⁵ Purified metal colloids can be obtained only as supported metal nanoparticles, because once the protective shell is removed, particles can easily undergo agglomeration. Leaching is done by washing as-synthesized metal colloids with ethanol. During this step, protective groups are removed due to solubility of the $(\text{C}_8\text{H}_{17})_4\text{N}^+$ in ethanol. Since particles are supported on carbon, agglomeration is prevented.

After leaching, almost pure metal particles supported on carbon are obtained (see energy dispersive X-ray analysis below (Figure 5.4)).

KGE variation. The method is new and up to now not fully standardized. Metal salt precursors are platinum(II) chloride (PtCl_2) and ruthenium(III) chloride (RuCl_3), so the same as in the EUP variation. The reducing agent is LiBt_3H and Bt_3H is the reductant as in the EUP variation. The solvent used is THF. The reducing agent is added in excess, so that a part of it stabilizes the formed metal colloids. The mode of stabilisation is still unclear, but preferably can be explained by static stabilisation, *i.e.* an excess of reducing agent forms an electrochemical double layer around neutral metal nuclei. Zerovalent metal nuclei stabilized only with THF (solvent) were reported in the literature.²⁶ So a steric stabilisation effect by the THF molecules can be expected, too. In general, the synthesis can be represented as follows:



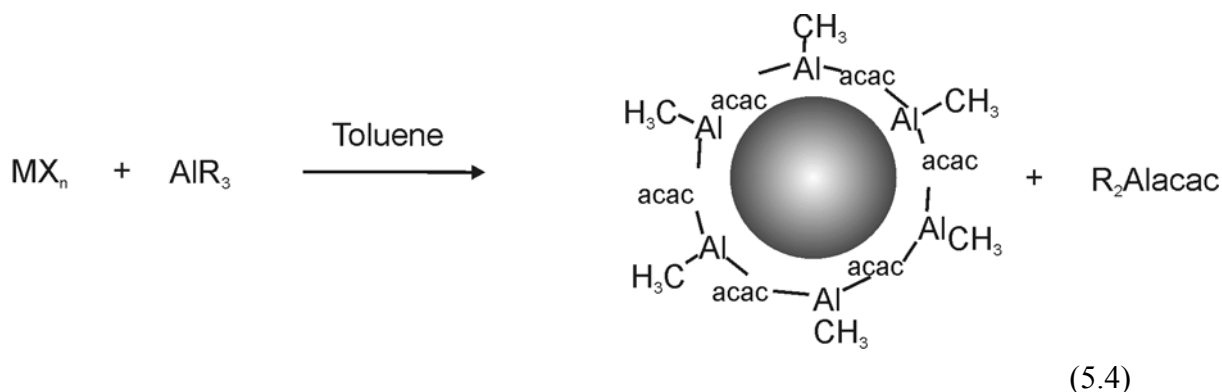
The synthesis was performed at room temperature. In this case, the reducing agent is stronger than in case of the EUP variation, thus milder conditions can be applied.

²⁵ Typically in literature metal colloids obtained by this method are reported to contain between 6 - 12 *mass* % of metal [71]. In our case sample was sent on elemental analysis and 10.5 *mass* % was obtained.

²⁶ It was shown for Ti in a similar synthesis as performed here (except that reducing agent is taken in stehiometric condition) that the resulting product Ti 0.5THF consists of Ti_{13} clusters in the zerovalent state, stabilized by six intact THF molecules [71].

Both supported and unsupported metal colloids can be prepared by this method. When the method is used to obtain supported metal colloids, the carbon support (Vulcan XC-72) is added to the mixture of salt precursors and the solvent (during step “b”) before the reduction step carbon is dispersed first in THF and after homogenous dispersion is obtained, it is added into the solution of the salt precursors in THF. After the synthesis is completed, the solvent is vacuum evaporated and the obtained catalyst is subjected to several washing steps: First ethanol, then benzene, and finally a water/benzene mixture (Water serves to wash out B-compounds eventually present in the catalyst powder, while benzene removes all possible organic compounds). Finally the solvent is freeze-dried and removed by means of vacuum sublimation and PtRu supported on carbon or unsupported is obtained.

WNF variation. Briefly, the method is described as an organoaluminium method. The metal salt precursors are: bis(cycloocta-1,5-diene)platinum(II) ($\text{Pt}(\text{COD})_2$) and tris(acetylacetonate)ruthenium(III) ($\text{Ru}(\text{acac})_3$). The reducing agent is tris(methyl)aluminium (III) ($\text{Al}(\text{me})_3$). The solvent used is THF. The method is a slight modification of mono and bi-metallic nanoparticle synthesis by using organoaluminium compounds as reducing agents, as described in [71]. In general, for monometallic nanoparticles the method can be formulated as follows:



where MX_n is a metal halogen or metal acetylacetonate salt ($n=2-4$), and R is an alkyl group ($\text{C}_1 - \text{C}_8$).

A layer of condensed organoaluminium species protects the metal core against aggregation as shown in equation (5.4). The exact “backbone” of the colloidal organoaluminium protecting agent has still not been completely established [71]. Unreacted organoaluminium groups (for example $\text{Al} - \text{CH}_3$) from the starting material are shown to be still present in the metal nanoparticles stabilizer. Active $\text{Al} - \text{C}$ bonds are used for a controlled protonolysis by long-chain alcohols or organic acids (these are “modifiers”) to

give Al-alkoxide groups in the stabilizer. This modification of the organoaluminium protecting shell can be used to tailor the dispersion characteristics of the original organosols. In this way, the solubility of the colloidal metal nanoparticles both in hydrophobic and hydrophilic media can be achieved. As-synthesized catalyst is subjected to leaching²⁷. For the leaching step 5 M NaOH was used, since it can form soluble sodium aluminate (NaAlO_2). The leaching temperature was 70 °C. After leaching, the catalyst was conditioned (as explained above).

A summary of catalyst names and abbreviations is given in Table A II.1 in Appendix II.

Prepared catalysts were characterized by EDX, XRD, TEM and SEM (scanning electron microscopy) and by electrochemical methods *i.e.* CO stripping and cyclic voltammetry.

5.2.2. Physical methods

The atomic ratio of Pt to Ru was determined by EDX. SEM with colour element mapping was used to check the presence of each element in a sample and its distribution over the support (SEM data are available only for the EUP sample). EDX and SEM analyses were performed with the same instrument (Oxford Inca System).

XRD was used to determine mean particle sizes and lattice parameters. X-ray diffraction data of the catalyst were collected on a Stoe STADI P transmission diffractometer in Debye-Scherrer geometry with a primary monochromator (curved germanium (111)) and a linear position sensitive detector. $\text{Cu } \alpha_1$ radiation was used and a 2θ scan from 10° to 100° with a step width of 0.01°. For measurements of air sensitive samples, the samples were filled into glass capillaries in a glove box and sealed to prevent contact with air. The measured patterns were evaluated qualitatively by comparison with entries from the PDF-2 powder pattern database. The analysis is performed with the WinXPow software package.

The mean particle size and particle size distribution was obtained by TEM measurements. HITACHI H7500 microscope (magnification up to 1.25 million) was used. For TEM analysis samples were prepared by ultrasonically suspending the catalyst powder in THF. A drop of the suspension was applied onto a clean carbon covered nickel grid.

²⁷ Electrochemical performances of non-leached sample were also checked (see below).

5.2.3. Electrochemical methods

Electrochemical measurements (CO stripping voltammetry, cyclic voltammetry in absence of methanol, steady state measurements, chronoamperometric measurements and electrochemical impedance spectroscopy) were done as explained in the experimental text section (Chapter 2). The loading of all MEA assemblies was 1 mg cm^{-2} .

5.3. Characterisation of catalysts

5.3.1. Physical methods

The result of the EDX analysis for the EUP catalyst is shown in Figure 5.4. Only peaks from the support (Vulcan XC-72), from platinum and from ruthenium are present. EDX has shown that the prepared catalyst consists of 68 *mass* % carbon (Vulcan XC-72), 10 *mass* % Ru and 22 *mass* % Pt (catalyst is prepared as 30 *mass* % metal loading on carbon). EDX analyses for other catalysts were done, but plots are not shown here. In general, it was shown that all prepared catalysts have a Pt:Ru atomic ratio of approximately 1:1. Results are collected in Table 5.1. The Pt content is calculated without taking into account the carbon support (for supported samples). This means that for both supported and unsupported catalysts the total sum of Pt and Ru contents is 100 %. In case of the $\text{KGE}_{\text{unSUPP}}$ catalyst besides Pt and Ru the EDX analysis indicates the presence of chlorine in an extent of approximately 6 *mass* %. Chlorine probably remained since it was not fully removed in the washing steps. By EDX analysis, only the overall composition of the catalyst can be determined, but not the catalyst surface composition.

The X-ray diffraction patterns for the investigated catalysts are shown in Figures 5.5, 5.6 and 5.7. The first peak at $2\theta \approx 23^\circ$ originates from the Vulcan XC-72 carbon support, while the other peaks are reflections of the face centred cubic (f.c.c) crystal lattice of Pt (vertical lines on the diagram represent the positions of the peaks of pure Pt). In the case of the $\text{KGE}_{\text{unSUPP}}$ sample (Figure 5.6) the peak at $2\theta \approx 23^\circ$ is missing. For EUP and KGE catalysts all peaks appear approximately at the same 2θ values as peaks for pure platinum (for example, the f.c.c (220) diffraction peak of the EUP sample is at $2\theta \approx 67.8^\circ$ while of Pt f.c.c (220) at $2\theta \approx 67.5^\circ$; similar is for KGE catalysts where f.c.c (220) peak reflections for $\text{KGE}_{\text{unCON}}$, KGE_{CON} and $\text{KGE}_{\text{unSUPP}}$ catalysts are respectively at 2θ values of 67.5, 67.6 and 67.7). In case of the $\text{WNF}_{\text{leach}}$ catalyst, all peaks are shifted towards higher angles compared to pure Pt (for example the f.c.c (111) diffraction peak of the WNF sample appears at $2\theta \approx$

40.4° between diffraction peaks for Pt f.c.c (111) at $2\theta \approx 39.8^\circ$ and diffraction peak for Ru h.c.p (101) at $2\theta \approx 42.2^\circ$; the f.c.c (220) diffraction peak of the sample appears at $2\theta \approx 68.8^\circ$ between diffraction peaks for Pt f.c.c (220) at $2\theta \approx 67.5^\circ$ and the diffraction peak for Ru h.c.p (110) at $2\theta \approx 69.4^\circ$). Higher angles, *i.e.* lower lattice parameter a , can indicate formation of a solid solution of PtRu with the Pt lattice being contracted due to the replacement of some Pt atoms in the Pt f.c.c crystal structure by the smaller Ru atoms ($r_{\text{Ru}}=0.133$ nm and $r_{\text{Pt}}=0.138$ nm [72]). Another possibility for the observed shift in 2θ values relative to 2θ values of the pure phase can be due to the lattice strain, X-ray scattering or disorder as pointed out in [48].

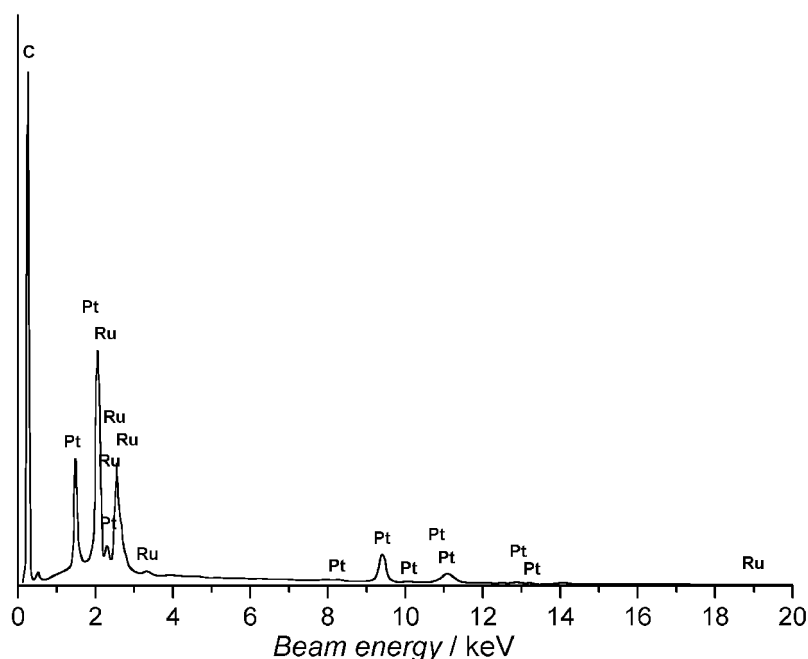


Figure 5.4 EDX analysis of the EUP sample.

Lattice parameters for PtRu catalysts were evaluated from the angular position of the (220)²⁸ reflection peak maxima, by using equation (5.5):

$$a = \frac{\sqrt{2} \cdot \lambda_{K\alpha_1}}{\sin \theta_{\max}} \quad (5.5)$$

where a is the lattice parameter, $\lambda_{K\alpha_1}$ is the wavelength of X-rays used (0.154056 nm) and θ_{\max} is the Bragg angle at the peak maximum. The results are given in Table 5.1.

²⁸ The angular position of the f.c.c (220) peak reflection is in a region where the diffraction spectrum of the carbon support contributes only in terms of a linear background. In the vicinity of other peaks, for example the f.c.c (111) diffraction peak of PtRu alloy, the strong background from the two-dimensional reflection of the carbon layers in the carbon black can be observed [73].

They refer to the lattice parameter values of the crystalline fraction of the catalysts. The values are compared to literature lattice parameter values of bulk PtRu alloys of different Pt:Ru compositions [74] (see Table 5.2). Lattice parameter values for the EUP and KGE catalysts are between the lattice parameter of pure Pt and the lattice parameter of the PtRu alloy with 90.3 at % Pt. This indicates a low extent of alloying. In case of the WNF_{leach} catalyst, the lattice parameter value corresponds to a Pt content of approximately 48.3 at % Pt²⁹.

Table 5.1 Pt content (EDX, XRD), mean particle sizes (XRD and TEM) and lattice parameters (XRD) for prepared PtRu catalysts.

Catalyst	Pt (at %)		d / nm		a / nm
	EDX	XRD	XRD	TEM	XRD
EUP	52.8	90.3	3.60	2.2-2.7	0.391
KGE _{uncon}	50.3	<100	4.0	2.7	0.392
KGE _{con}	50.3	90.3	3.9	2.7 ³⁰	0.391
KGE _{unsupp}	48.9	90.3	4.45	3	0.391
WNF _{unleach}	/	/	amorphous	0.8 – 1.2	/
WNF _{leach}	54	≈48.3	2.9	1.7-3.3	0.3859

Table 5.2 Pt content in at% in PtRu bulk alloys with different Pt:Ru compositions based on X-ray fluorescence measurements, crystal structure and lattice parameters measured by X-ray diffraction. Adopted from reference [74].

Pt at %	Crystal structure	a / nm
100	f.c.c	0.39231
90.3	f.c.c	0.39166
70.2	f.c.c	0.38907
48.3	f.c.c	0.38624
39.4	f.c.c	0.38486
9.5	h.c.p	0.27178
0.0	h.c.p	0.27058

²⁹ Lattice parameter values for all catalysts are lower than for the bulk PtRu alloy (Table 5.1). The contraction of lattice constants in metal nanoparticles relative to values expected for bulk samples were already reported in [75]. This effect was interpreted as a result of the increase in the surface stress due to the high curvature of the particles.

³⁰ Conditioning under mild conditions *i.e.* at low temperatures like in our case at 120°C, does not produce any particle agglomeration. Here TEM after conditioning was not performed and it was assumed that particle size remains unchanged compared to the unconditioned sample.

For all samples, peak reflections of the h.c.p. crystal structure of Ru were not seen. The absence of characteristic Ru peak reflections can be due to several reasons. One is that Ru particles are small and not in a crystalline state, *i.e.* amorphous. Dubau *et al.* [76] attributed similar finding to Pt particles decorated by Ru particles. Another reason is that Ru is present as Ru-oxide, as it was reported by Rolison *et al.* [48] and Jusys *et al.* [17] who investigated several commercial Pt-Ru catalysts and found out that they are predominantly a mixture of a Pt metal phase and Ru-oxides. In our study, peak reflections of anhydrous or hydrous Ru oxide were not seen as well. In general, hydrous Ru-oxide peak reflections have a low intensity and peaks are broad, so the presence of Ru-oxide cannot be excluded. The same is true for metallic Ru.

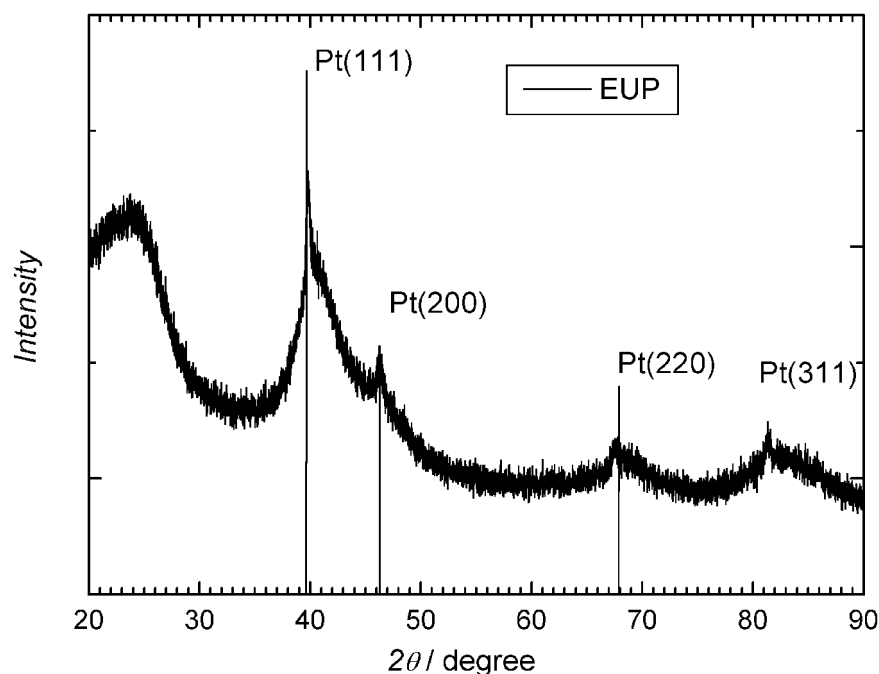


Figure 5.5 X-ray diffraction pattern of the 30 % PtRu / Vulcan-XC-72 EUP catalyst with an atomic ratio of Pt:Ru=1:1.

The average particle size is estimated by using the Scherrer equation [73]:

$$d = \frac{0.9 \cdot \lambda_{K\alpha_1}}{B_{(2\theta)} \cos \theta_{\max}} \quad (5.6)$$

where d is the mean particle size and $B_{(2\theta)}$ the width (in rad) of the peak at the half height (peak height is calculated from a baseline). The other symbols have the same meaning as in equation (5.4). The values are given in Table 5.1. Since particle sizes are determined from the

f.c.c (220) peak reflection, they should correspond to the particle size of the crystalline part of the catalysts.

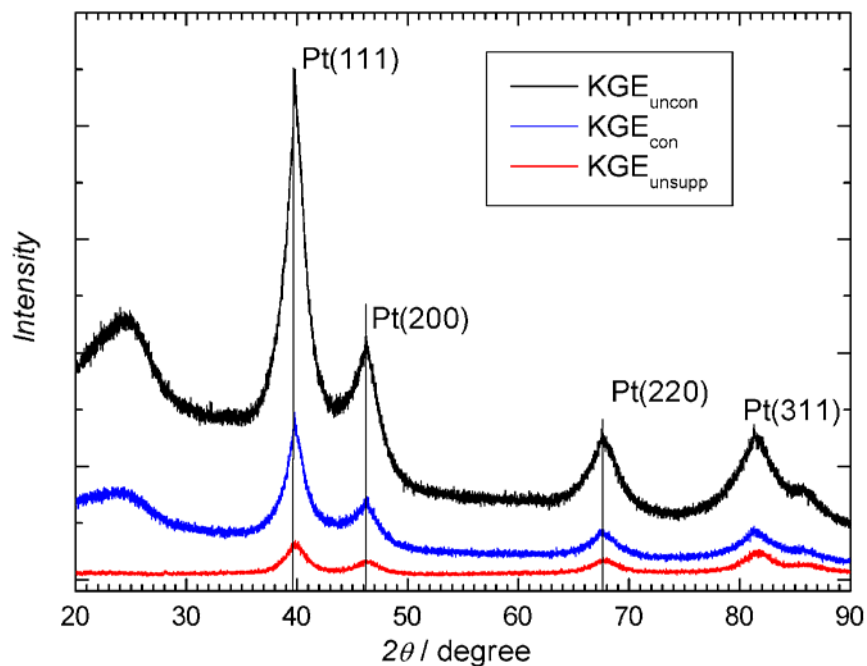


Figure 5.6 X-ray diffraction patterns of 30 % PtRu / Vulcan-XC-72 KGE_{uncon} and KGE_{con} and KGE_{unsupp} catalysts with an atomic ratio of Pt:Ru=1:1.

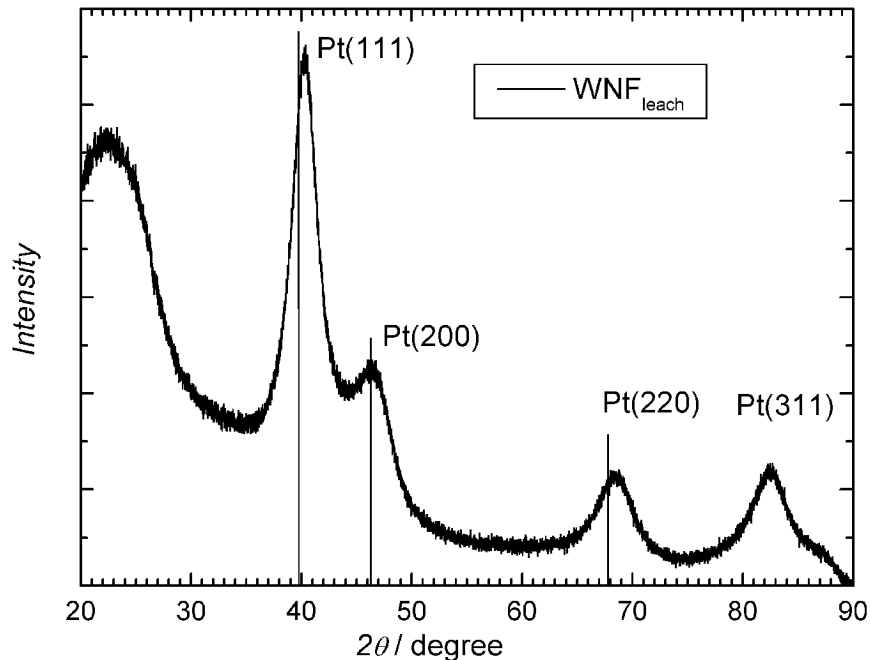


Figure 5.7 X-ray diffraction pattern of 30 % PtRu / Vulcan-XC-72 WNF_{leach} catalyst with an atomic ratio of Pt:Ru 1:1.

Bright field TEM micrographs of the investigated catalysts are shown in Figure 5.8.

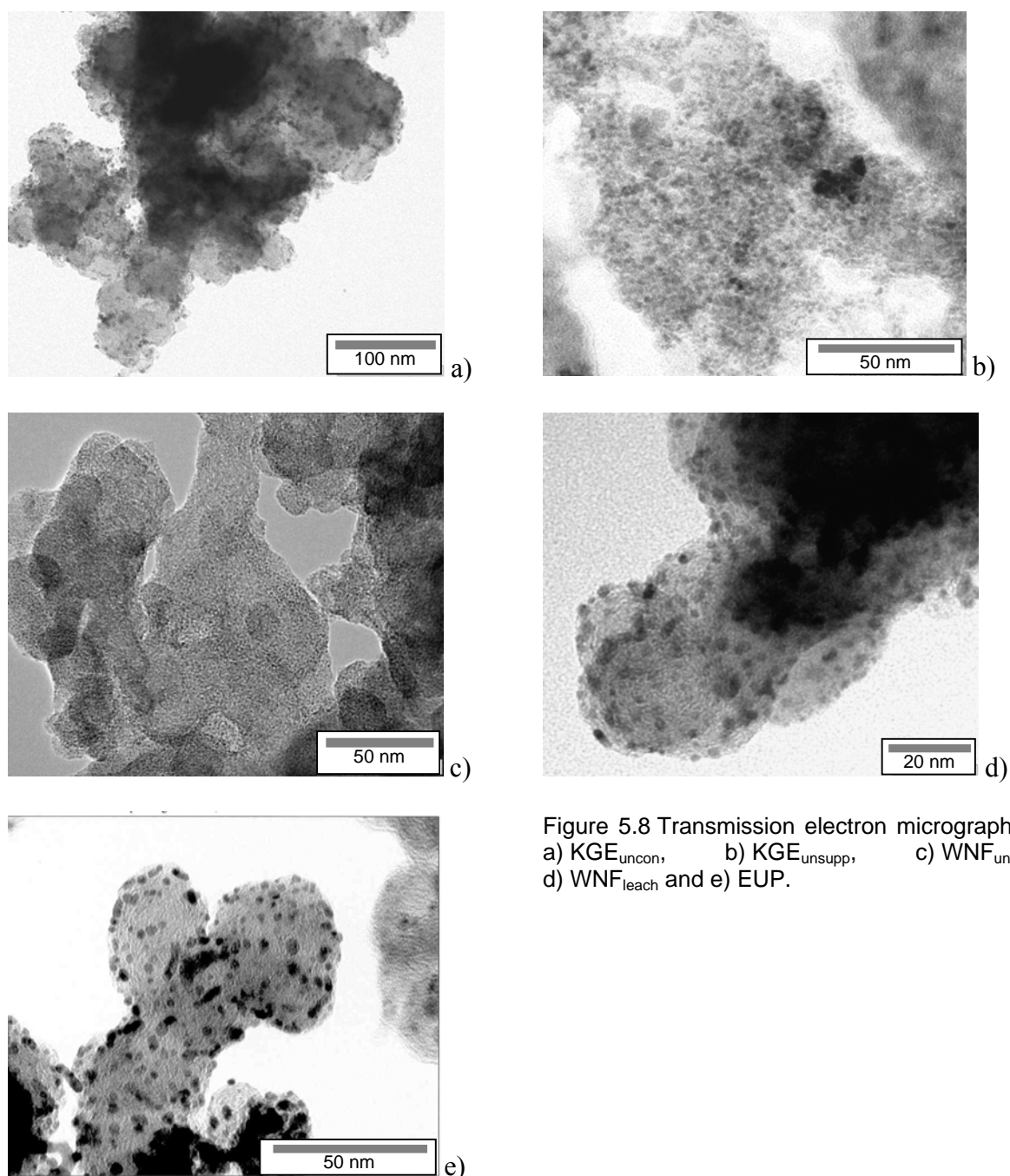


Figure 5.8 Transmission electron micrographs of a) $\text{KGE}_{\text{uncon}}$, b) $\text{KGE}_{\text{unsup}}$, c) $\text{WNF}_{\text{unleach}}$, d) $\text{WNF}_{\text{leach}}$ and e) EUP.

No significant particle agglomeration was observed. Particles are uniformly distributed over the Vulcan XC-72 support. Particle size varies and depends on the preparation route used. The smallest particle size is obtained by the WNF method. The unleached sample ($\text{WNF}_{\text{unleach}}$) has a particle size of 0.8 – 1.2 nm, very uniform particle size distribution as well as particles distribution over the support. After leaching particle agglomeration occurs and the particle size for sample $\text{WNF}_{\text{leach}}$ is from 1.7 – 3.3 nm. In case of the KGE samples the particle size of the unsupported sample is greater than of the supported sample. This indicates a small influence of particle agglomeration.

A SEM micrograph of the EUP catalyst with element colour mapping is shown in Figure 5.9. Carbon is coloured in red, platinum in green and ruthenium in blue. The element mapping is used in order to check the presence of each metal and therefore its distribution in the sample selected for observation. A uniform distribution of both metals (Pt and Ru) on carbon can be taken as an indication of an alloyed or an intermetallic system. Black spots come from an uneven particle distribution.

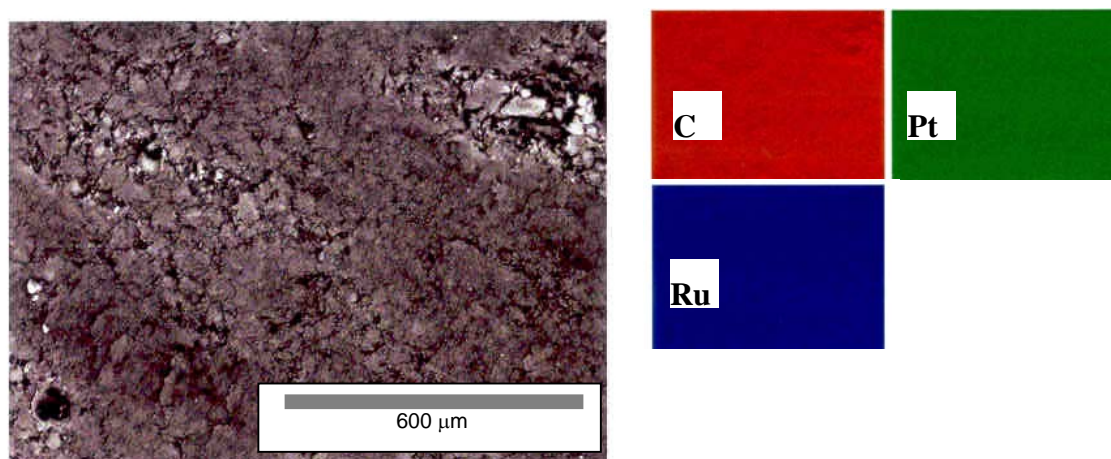


Figure 5.9 SEM micrograph of the EUP sample with element colour mapping.

The results of the methods discussed above are summarized in Table 5.1 (EDX and XRD PtRu compositions, the mean particle size determined by XRD and TEM and the lattice parameter obtained by XRD). The PtRu composition from XRD is obtained by comparing the lattice constants of the catalysts with lattice constants of well-defined PtRu bulk alloys as given in Table 5.2. As can be seen in Table 5.1 all catalysts have overall PtRu compositions as expected (approximately 50:50 *at %* Pt:Ru) (first column in Table 5.1 is EDX composition). The second column (XRD composition) shows compositions of the crystalline parts of the catalysts. It follows that the WNF_{leach} catalyst is a PtRu alloy with a PtRu composition of approximately 1:1. Other catalysts are PtRu alloys rich in platinum (approximately 90 *at %* of platinum, except for the KGE_{uncon} catalyst which behaves almost like pure platinum). It can be assumed that the WNF_{leach} catalyst consists predominately of a PtRu alloy phase, while other catalysts are mixtures of a Pt rich phase, a Ru-rich and probably a Ru-oxide phase. As was already mentioned, Ru or Ru-oxide peaks are not seen in XRD spectra, which can be explained by low crystalline of Ru and Ru-oxides. The particle size determined by XRD is bigger than by TEM. XRD counts only for crystalline particles while TEM can “see” smaller (non-crystalline) particles. It can be expected that an average particle size determined by XRD is bigger than determined by TEM for the same sample.

However, TEM should cover the whole range of particle sizes, including average particle size determined by XRD, as it is in the case of one of the investigated catalysts - $\text{WNF}_{\text{leach}}$ (for this catalyst XRD particle size was 2.9 nm which is in the range of particle sizes determined by TEM (1.7 – 3.3 nm)). For other two catalysts (EUP and KGE_{con}) XRD particle sizes were out of the range of TEM particle sizes, which can indicate that this fraction of particles was insignificant or not seen in TEM analysis.

The above discussed methods deal with *ex-situ* catalyst characterisation. *In-situ* characterisation was performed by CO-stripping voltammetry and cyclic voltammetry in absence of methanol³¹ and will be discussed in the following text.

5.3.2. CO stripping

Carbon monoxide is considered to be a kind of “test molecule” in electrocatalysis. CO stripping voltammetry has a threefold function. First, CO stripping charge can be used for estimation of real surface area (This use of CO stripping voltammetry was discussed in Chapter 3). Second, commencement, peak potential and shape of CO stripping wave are surface sensitive [16]. Third, since CO is considered as an intermediate in methanol oxidation (see Chapter 4), higher activity in CO oxidation can be correlated to higher activity towards methanol oxidation.

Figure 5.10 summarizes results for the CO stripping voltammetry of a saturated CO monolayer on different PtRu supported catalysts. Only anodic parts of voltammograms are presented. All CO stripping voltammograms are distorted and baselines (second positive going sweep) are not well defined. Problems with voltammetric CO charge determination were already discussed in Chapter 3, where the method for baseline subtraction was proposed. The method is applied here and corrected CO stripping voltammograms are shown in Figure 5.11 and will be discussed in the following.

Real surface areas³² were calculated from CO stripping charge following the procedure as described in Chapter 3. The determination of CO stripping charges and surface areas are given in Table 5.3 below.

³¹ In electrochemistry, cyclic voltammetry of bulk polycrystalline and especially single crystal surfaces is considered as a fingerprint of an electrode surface [7].

³² In the following text the real surface area is denoted as CO surface area.

For comparison with the CO surface area, a rough estimate of the total surface area is made by assuming spherical particles with a diameter determined from XRD and by using equation (5.7):

$$S_{XRD} = \frac{6 \cdot 10^3}{\rho_{PtRu} d} \quad (5.7)$$

where S_{XRD} is the specific surface area in $\text{m}^2 \text{g}^{-1}$, ρ_{PtRu} is PtRu density in g cm^{-3} and d is particle diameter in nm.

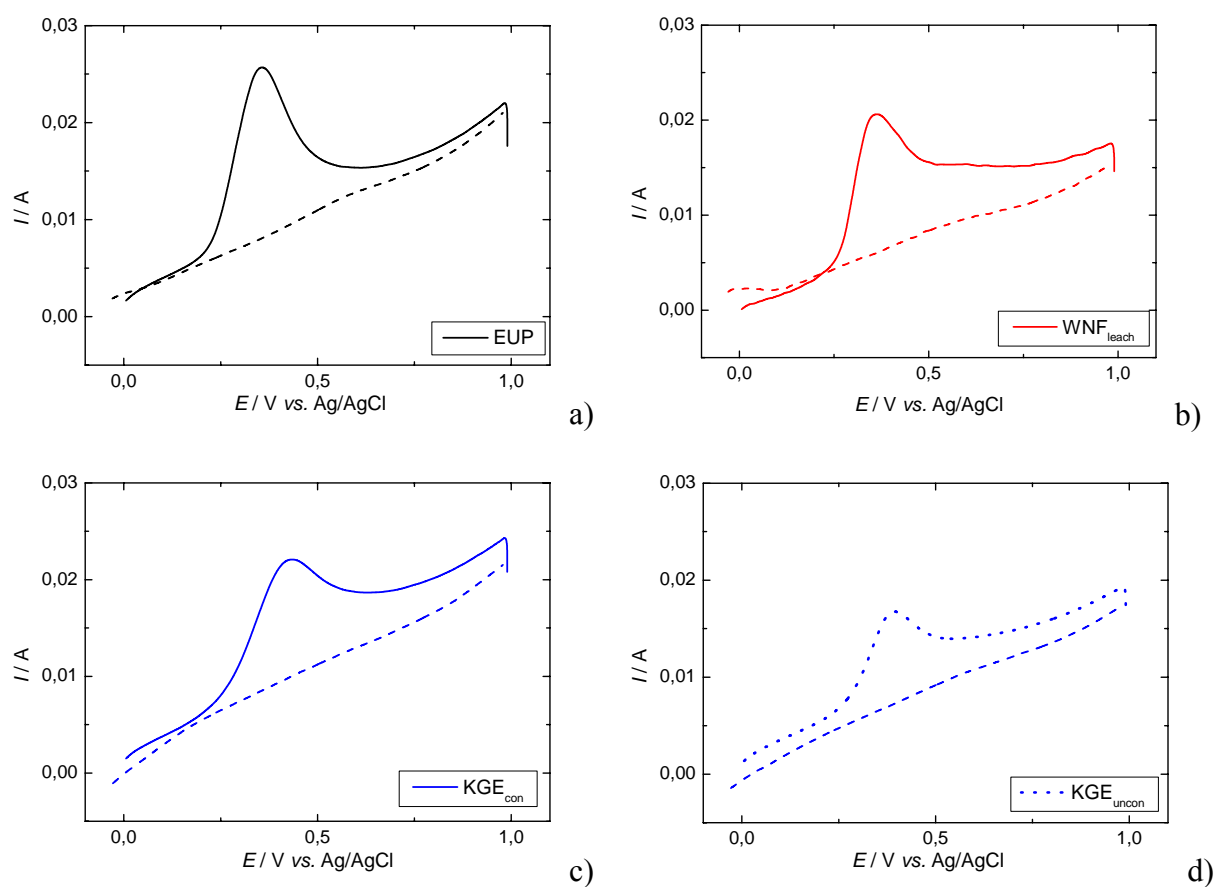


Figure 5.10 CO stripping voltammograms of carbon supported PtRu catalysts. Dashed line - second positive going sweep. Conditions: sweep rate 5 mV s^{-1} , CO adsorption potential 0 V vs. Ag/AgCl , adsorption time 30 min , N_2 in working electrode compartment, flow rate 120 ml min^{-1} ; room temperature.

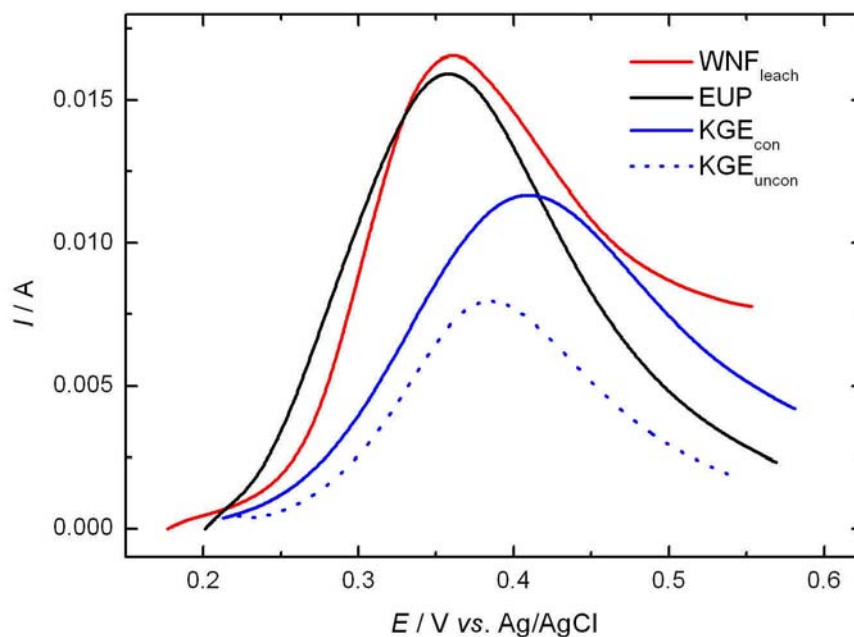


Figure 5.11 CO stripping voltammograms of carbon supported PtRu catalysts from Figure 5.10 after baseline correction.

The PtRu mass density was calculated as follows:

$$\rho_{\text{PtRu}} = \rho_{\text{Pt}} \cdot \text{mass}_{\text{Pt}} + \rho_{\text{Ru}} \cdot \text{mass}_{\text{Ru}} \quad (5.8)$$

where ρ_{PtRu} is the density of PtRu alloy particles, ρ_{Pt} is the platinum density (21.4 g cm^{-3}), ρ_{Ru} is the ruthenium density (12.2 g cm^{-3}), mass_{Pt} and mass_{Ru} are the Pt and Ru mass fractions determined from EDX analyses without taking the oxygen content into account. The results of this calculation are summarized in the Table 5.4.

Table 5.3 CO stripping charge and real surface area for supported PtRu catalysts. Conditions: CO adsorption at 0 V vs. Ag/AgCl for 30 min or 60 min. N_2 in working electrode compartment, flow rate 120 ml min^{-1} , room temperature.

Catalyst	Q_{CO} / C	$S / 10^3 \text{ cm}^2$
EUP	0.51 ± 0.05	1.8 ± 0.2
$\text{KGE}_{\text{uncon}}$	0.31 ± 0.025	1.1 ± 0.1
KGE_{con}	0.52 ± 0.05	1.8 ± 0.2
$\text{WNF}_{\text{leached}}$	0.58 ± 0.01	2.03 ± 0.03

In the case of the $\text{WNF}_{\text{leach}}$, EUP and KGE_{con} samples, the real surface area³³ is more than one half of the XRD surface area (56%, 61% and 66 % respectively). Utilisation rate for the $\text{KGE}_{\text{uncon}}$ catalyst is a bit lower (41 %). According to the literature, the catalyst utilisation under fuel cell conditions can vary from 5 % [19] to 80 % [20] related to BET surface area. A typical value for catalyst utilisation is about 50% compared to XRD [63], TEM [65] or BET [19] surface areas. CO surface area of $40 \text{ m}^2 \text{ g}^{-1}$ for carbon supported PtRu catalysts prepared by the nitrile method (cell configuration was rotating disc and thin film method was used) was obtained in reference [63]. At the same time the XRD surface area was $80 \text{ m}^2 \text{ g}^{-1}$. The result was taken as an indication of the validity of PtRu surface area characterisation by CO stripping voltammetry. A similar result was obtained in a half-cell study on a gas diffusion electrode prepared with PtRu carbon supported catalyst obtained by chemical reduction, [65] where the CO stripping area was approximately 50 % of TEM surface area.

Table 5.4 Atomic and *mass* % contents, densities, XRD and specific surface areas of PtRu catalysts.

Catalyst	<i>at</i> % Pt	<i>mass</i> % Pt	$\rho_{\text{PtRu}} / \text{g cm}^{-3}$	$S_{\text{XRD}} / \text{m}^2 \text{ g}^{-1}$	$S_{\text{sp}} / \text{m}^2 \text{ g}^{-1}$
EUP	52.8	68.3	18.5	90	55.0±5.3
$\text{KGE}_{\text{uncon}}$	50.3	66.1	18.3	82	33.9±2.7
KGE_{con}	50.3	66.1	18.3	84	55.8 ±5.3
$\text{WNF}_{\text{leach}}$	54	69.4	18.6	111	62.7±1.1

Catalyst utilisation is influenced by MEA manufacturing, content of metallic oxide phase, temperature and catalyst preconditioning [19], and by the procedure which is used to get the CO surface area from experimental data, as discussed in Chapter 3. Since particles are carbon supported, and part of the particle surface is covered with the Nafion film some imperfections in particle contact can be expected (as it was discussed for PtRu unsupported catalysts), utilisation will further decrease. High metal oxide content can significantly decrease the CO surface area as shown in reference [19]. If CO stripping is performed at higher temperatures and on a reduced sample the CO surface area increases [19,20]. In our case, CO stripping was performed on an as-received sample at room temperature. No additional MEA conditioning was applied (for example MEA conditioning in H_2 atmosphere). The slightly lower catalyst utilisation in case of the $\text{KGE}_{\text{uncon}}$ sample can be due

³³ The CO adsorption method was used for real surface area determination.

to the higher Ru-oxide content in this sample compared to the conditioned sample.³⁴ In the case of the WNF catalyst, its utilisation can be also influenced by the lower accessibility of particles deposited in small pores of the carbon support. Originally, the WNF method produces small particles with a particle size in the range from 0.8 to 1.2 nm. As-produced catalyst is supported on Vulcan XC-72, and it is possible that some of particles are impregnated in pores with small diameters, which are later on inaccessible. According to pore size distribution measurements on Vulcan XC-72, pores in the range from 30-50 nm dominate the surface area of this carbon black, but there is a small fraction of pores with a pore size of about 3 nm [64]. In conclusion, taking into account all factors, which contribute to catalyst utilisation under fuel cell conditions, CO surface areas determined in this study indicate typical values of catalyst utilisation found in literature.

The onset of reaction and peak potential values differs for different electrocatalysts. In general, the shape of the CO stripping wave for all catalysts reflects the same features. The commencement of CO oxidation in case of the EUP catalyst is at lowest potential. The peak height decreases according to the ranking: $WNF_{leach} > EUP > KGE_{con} > KGE_{uncon}$. The peak width at half of the peak current is largest for KGE_{con} catalyst, while for other catalysts this value is approximately the same.

CO stripping peak potential is sensitive to the PtRu surface composition [16]. The lowest value was obtained for a Ru surface composition of 46 *at %*. A similar result was obtained by Cao *et al.* [47] for CO oxidation on Pt black decorated by Ru. In their study, a minimum was obtained when the Ru surface composition was between 38 and 57 *at %*. In addition, concerning the CO stripping peak potential, Dubau *et al.* [77] found that for the same overall PtRu composition the alloyed PtRu catalyst has more positive peak potential than a non-alloyed Pt+Ru catalyst obtained by physical mixing of Pt and Ru colloidal catalysts. To summarize, two main tendencies were recognized: First, the maximum towards CO oxidation (peak potential at most negative potential) appears at a surface with a Ru-content of approximately 50 *at %* and second, the alloyed catalyst is less active than the non-alloyed catalyst.

Due to the sensitivity of the CO stripping peak potential with respect to the Ru surface content and the level of catalyst alloying, CO stripping voltammetry could be used in principle for *in situ* catalyst characterisation. A problem, which arises here, is a suitable

³⁴ CO adsorption takes place only on pure metallic surfaces [17].

standard for method calibration. In a study by Dihn *et al.* [19] CO stripping voltammetry was used for *in situ* characterisation of unsupported PtRu catalysts and as a standard CO stripping data reported for PtRu bulk alloys were used [16]. However, we do not consider this approach as fully justified due to the following reasons: a) smooth surfaces do not behave like rough surfaces made of nanoparticles; b) the mechanism of CO oxidation [26] includes OH species adsorbed at the surface; if the rate determining step is the reaction between adsorbed CO and OH, the CO stripping peak potential can be *pH*-dependent and influenced by the H⁺-concentration in the supporting electrolyte; c) the conditions in a classical three-compartment electrochemical cell can differ a lot from the conditions in a more technical configurations; d) real catalysts are usually a mixture of alloyed phases and of metal oxides. Therefore CO stripping can be used for *in situ* catalyst characterisation after suitable calibration. Calibration can be also done by XRD or XPS. In our case, according to XRD analysis the WNF_{leach} sample is a PtRu alloy with approximately 50 at % Pt, while other catalysts are a mixture of Pt rich phases and metal oxides. So the overlapping of the CO peak potentials of these two catalysts is probably due to the mutual influence of the two different effects (alloy composition and level of alloying). Concerning their total activities the WNF_{leach} and EUP catalysts are comparable. KGE catalysts are less active, although they have almost the same lattice constant as the EUP catalyst, so according to XRD they have almost the same composition. Obviously, some other effects not mentioned here could be also important.

5.3.3. Cyclic voltammetry in absence of methanol

Cyclic voltammograms of PtRu MEAs in absence of methanol are shown in Figure 5.12. The potential region is chosen in order to prevent dissolution of Ru [23]³⁵. In the description of the cyclic voltammetry behaviour (Figure 5.12), the potential region is “divided” into two regions: a “hydrogen adsorption/desorption” region due to similarity with the platinum behaviour (see Chapter 3)³⁶ and a “double layer region”³⁷.

³⁵ This aspect was already discussed in connection with the potential limits determination in CO stripping voltammetry. As it was pointed out, although reported in [23], no significant Ru dissolution is observed in our case. However, in these experiments a higher positive potential limit is not applied, first because more positive potential region is not interesting for fuel cell application of the catalyst and second due to Ru-oxide formation and reduction the whole cyclic voltammogram becomes a bit distorted and covers features that we want to discuss here.

³⁶ In case of Pt-Ru catalysts hydrogen adsorption proceeds only at Pt-adsorption sites and it is influenced by the adsorption of oxygen-containing species on Ru (Chapter 3).

The "hydrogen adsorption/desorption" region denotes region from - 0.2 to 0.1 V vs. Ag/AgCl. Voltammetric features of all catalysts in this region are somewhat different. According to literature data, catalyst's features in this region are influenced by Pt:Ru surface composition [16], [37], [47], [78]. In general, alloys containing more than 50 at % of platinum resemble more platinum like features, while those containing less than 50 at % platinum more ruthenium like features. For example, absence of the H-adsorption peak, which correspond to H-adsorption on "Pt(100)" surface, is observed for PtRu alloys with Ru content higher than 33 at % Ru [16]. Similar Chu and Gilman [37], showed that cyclic voltammograms of PtRu alloys containing less than 50 at % Ru resemble that of pure Pt, with H adsorption at potentials more positive than - 0.1 V vs. Ag/AgCl, while those for alloys containing more than 50 at % of Ru resemble that of pure Ru, *i.e.* no hydrogen adsorption at potential more positive than - 0.1 V vs. Ag/AgCl is observed. The same was seen in a recent paper of Batista *et al.* [78] for PtRu alloys with two different compositions Pt:Ru 85:15 and 50:50. Gradual decrease of typical Pt features was obtained on Pt-black catalyst after modification with Ru [47].

H-adsorption on platinum is completely suppressed on the KGE_{con} catalyst, which indicates a high Ru surface content. This Ru content is difficult to quantify and one can only say that it is higher than 50 at %. XRD, in a way, opposes this conclusion since, according to XRD the KGE_{con} catalyst is mixture of a Pt rich phase and Ru rich phase and more platinum like features would be expected. However, a high Ru surface composition and a lattice constant close to pure platinum do not necessarily oppose each other and both conditions are satisfied in the case of Pt particles decorated with Ru. In the literature, similar CV features as in that work were obtained in case of Pt(111) electrodes modified by Ru deposition [79-80]. So, tentatively it can be concluded that the KGE_{con} catalyst consists of Pt-rich particles decorated with Ru particles.

According to XRD and TEM, the EUP catalyst is mixture of Pt and Ru rich phases. Platinum features are seen in Figure 5.12, but they are not as pronounced as one would expect in case of 90 at % platinum alloy. An explanation can be the overlapping of Ru features with H-adsorption on Pt.

³⁷ In this region, the current is not only governed by a capacitive contribution, but also by Faradaic current due to OH adsorption.

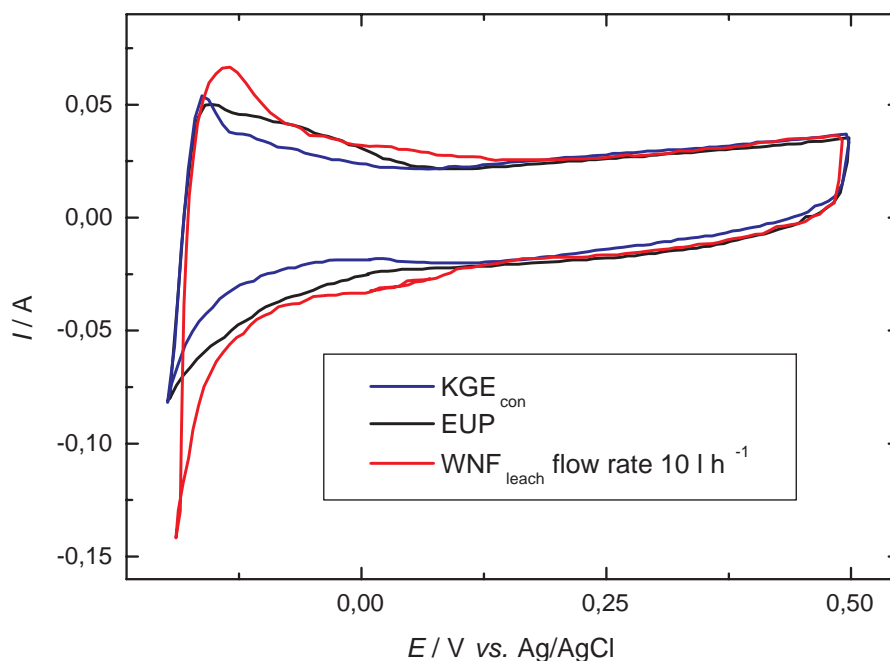


Figure 5.12 Cyclic voltammograms of different 30 % PtRu catalysts supported on Vulcan XC-72 at 22 °C. Water in the working electrode compartment. Sweep rate 50 mV s⁻¹. Flow rate 0 l h⁻¹ except for WNF_{leach} catalyst.

Very similar CV features as in the case of the WNF_{leach} catalyst were obtained for Ru decorated Pt black with a Ru surface coverage between 0.33 and 0.45 [47] as well as with unsupported PtRu with 58 at % Pt [37]. According to XRD, the WNF_{leach} catalyst is a PtRu alloy with approximately 50 at % Pt, which is in accordance to [37].

The double layer region extends approximately from 0.1 V to 0.5 V vs. Ag/AgCl and currents in the double layer region are the same for all catalysts. In general, the capacitive currents from the carbon support and the PtRu particles predominate, but some pseudo capacitive contributions (like OH adsorption/desorption and processes on Ru-oxides [81]) can also be present. In our case, the ratio of carbon support to metal catalyst was kept constant (30 % of metal catalyst on Vulcan XC-72) and the real surface areas of all catalysts were approximately the same, what explains the same current for different electrocatalysts in the double layer region.

Since the catalyst activity towards methanol oxidation was investigated at both room temperature and at 60°C, the influence of temperature on cyclic voltammetry behaviour in absence of methanol was also checked. It is shown in Figure 5.13 for the KGE_{con} - MEA. In comparison to room temperature, at higher temperatures hydrogen evolution starts at higher potentials. In addition, a difference is observed in the double layer region, where the beginning of the OH adsorption is shifted towards more negative potentials (see also Inset -

Figure 5.13) (due to the shift of the equilibrium potential of this reaction), which can have a promoting effect on the rate of methanol oxidation. The same features are observed for all other examined catalysts (not shown).

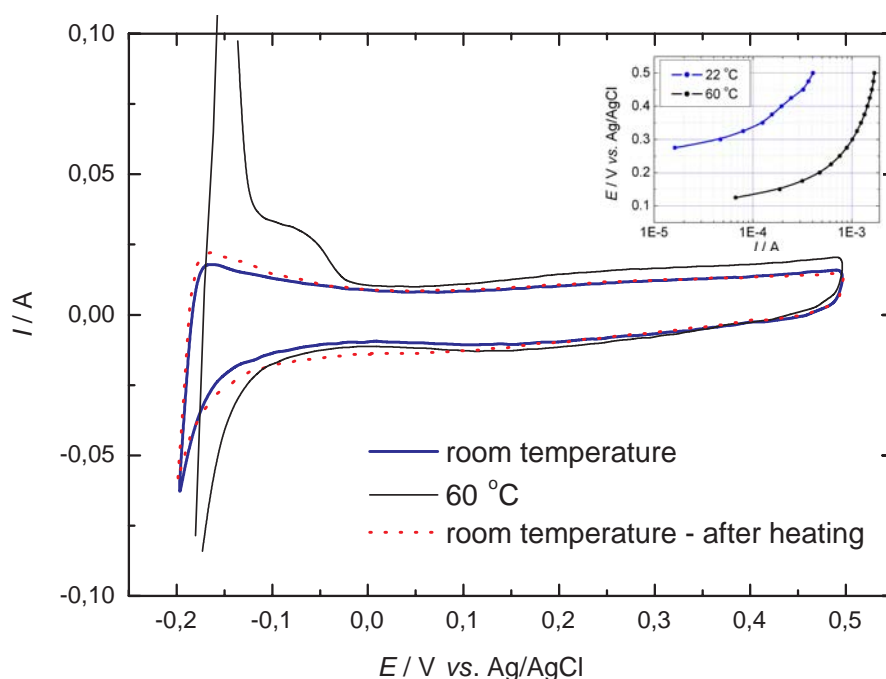


Figure 5.13 Cyclic voltammogram of the KGE_{con} catalyst, supported on Vulcan XC-72 at room temperature and 60 °C. Water in the working electrode compartment. Sweep rate 20 mV s^{-1} . Flow rate 10 l h^{-1} . Inset: Steady state measurements at room temperature and 60 °C. Conditions: fixed delay 5 min, water in the working electrode compartment, flow rate 10 l h^{-1} .

5.4. Catalyst activity in methanol oxidation

Steady-state experiments for methanol oxidation on different PtRu MEAs, at a flow rate of 10 l h^{-1} and at room temperature (22°C) and 60 °C, are shown in Figure 5.14. The currents are corrected for the background current, recorded at the same conditions in absence of methanol, but the correction was insignificant for all catalysts.

In Figure 5.14 two potential regions are observed. The potential region from 0.15 to 0.3 V vs. Ag/AgCl at room temperature and the region from 0.1 to 0.25 V vs. Ag/AgCl at 60°C, where the $E - \log(I)$ correlation is linear in the Tafel region, *i.e.* the activation controlled region (Chapter 4). In the potential region from 0.3 to 0.5 V vs. Ag/AgCl at room temperature and in the region from 0.25 to 0.5 V vs. Ag/AgCl at 60°C system reaches the limiting current level (Chapter 4).

Tafel slope values determined for different electrocatalyst from Figure 5.14 in the Tafel region are listed in Table 5.5.

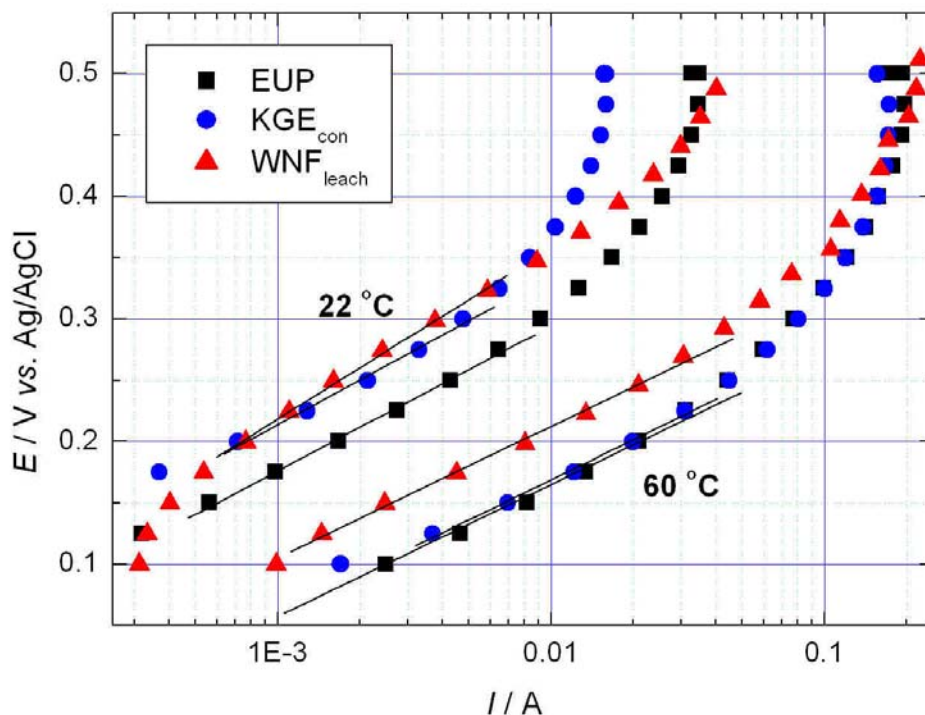


Figure 5.14 Steady state polarisation curves for methanol oxidation on different 30% PtRu/Vulcan XC-72 catalysts at 22 °C and 60 °C and at a flow rate of 10 l h⁻¹. Methanol concentration in the working electrode compartment: 1M.

At room temperature, Tafel slope values for EUP and KGE_{con} are almost the same (about 120 mV dec⁻¹), while the value for the WNF_{leach} catalyst is higher. At 60°C, Tafel slope values are approximately the same for all catalysts. The temperature increase causes a decrease of the Tafel slope value from 120 mV dec⁻¹ to approximately 108 mV dec⁻¹ for the EUP and KGE_{con} catalysts and from 139 to 107 mV dec⁻¹ for the WNF WA catalyst. By increasing the temperature a commencement³⁸ of the reaction shifts approximately 100 mV to lower values for all of the investigated catalysts. The reaction reaches the region of mixed control (potential region between activation controlled region and limiting current region) about 100 mV earlier than at room temperature.

In Chapter 4 a simple model for methanol oxidation was presented. According to this model, the Tafel slope value is changing from 40-44 mV dec⁻¹ (at room temperature and 60°C respectively) at very negative potentials to infinity at very positive potentials. Low Tafel slope value was not experimentally verified (it corresponds to low current values and it is influenced by background correction), while a slope close to infinity was recorded in the

³⁸ Commencement of the reaction is a poorly defined term. Here, it was chosen as potential where the observed current reaches 1 mA.

limiting current region. Experimentally obtained values are approximately 120 mV dec^{-1} at room temperature for KGE_{con} and EUP catalysts, while 139 mV dec^{-1} in case of the WNF_{leach} catalyst and about 110 mV dec^{-1} for all catalysts at $60 \text{ }^\circ\text{C}$. It was suggested in Chapter 4 that the experimental Tafel slope values do not correspond to a single *r.d.s.* as in a case of a simple electrochemical reaction, but belong to a transient region between low and high Tafel slope values in the model.

Table 5.5 Tafel slope values for different 30 % PtRu/Vulcan XC-72 catalysts at 22 and $60 \text{ }^\circ\text{C}$.

Catalyst	Slope / mV dec^{-1}	
	$t = 22^\circ\text{C}$	$t = 60^\circ\text{C}$
EUP	118	108
KGE _{con}	121	108
WNF _{leach}	139	107

The limiting current region is more pronounced in case of EUP and KGE_{con} catalysts than the WNF_{leach} catalyst. In Chapter 4, it was discussed that current in this region can be limited by slow transport of methanol (reactant) or CO_2 (product) when this current would be a diffusion limiting current or by a slow chemical reaction preceding the electrochemical reaction. In the latter case this current would be a reaction limiting current. It is also possible that the limiting current is dominated by both slow diffusion and slow chemical reaction. In the model proposed in Chapter 4 it was assumed that the limiting current is a reaction limiting current. This assumption was supported by some experimental findings, but it is still under consideration. It should be mentioned that diffusion limiting currents do not depend on the catalyst real surface area or catalyst composition. This means that all catalysts should have the same limiting currents if those currents are diffusion limited. In our case (Figure 5.14) this condition is not satisfied at room temperature, but at 60°C all limiting currents are almost the same. So this point remains unclear.

The catalytic activity for methanol oxidation decreases in the order: $\text{EUP} > \text{KGE}_{\text{con}} > \text{WNF}_{\text{leach}}$ at room temperature, while at $60 \text{ }^\circ\text{C}$ the activity of the EUP catalyst is the same as for the KGE_{con} catalyst. The lowest activity is again obtained for the WNF_{leach} catalyst.

The observed difference in activity can be caused by several reasons: a) different mechanism of methanol oxidation, b) different real surface areas, c) different extents of alloying, d) particle size effect, e) geometrical effect. These are discussed in the following.

In accordance to the model proposed in Chapter 4 the same mechanism for methanol oxidation is accepted for all examined catalysts, so the reason “a” as an explanation for different catalyst activities is discarded.

Real surface areas for all catalysts are obtained by means of CO stripping voltammetry. The trend is as follows: $WNF_{leach} > KGE_{con} > EUP$. Reaction rates for methanol oxidation are normalized with respect to the real surface areas (see Table 5.3) and the results are shown in Figure 5.15.

The trend in catalyst activity remained the same.³⁹ Almost no influence of the real surface area was observed since real surface areas of the catalysts are similar.

Catalyst characterisation (both *ex-situ* and *in-situ* methods) has shown, that the catalysts are different in the extent of Pt:Ru alloying, particle size etc. The highest activity was obtained for the EUP catalyst. This catalyst is considered as a mixture of a Pt-rich phase, a Ru metal phase and an oxide phase. The KGE_{con} catalyst has same lattice constant as the EUP catalyst, but it was assumed that Pt-rich particles are decorated with Ru particles. So a higher Ru surface concentration is expected in case of the KGE_{con} than in case of the EUP catalyst. Optimal Pt:Ru composition for methanol oxidation is changing with temperature [45]. At room temperature a Pt-rich catalyst is more active while at 60°C Ru begins to be active too. This would explain higher EUP activity at room temperature, while at 60 °C its activity becomes the same as for the KGE_{con} sample.

According to XRD data, the WNF_{leach} catalyst is a PtRu alloy with a Pt:Ru composition close to the nominal value. Tentatively, the same was concluded from electrochemical characterisation in absence of methanol. It was already reported that an alloyed catalyst has a lower activity than a non-alloyed [77]. From obtained in this work no definite conclusion can be drawn, since the WNF_{leach} catalyst differs from the other catalysts not just in the extent of PtRu alloying, but also in the Pt:Ru particle composition.

³⁹ It should be mentioned that using the area, which was determined by CO stripping at room temperature, for surface area normalisation at 60°C, is not completely justified in the case when oxide content in the catalysts is different.

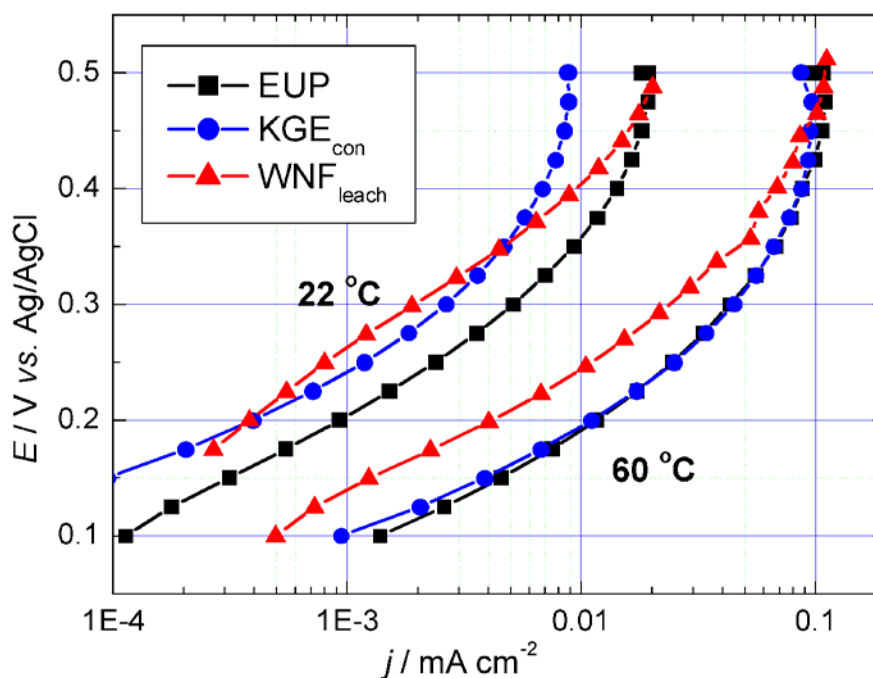


Figure 5.15 Steady state polarisation curves for methanol oxidation at different 30% PtRu/Vulcan XC-72 catalysts at 22 and 60 °C and at flow rate of 10 l h⁻¹. Methanol concentration in the working electrode compartment was 1M. Currents are normalized per real surface area.

5.4.1. Current vs. time - stability test

For fuel cell operation, not only a high catalyst activity towards methanol oxidation, but also good stability during the prolonged polarisation at constant potential is required. To test this, chronoamperometric experiments at 0.3 V were performed and the results are presented in Figure 5.16. For all investigated catalysts, steady state conditions are reached after approximately 10 min at 22 °C, while at 60°C steady state conditions were not reached in the investigated time span. At room temperature the potential at which the current decay is recorded, is in the Tafel region, while at 60°C it is in the region under mixed control (see Figure 5.14). It is possible that the system needs more time to reach steady state conditions at a higher temperature due to mixed control of the overall reaction. Such decrease of the catalytic activity with time was observed for other PtRu catalysts as well [82-83]. In respect to the stability at room temperature and 60°C all catalysts behave in the same way.

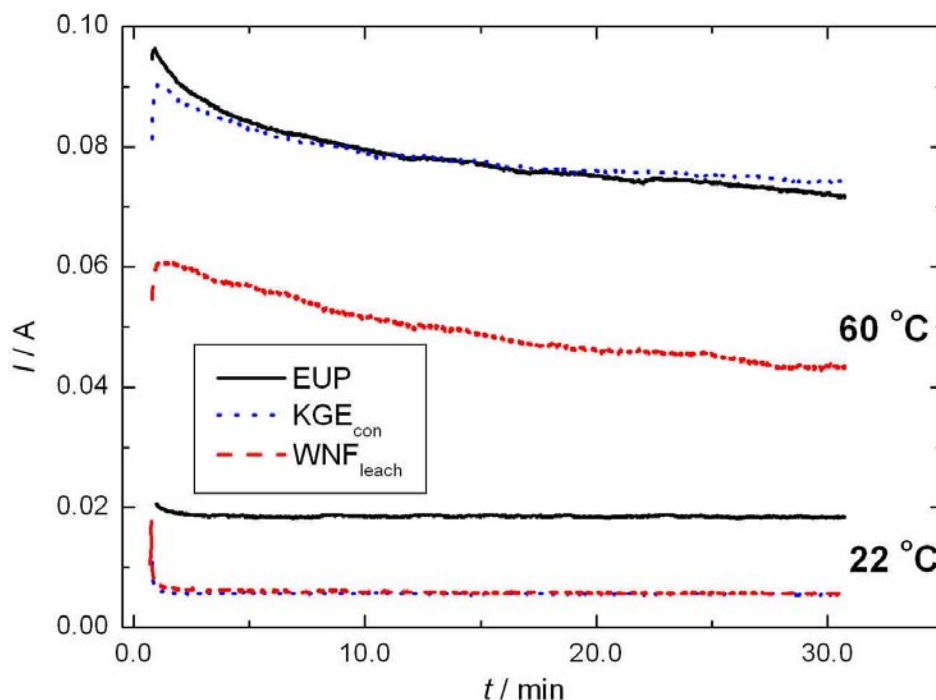


Figure 5.16 Current vs. time curves for different PtRu catalysts supported on Vulcan XC-72 at 0.3 V vs. Ag/AgCl and at 60 °C. Potential was 0.3 V vs. Ag/AgCl. Flow rate was 10 l h⁻¹. 1 M methanol solution in water was in the working electrode compartment.

5.4.2. Electrochemical impedance spectroscopy

Impedance plots for different 30%PtRu/Vulcan XC-72 catalysts in the frequency range from 2 kHz - 10 mHz at room temperature and 60°C are shown in Figure 5.17. All plots are ohmic resistance compensated.⁴⁰ Impedance plots are nominally recorded at 0.3 V vs. Ag/AgCl, but due to the ohmic resistance in the system real potential values were: 0.290 ± 0.003 V vs. Ag/AgCl at room temperature and 0.260 ± 0.003 V vs. Ag/AgCl at 60 °C.

Impedance plots at 22°C consist each of a not complete depressed semicircle, while at 60°C the semicircle is completely formed and in addition it has a low frequency inductive loop. The lack of an inductive loop at 22°C is due to the bigger total resistance. Increasing the temperature, the diameter of the semicircle decreases which indicates a lowering of the charge transfer resistance for methanol oxidation. As in Chapter 4, impedance spectra are shown only in a qualitative way and they reveal the same features as the impedance spectra of unsupported PtRu catalyst in Chapter 4.

⁴⁰ Ohmic resistance always appears at the high frequency end of the impedance spectra and is mainly governed by the electrolyte resistance (sulphuric acid and Nafion 105 membrane). Typical resistance values under the experimental conditions of this work (molar concentration of sulphuric acid was 1M) were: $1.3 \pm 0.1 \Omega$ at 22°C and $0.96 \pm 0.03 \Omega$ at 60°C.

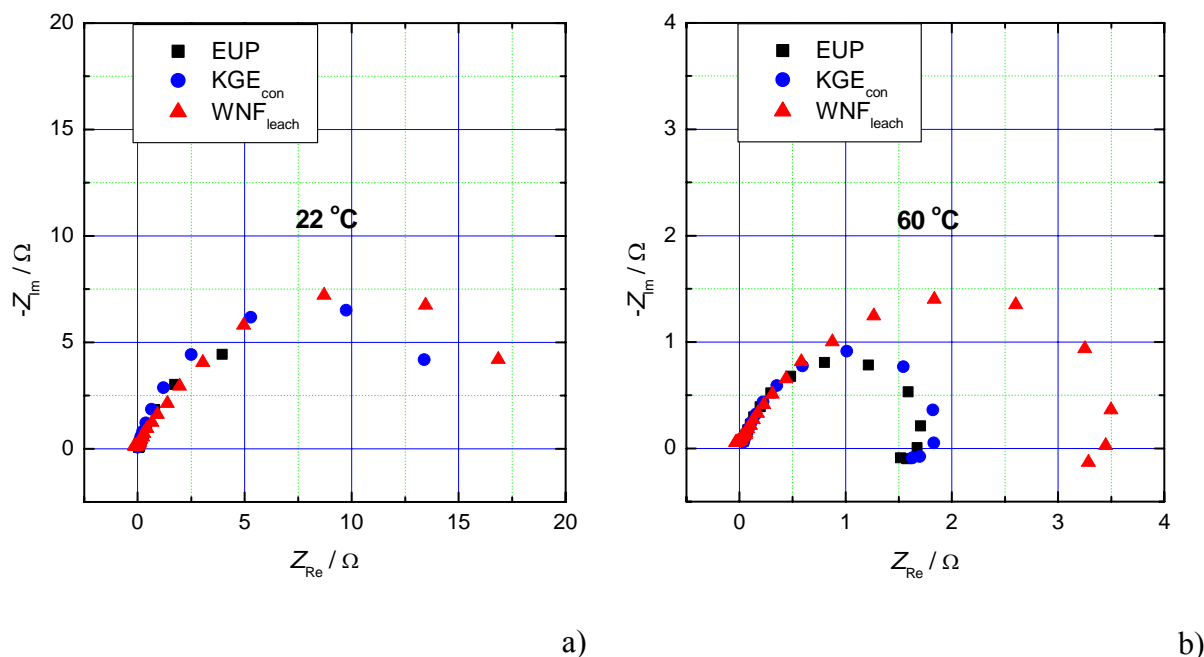


Figure 5.17 Experimental impedance plots for different 30%PtRu/Vulcan XC-72 catalysts at different temperatures: \square - EUP, \circ - KGE_{con} and Δ - WNF_{leach}. Conditions: 1 M methanol in working electrode compartment; flow rate 10 l h^{-1} , potential (nominal) 0.3 V vs. Ag/AgCl.

Also, impedance plots are in agreement with steady state data *i.e.* they support the same mechanism for methanol oxidation at all investigated catalysts.

5.5. Influence of conditioning, support and leaching

5.5.1. Influence of conditioning

The influence of conditioning on the KGE catalyst performance is shown in Figure 5.18, where cyclic voltammograms of unconditioned (KGE_{uncon}) and conditioned (KGE_{con}) catalysts prepared by KGE method in the absence of methanol are presented. The unconditioned sample is featureless, with a poorly pronounced hydrogen adsorption/desorption region and with high currents in the double layer region. Conditioning produced more Faradaic-like features, *i.e.* more pronounced hydrogen adsorption/desorption region and lower currents in the double layer region.

The expected effects of conditioning are the removal of organic residues from the catalyst surface, which remained after the synthesis, by initial O_2 treatment [66] and platinum reduction to zerovalent state as well as ruthenium reduction [84], which should occur during the subsequent H_2 conditioning. Camara *et al.* [66] showed that catalyst treatment under a H_2 atmosphere can modify the catalyst structure (Ru moves into the f.c.c crystal of Pt and a real

alloy is formed). According to XRD data, the lattice constant for the unconditioned sample is close to the lattice constant of pure platinum, while the conditioned sample has a value near the lattice constant of Pt-rich alloy.

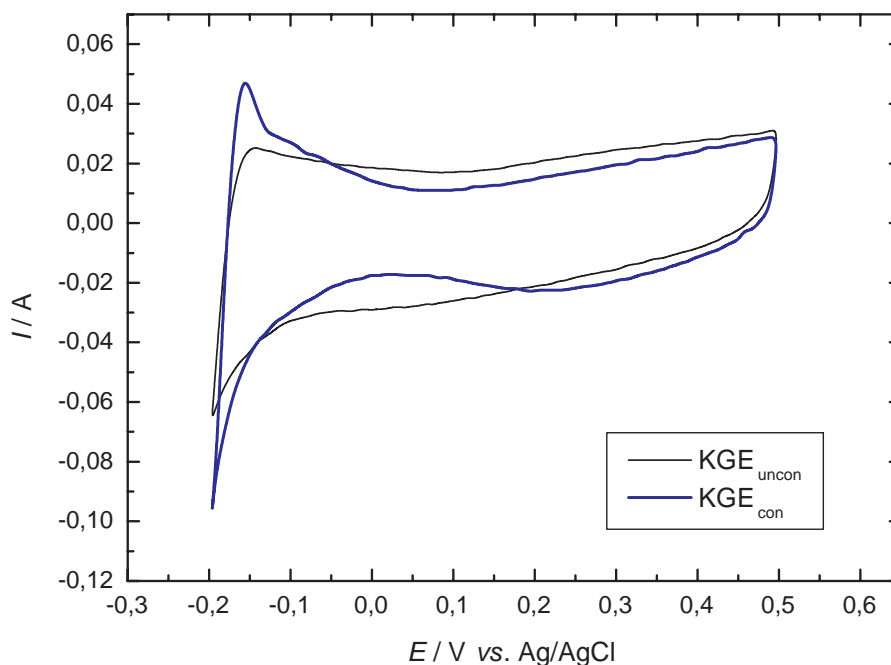


Figure 5.18 Cyclic voltammograms of unconditioned and conditioned KGE catalysts supported on Vulcan XC-72 at 22 °C. Water in the working electrode compartment. Sweep rate 50 mV s⁻¹. Flow rate 0 l h⁻¹.

The lower currents in the double layer region obtained after conditioning can be due to reduction of some Ru-oxides (the kind of Ru-oxides and the degree of hydration is synthetic sensitive. So, for example, RuO_xH_y is known to have a huge capacitance [81]). Increase of CO stripping area in the case of KGE_{con} compared to KGE_{uncon} sample was correlated to a decrease in quantity of the Ru-oxide phase in the former catalyst.

The influence of the catalyst conditioning on methanol electrooxidation is illustrated for the same KGE catalysts in Figure 5.19. The conditioned sample is more active in the whole potential region. The Tafel slope remains unchanged which indicates the same rate-determining step. Although data for the unconditioned sample are recorded at quasi-steady state conditions, a comparison with the conditioned sample where data are collected under steady-state conditions can still be made as was shown in the Chapter 2. A normalization per real surface area determined from CO stripping was applied, and the results are shown in Figure 5.20. After normalization, the activities of conditioned and unconditioned samples are almost the same. Hence conditioning only increases the active surface area.

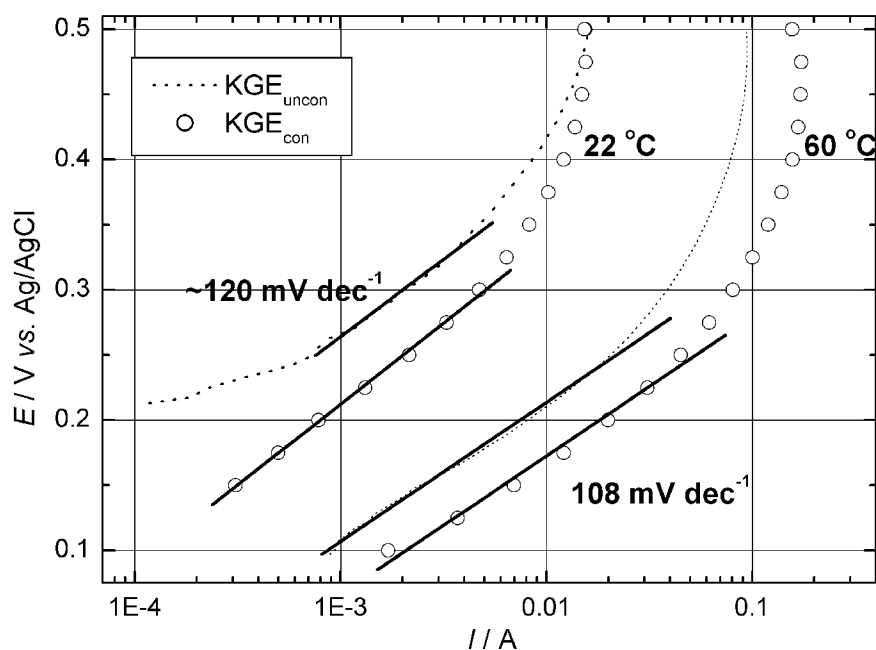


Figure 5.19 Tafel plots for methanol oxidation at unconditioned and conditioned 30% PtRu / Vulcan XC-72 at 22°C and 60°C and at a flow rate of 10 l h^{-1} . For the $\text{KGE}_{\text{uncon}}$ catalyst data are collected at sweep rate of 1 mV s^{-1} , while for the KGE_{con} catalyst in a steady state experiment.

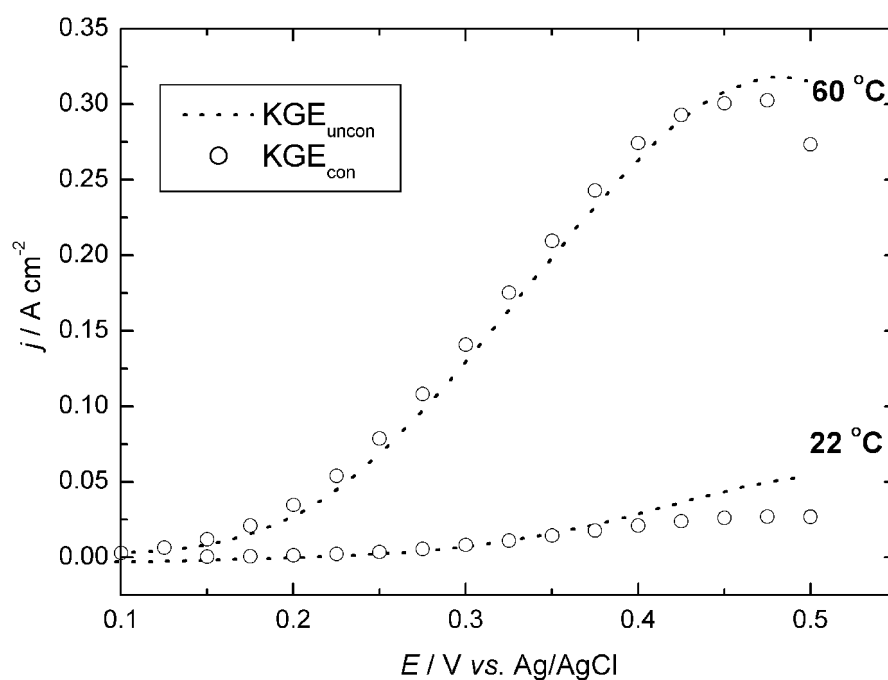


Figure 5.20 Polarisation curves for methanol oxidation at unconditioned and conditioned 30% PtRu / Vulcan XC-72 at 22°C and 60°C and at a flow rate of 10 l h^{-1} . Currents are normalized per real surface area determined from CO stripping experiments. Conditions are the same as for Figure 5.19.

5.5.2. Influence of support

Cyclic voltammograms of unconditioned supported and unsupported PtRu catalysts prepared by the KGE method in absence of methanol are shown in Figure 5.21. The shape of the voltammograms is the same. The supported sample shows higher currents due to the carbon support (both catalysts have the same metal loading, 1 mg cm^{-2} , while the supported sample additionally has a certain amount of carbon). The hydrogen adsorption/desorption region is somewhat more pronounced in case of the supported catalyst. Generally, the cyclic voltammetry behaviour resembles surfaces being enriched in Ru. (It is characteristic for pure Ru catalyst that the cyclic voltammogram is distorted, *i.e.* it is not very symmetrical to the zero current line and is shifted towards negative currents in the hydrogen region, while at more positive potential, in the region of oxide formation, it is distorted in the opposite direction [77]). Previously it was discussed that the KGE catalyst most probably consists of Pt particles decorated with Ru particles. In addition, the presence of a Ru-oxide phase is expected, although it is not clearly seen in the XRD patterns.

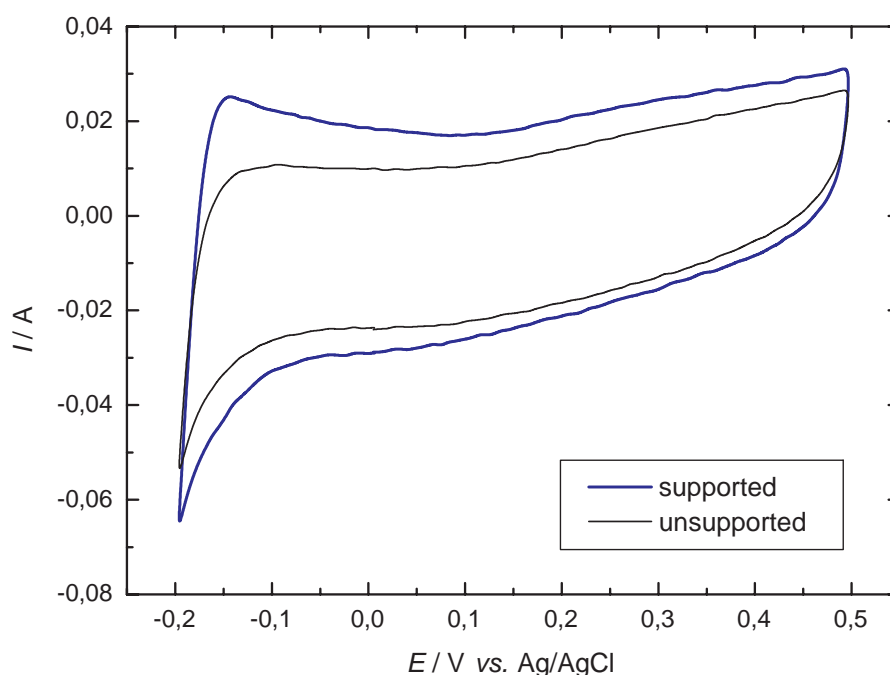


Figure 5.21 Cyclic voltammograms of supported and unsupported KGE catalysts at $22 \text{ }^{\circ}\text{C}$. Water in the working electrode compartment. Sweep rate 50 mV s^{-1} . Flow rate 0 l h^{-1} . Both supported and unsupported samples were unconditioned.

The supported catalyst is more active for methanol oxidation (Figure 5.22) than the unsupported one. The Tafel slopes are the same for both catalysts, so the mechanism of methanol oxidation is unchanged. A difference in activity of the supported *vs.* the unsupported catalyst is observed mainly in the limiting current region.

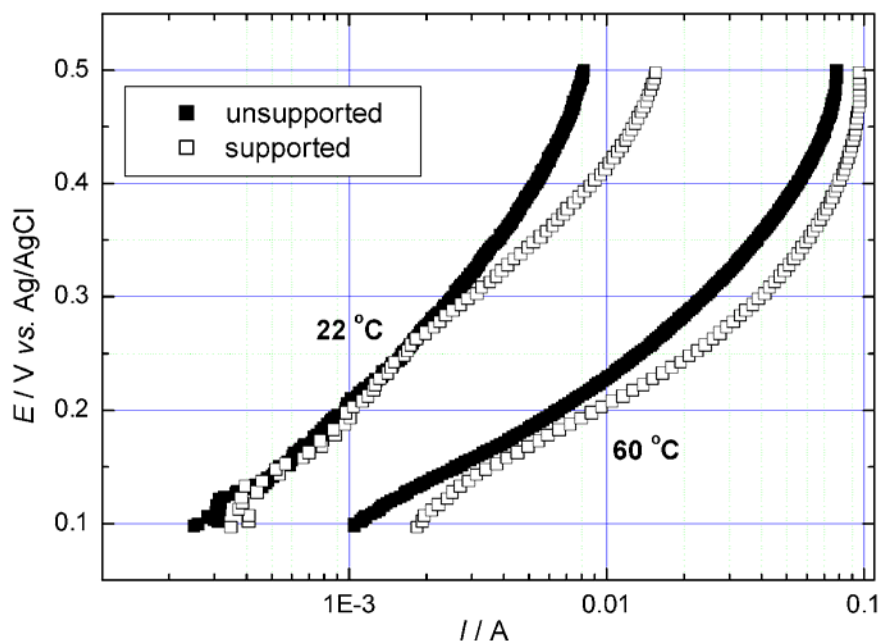


Figure 5.22 Tafel plots for methanol oxidation at supported and unsupported KGE KA catalysts at 22 °C and 60 °C, at a flow rate of 10 l h⁻¹. Data are collected at a sweep rate of 1 mV s⁻¹. 1 M methanol in the working electrode compartment.

5.5.3. Influence of leaching

Cyclic voltammograms of an unleached *i.e.* as-prepared catalyst (WNF_{unleach}) and leached (WNF_{leach}) samples are shown in Figure 5.23. The leached catalyst shows higher currents in the whole investigated potential region. This could be due to a problem with the unleached sample, which shows bad adhesion of the catalyst to the Nafion membrane, and as a result a low utilisation of the catalyst.

Activities of the leached and unleached samples in methanol oxidation at 22 °C and 60 °C were also investigated. The current values for the unleached sample at both room temperature and 60 °C were affected by background currents. This suggests a kind of disproportionality between the active surface area for methanol oxidation and processes taking place in absence of methanol.

Tafel slope values for unleached and leached samples are given in Table 5.6.

In general, the values for the unleached sample are higher than for the leached one. It was discussed that experimentally determined Tafel slope values, according to the model (Chapter 4), belong to the transient region, *i.e.* the Tafel slope varies from of 40 - 44 mV dec⁻¹ and infinity. The experimentally observed Tafel slope value depends on the ratio of rate constants of step 1 and step 3 in the mechanism for methanol oxidation (see Chapter 4).

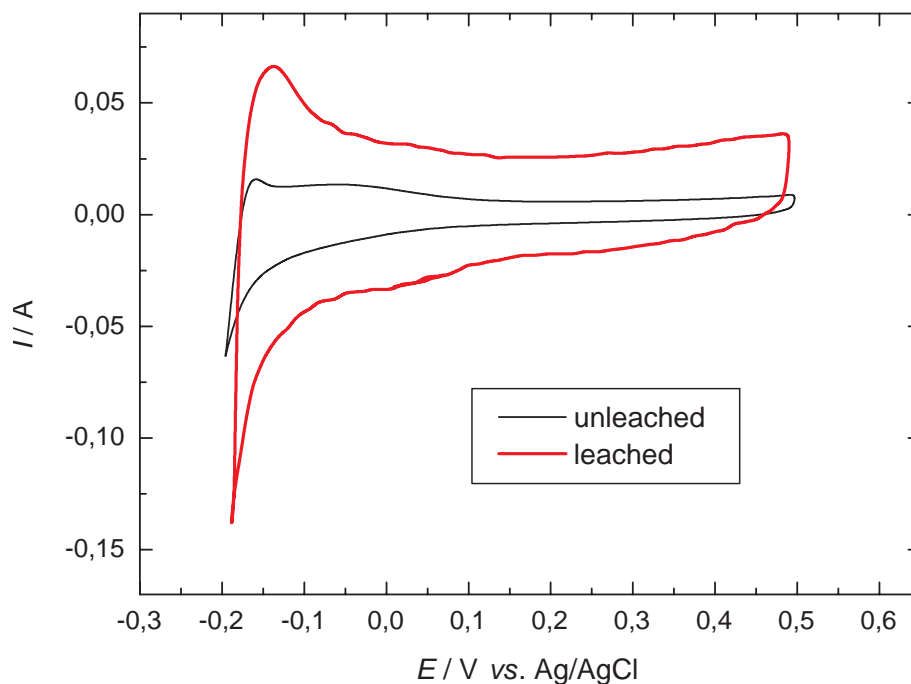


Figure 5.23 Cyclic voltammograms of an unleached ($\text{WNF}_{\text{unleach}}$) and leached ($\text{WNF}_{\text{leach}}$) catalysts prepared by the WNF method. Conditions: Water in working electrode compartment, sweep rate 50 mV s^{-1} , flow rate 0 l h^{-1} , temperature 22°C .

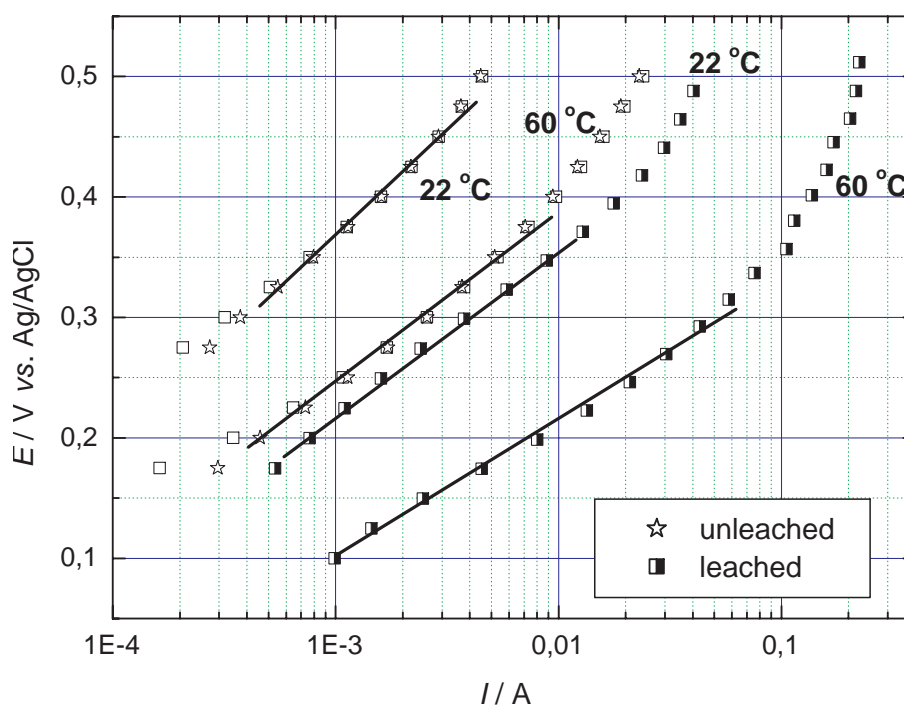


Figure 5.24 Steady state polarisation curves for methanol oxidation on unleached ($\text{WNF}_{\text{unleach}}$) and leached ($\text{WNF}_{\text{leach}}$) catalysts prepared by the WNF method, at 22 and 60°C , and at flow rate of 10 l h^{-1} . Methanol concentration in working electrode compartment was 1M . Hollow square stands for methanol oxidation currents of $\text{WNF}_{\text{unleach}}$, which are not corrected for background currents.

Table 5.6 Tafel slope values for unleached and leached samples prepared by WNF method. Data taken from Figure 5.24.

Catalyst	slope / mV dec ⁻¹	
	<i>t</i> = 22°C	<i>t</i> = 60°C
WNF _{unleach}	181	139
WNF _{leach}	139	107

If step 1 in the mechanism, *i.e.* methanol adsorption, is slow at a certain surface, then the apparent Tafel slope value will be higher.

There are at least two reasons for slow methanol adsorption in the case of the unleached sample. At first, an unleached sample has a very small particle size (according to TEM, from 0.8 – 1.2 nm) and second its surface is partially covered by the Al-protecting shell.

A so-called "particle-size" effect is reported in the literature with respect to methanol oxidation on platinum nanoparticles [85-87]. It was shown that for particle sizes in the range from 4.5 to 10 nm the activity is constant, while for particles in the range from 4.5 to 1.2 nm it decreases. Two possible explanations are offered. The first is that a decrease in particle size decreases the number of possible sites for methanol adsorption. This is due to geometrical reasons, *i.e.* smaller particles have greater edges and kinks to plain surface ratio, compared to larger particles [12]. In addition, as in this work, particles can be partly covered by Al-shell. According to the model developed by Gasteiger *et al.* [32], methanol adsorption requires three adjacent platinum sites at room temperature, while at 60°C methanol adsorption at Ru sites is also possible. Also, they appear to have less strongly bonded hydrogen sites at the surface and it is claimed that these sites are preferable for methanol adsorption [31]. The second explanation is that smaller Pt particles have greater affinity for OH adsorption, which in turn decreases the possibility of methanol adsorption since methanol and water adsorption are competitive processes. The last observation was confirmed in a XPS study where it was shown that smaller particles have greater affinity for oxide formation [87]. Also, cyclic voltammetry studies on the formation and reduction of Pt-oxide at Pt particles of different size have shown stronger adsorption of oxygenated species at Pt particles of smaller size [27], [85].

The lower overall activity of the unleached sample is due to a low total catalyst utilisation because of the problems in MEA preparation.

For both catalysts the limiting current is not reached at room temperature as well as for the unleached sample at 60 °C. The reason can be the low rate of the overall reaction.

5.6. Conclusions

Carbon supported and unsupported PtRu catalysts prepared by three varieties of the salt-reduction colloid method were investigated with regard to differences in morphology and in electrochemical behaviour.

EDX analysis showed that all catalysts, after leaching and conditioning, contain only platinum, ruthenium and carbon.

In XRD analysis, only peak reflections of the platinum f.c.c. structure were seen. Lattice constants of the EUP and KGE samples are close to lattice constant of pure Pt. They were assigned to a Pt rich PtRu alloy. In case of the WNF_{leach} catalyst, the lattice constant was close to the lattice constant of a PtRu alloy of approximately 50 at % Pt. No peak reflections of Ru h.c.p structure or of anhydrous or hydrous RuO₂ were observed. The particle size obtained by the XRD method decreases in the order KGE_{con}>EUP>WNF_{leach}.

TEM analysis revealed a uniform particle size distribution and dispersion over the carbon support. The average particle sizes obtained by TEM were lower than values obtained by XRD. In the case of the EUP catalyst, TEM with colour element mapping has shown metal phase segregation. Pt particles were observed next to Ru particles.

According to CO stripping voltammetry, the activities of EUP and WNF_{leach} catalysts are comparable, while the least active was KGE_{con}. The CO stripping surface areas follow the order WNF_{leach} > KGE ≈ EUP.

Cyclic voltammetry in absence of methanol showed some differences in the hydrogen adsorption/desorption region. The absence of H-adsorption at potentials higher than – 0.1 V vs. Ag/AgCl was ascribed to a Pt surface composition with less than 50 at % Pt.

The EUP catalyst has the highest activity in methanol oxidation at room temperature, while at 60°C activities of the EUP and the KGE_{con} catalysts were the same. Regarding the catalyst structures the following conclusions can be made: The EUP catalyst was found to consist of Pt rich particles and Ru particles nearby. The KGE_{con} consists of Pt particles decorated with Ru particles and finally the WNF_{leach} catalyst is a true PtRu alloy catalyst. For all catalysts, the same mechanism of methanol oxidation seems to be valid. After the currents were normalized per CO stripping area, the trend in catalyst activity remained the same. The

higher EUP than KGE_{con} catalyst activity at room temperature can be explained by a higher exposed Pt surface area in the former case. At 60°C it was assumed that Ru becomes active in methanol adsorption as well.

Catalyst conditioning, as shown at the KGE catalyst, results probably in some Ru-oxide reduction. A conditioned sample is more active than an unconditioned for methanol oxidation and the surface area (determined by CO stripping) was doubled with conditioning. The rate determining step remained the same after conditioning. After the currents are normalized with regard to the CO stripping surface area, the activities of the unconditioned and the conditioned samples were almost equal.

Comparison between a supported and unsupported sample showed a somewhat better performance towards methanol oxidation for the supported sample. Higher surface area in case of the supported sample is expected since some degree of particle agglomeration is mandatory for the unsupported samples. Tafel slope values for both supported and unsupported samples are the same, indicating the same mechanism of methanol oxidation.

The influence of leaching was demonstrated for two WNF supported catalysts. The unleached sample has a smaller particle size than the leached sample, but its performance in methanol oxidation was worse. The reason was the low utilisation of the unleached sample, which might be the result of the Al-shell and possible particle size effects.

5.7. Outlook

This Chapter showed that the characterisation of fuel cell catalysts is not simple at all. There are many unknowns and no single method for catalyst characterisation can give a definite answer. A combination of two or more methods is required. Here the use of CO stripping and cyclic voltammetry in absence of methanol in combination with XRD for catalyst characterisation was demonstrated.

XPS may give information on amorphous Ru-oxide species and DEMS can give information on distribution of reaction products, so these two methods are suggested in further catalysts characterisation.

Supported catalysts showed a higher activity with respect to methanol oxidation than the unsupported ones. In the future, it would be interesting to analyse the effect of different types of support on the activity using the same type of catalyst.

6. Concluding Remarks

The concluding remarks for this study can be summarized as follows:

In this study the cyclone flow cell was used for the first time for a systematical investigation of the kinetics of methanol electrooxidation. It proved to be suitable for such a study. Due to its unique feature, which allows investigation of electrochemical reactions in a membrane electrode assembly and at the same time a three electrode set-up, the experimental data are collected with a higher reliability than in a fuel cell set-up. Furthermore, well-defined hydrodynamic conditions enable a better determination of the role of diffusion in the overall anodic process.

The CO adsorption method can be used for the determination of real surface area of fuel cell catalyst under fuel cell relevant conditions (Chapter 3). It was shown that the experimentally obtained charge is greatly influenced by non-faradaic and other faradaic contributions, which underlines the importance of the base line subtraction and the choice of proper integration limits in comparing data of different catalysts. A method for the base line subtraction is proposed in order to eliminate the contributions due to oxide formation and double layer charging. The CO stripping line integration up to the half peak potential gave reliable results for the total CO charge, independent of the sweep rate used.

In Chapter 4 experimental data on the kinetics of methanol oxidation on a commercial catalyst are presented. The influence of the flow rate, the methanol concentration and the temperature was investigated. Based on these experimental and literature data, a model of methanol electrooxidation is selected and a rate expression is formulated. A good agreement between experimental data and simulated results was obtained after fitting of the kinetic parameters.

In Chapter 5 carbon supported and unsupported PtRu catalysts prepared by three variations of the salt-reduction colloid method were investigated with respect to their differences in morphology and in electrochemical behaviour. All catalysts were nominally with the same PtRu composition. Based on physical methods (EDX, XRD, TEM) and electrochemical methods (CV, CO stripping) it was concluded that only one catalyst

(WNF_{leach}) is a PtRu alloy with a Pt:Ru composition close to the nominal one. The best activity in methanol oxidation was obtained for the EUP catalyst, which was found to be a mixture of PtRu alloy with high Pt content, and metallic and oxide Ru phases. The model proposed in Chapter 4 is consistent with the experimental data obtained using these new catalysts.

7. References

- [1] T. Schultz, S. Zhou, K. Sundmacher, *Chem. Eng. Technol.* 24 (2001) 1223 – 1233.
- [2] W. Vielstich, in: E. Julio Calvo (Ed.), *Interfacial Kinetics and Mass Transport*, Vol. 2, Wiley-VCH, Weinheim, 2003, pp. 466 – 511.
- [3] K. Sundmacher, *J. Appl. Electrochem.*, 29 (1999) 919 - 926.
- [4] L. Jörissen, V. Gogel, J. Kerres, J. Garche, *J. Power Sources*, 105 (2002) 267 - 273.
- [5] T. Schultz, Ph. D. Thesis, Otto-von-Guericke University, Magdeburg, 2004, p.61.
- [6] E. Gileadi, *Electrode Kinetics for Chemists, Chemical Engineers and Material Scientists*, Wiley-VCH, New York, 1993.
- [7] E. Herrero, K. Franaszczuk, A. Wieckowski, *J. Phys. Chem.*, 98 (1994) 5074 – 5083.
- [8] F. Nart, W. Vielstich, in: W. Vielstich, H. A. Gasteiger, A. Lamm (Eds), *Handbook of Fuel Cells – Fundamentals, Technology and Applications*, Vol. 2. Electrocatalysis, John Wiley&Sons, Weinheim, 2003, Ch. 21 and references therein.
- [9] J. Clavilier, A. Rodes, K.El. Achi, M.A. Zamakhchari, *J. Chim. Phys.*, PCB, 88 (1991) 1291 - 1337.
- [10] M.E. Martins, C.F. Zinola, G. Andreasen, R.C. Salvarezza, A. J. Arvía, *J. Electroanal. Chem.*, 445 (1998) 135 - 154.
- [11] D. Armand, J. Clavilier, *J. Electroanal. Chem.*, 233 (1987) 251 - 265.
- [12] J. McBreen, S. Mukerjee, in: A. Wieckowski (Ed) *Interfacial Electrochemistry, Theory, Experiment and Application*, Marcel Dekker, Inc, New York, 1999, Ch. 49.
- [13] T. J. Schmidt, H. A. Gasteiger, G. D. Stáb, P. M. Urban, D. M. Kolb, R. J. Behm, *J. Electrochem. Soc.*, 145 (1998) 2354 - 2357.
- [14] S. Lj. Gojković, T. R. Vidaković, *Electrochim. Acta*, 47 (2001) 633 - 642.
- [15] S. Gilman, *J. Phys. Chem.*, 66 (1962) 2657 - 2664.

- [16] H. Gasteiger, N. Marković, P. Ross, E. Cairns, *J. Phys. Chem.*, 98 (1994) 617 - 625.
- [17] Z. Jusys, T. J. Schmidt, L. Dubau, K. Lasch, L. Jörissen, J. Garche, R. J. Behm, *J. Power Sources*, 105 (2002) 297 - 304.
- [18] J. P. Iudice de Souza, T. Iwasita, F. C. Nart, W. Vielstich, *J. Appl. Electrochem.*, 30 (2000) 43 - 48.
- [19] H. N. Dinh, X. Ren, F. H. Garzon, P. Zelenay, S. Gottesfeld, *J. Electroanal. Chem.*, 491 (2000) 222 - 233.
- [20] B. Gurau, E. Smotkin, *J. Power Sources*, 112 (2002) 339 - 352.
- [21] D. S. Corrigan, M. J. Weaver, *J. Electroanal. Chem.*, 241 (1988) 143-162.
- [22] N. M. Marković, B. N. Grgur, C. A. Lucas, P. N. Ross, *J. Phys. Chem.*, B103 (1999) 487 - 495.
- [23] S. Gojković, T. Vidaković, D. Đurović, *Electrochim. Acta*, 48 (2003) 3607 – 3614 and references therein.
- [24] S. Srinivasan, E. Gileadi, *Electrochim. Acta*, 11 (1966) 321-335.
- [25] S. Trasatti, W. O'Grady, in: H. Gerisher, C. W. Tobias (Eds), *Advances in Electrochemistry and Electrochemical Engineering*, Vol. 12, Wiley, New York, 1981, pp. 177 - 261.
- [26] P. Liu, A. Logadottir, J. K. Nørskov, *Electrochim. Acta*, 48 (2003) 3731 – 3742.
- [27] A. S. Aricò, S. Srinivasan, V. Antonucci, *Fuel Cells*, 1 (2001) 133 – 161.
- [28] V. Bagotzky, Y. Vassiliev, O. Khazova, *J. Electroanal. Chem.*, 81 (1977) 229 - 238.
- [29] R. Parsons, T. VanderNoot, *J. Electroanal. Chem.*, 257 (1987) 9 – 54.
- [30] A. Hamnett, *Catalysis Today*, 38 (1997) 445-457.
- [31] A. Hamnett, in: A. Wieckowski (Ed.), *Mechanism of Methanol Electrooxidation, Interfacial Electrochemistry, Theory, Experiment and Applications*, Marcel Dekker, New York, 1999, Ch. 47.
- [32] H. Gasteiger, N. Markovic, P. Ross, E. Cairns, *J. Phys. Chem.*, 97 (1993) 12020 - 12029.
- [33] A. Kabbabi, R. Faure, R. Durand, B. Beden, F. Hahn, J. M. Leger, C. Lamy, *J. Electroanal. Chem.*, 444 (1998) 41 - 53.

- [34] O. Khazova, A. Mikhailova, A. Skundin, E. Tuseeva, A. Havránek, K. Wippermann, *Fuel Cells*, 2 (2002) 99 - 108.
- [35] T. Vidaković, M. Christov, K. Sundmacher, *Electrochim. Acta*, 49 (2004) 2179 - 2187.
- [36] Z. Jusys, J. Kaiser, R. J. Behm, *Electrochim. Acta*, 47 (2002) 3693 - 3706.
- [37] D. Chu, S. Gilman, *J. Electrochem. Soc.*, 143 (1996) 1685 - 1690.
- [38] H. Wang, C. Wingender, H. Baltruschat, M. Lopez, M. Reetz, *J. Electroanal. Chem.*, 509 (2001) 163 - 169.
- [39] M. Watanabe, S. Motoo, *J. Electroanal. Chem.*, 60 (1975) 267 - 273.
- [40] Q. Fan, C. Pu, E. Smotkin, *J. Electrochem. Soc.*, 143 (1996) 3053 - 3057.
- [41] J. Leger, *J. Appl. Electrochem.*, 31(2001) 767 - 771.
- [42] D. Kardash, C. Korzeniewski, N. Marković, *J. Electroanal. Chem.*, 500 (2001) 518 - 523.
- [43] J. Kua, W. Goddard, *J. Am. Chem. Soc.*, 121 (1999) 10928 - 10941.
- [44] T. Schmidt, H. Gasteiger, R. Behm, *Electrochem. Commun.*, 1 (1999) 1 - 4.
- [45] H. Gasteiger, N. Marković, P. Ross, E. Cairns, *J. Electrochem. Soc.*, 141 (1994) 1795 - 1803.
- [46] A. Kulikovskiy, *Electrochem. Commun.*, 5 (2003) 530 - 538.
- [47] D. Cao, S. Bergens, *Electrochim. Acta*, 48 (2003) 4021 - 4031.
- [48] D. Rolison, P. Hagans, K. Swider, J. Long, *Langmuir*, 15 (1999) 774 - 779.
- [49] B. E. Conway, *Electrochemistry Encyclopedia, Electrochemical Capacitors - Their Nature, Function, and Applications*, Chemistry Department, University of Ottawa, Canada (March, 2003) <http://electrochem.cwru.edu/ed/encycl/art-c03-elchem-cap.htm>
- [50] B. Gurau, E. Smotkin, *J. Power Sources*, 112 (2002) 339 - 352.
- [51] Z. J. Derlacki, A. J. Easteal, A. V. J. Edge, L. A. Woolf, Z. Roksandric, *J. Phys. Chem.*, 89 (1985) 5318 - 5322.
- [52] W. H. Mulder, J. H. Sluytes, T. Pajkossy, I. Nyikos, *J. Electroanal. Chem.*, 285 (1990) 103 - 115.
- [53] R. Melnick, T. Palmore, *J. Phys. Chem.*, B 105 (2001) 1012 - 1025.

- [54] I.-M. Hsing, X. Wang, Y.-J. Leng, *J. Electrochem. Soc.*, 149 (5) (2002) A615-A621.
- [55] J. Müller, P. Urban, W. Hölderich, *J. Power Sources*, 84 (1999) 157 - 160.
- [56] M. Ciureanu, H. Wang, Z. Qi, *J. Phys. Chem., B* 103 (1999) 9645 - 9657.
- [57] T. Iwasita, F. Nart, W. Vielstich, *Ber. Bunsenges. Phys. Chem.*, 94 (1990) 1030 – 1034.
- [58] N. Markovic, H. Gasteiger, P. Ross, X. Jiang, I. Villegas, M. Weaver, *Electrochim. Acta*, 40 (1995) 91 - 98.
- [59] J. Meyers and J. Newman, *J. Electrochem. Soc.*, 149 (6) (2002) A718 – A728.
- [60] C. Lamy, A. Lima, V. Lerhum, F. Deline, C. Contanceu, *J. Power Sources*, 105 (2002) 283 - 296.
- [61] H. Bönnemann, R. M. Richards, *Eur. J. Inorg. Chem.*, 10 (2001) 2455 - 2480.
- [62] H. Bönnemann, S. Kinge, in preparation.
- [63] Y. Takasu, T. Fujiwara, Y. Murakami, K. Sasaki, M. Orguri, T. Asaki, W. Sugimoto, *J. Electrochem. Soc.*, 147 (12) (2000) 4421 - 4427.
- [64] Y. Takasu, T. Kawaguchi, W. Sugimoto, Y. Murakami, *Electrochim. Acta*, 48 (2003) 3861 - 3868.
- [65] W. H. Lizcano-Valbuena, V. A. Paganin, C. A. P. Leite, F. Galambeck, E. R. Gonzalez, *Electrochim. Acta*, 48 (2003) 4239 - 4244.
- [66] G. A. Camara, M. J. Giz, V. A. Paganin, E. A. Ticianelli, *J. Electroanal. Chem.*, 537 (2002) 21 - 29.
- [67] W. D. King, J. D. Corn, O. J. Murphy, D. L. Boxall, E. A. Kenik, K. C. Kwiatkowski, S. R. Stock, C. M. Lukehart, *J. Phys. Chem. B*, 107 (2003) 5467 - 5474.
- [68] C. W. Hills, M. S. Nashner, A. I. Frenkel, J. R. Shapley, R. G. Nuzzo, *Langmuir*, 15 (1999) 690 - 700.
- [69] C. W. Hills, N. H. Mack, R. G. Nuzzo, *J. Phys. Chem. B*, 107 (2003) 2626 - 2536.
- [70] A. S. Aricò, V. Baglio, E. Modica, A. Di Blasi, V. Antonucci, *Electrochem. Communications*, 6 (2004) 164 - 169.
- [71] H. Bönnemann, R. Richards in: A. Wieckowski et al (Eds), *Catalysis and Electrocatalysis at Nanoparticle Surfaces*, Marcel Dekker, Inc., New York, 2003, Chapter 10 Nanomaterials as Precursors for Electrocatalysis.

- [72] A. J. Dean (Ed.), *Lange's Handbook of Chemistry*, 13th Edition, McGraw-Hill, New York, 1985, 3.124 - 3.125.
- [73] V. Radmilovic, H. A. Gasteiger, P. N. Ross, Jr, *J. Catalysis*, 154 (1995) 98 - 106.
- [74] H. A. Gasteiger, P. N. Ross, Jr, E. J. Cairns, *Surface Science*, 293 (1993) 67 - 80.
- [75] A. I. Frenkel, C. W. Hills, R. G. Nuzzo, *J. Phys. Chem. B*, 105 (2001) 12689 - 12703.
- [76] L. Dubau, C. Coutanceau, E. Garnier, J.-M. Leger, C. Lamy, *J. Appl. Electrochem.*, 33 (2003) 419 -
- [77] L. Dubau, F. Hahn, C. Coutanceau, J.-M. Leger, C. Lamy, *J. Electroanal. Chem.*, 554-555 (2003) 407 - 415
- [78] E. A. Batista, H. Hoster, T. Iwasita, *J. Electroanal. Chem.*, 554-555 (2003) 265 - 271.
- [79] W.F. Lin, M. S. Zei, M. Eiswirth, G. Ertl, T. Iwasita, W. Vielstich, *J. Phys. Chem. B*, 103 (1999) 6968 - 6977.
- [80] K. A. Friedrich, K. P. Geyzers, U. Linke, U. Stimming, J. Stumper, *J. Electroanal. Chem.*, 402 (1996) 123 - 128.
- [81] V. Panić, T. Vidaković, S. Gojković, A. Dekanski, S. Milonjić, B. Nikolić, *Electrochim. Acta*, 48 (2003) 3805 - 3813.
- [82] H. Hoster, T. Iwasita, H. Baumgartner, W. Vielstich, *J. Electrochem. Soc.*, 148 (2001) A496 – A501.
- [83] A. Hamnett, S. Weeks, B. Kennedy, G. Troughton, P. Christensen, *Ber. Bunsenges. Phys. Chem.*, 94 (1990) 1014 - 1020.
- [84] J. Long, R. Stroud, K. Swider-Lyons, D. Rolison, *J. Phys. Chem., B* 104 (2000) 9772 - 9776.
- [85] A. Kabbabi, F. Gloaguen, F. Andolfatto, R. Durand, *J. Electroanal. Chem.*, 373 (1994) 251 - 254.
- [86] T. Frelink, W. Visscher, J. A. R. van Veen, *J. Electroanal. Chem.*, 382 (1995) 65 - 72.
- [87] F. Parmigiani, E. Kay, P. S. Bagus, *J. Electron. Spectrosc. Relat. Phenom.*, 50 (1990) 39 - 46.

Appendix I

List of symbols

Bi	Biot number (dimensionless)
$c_{\text{CH}_3\text{OH}}$	bulk methanol concentration (mol dm^{-3})
c_{H^+}	H^+ concentration in Nafion membrane (1.2 mol dm^{-3})
$a_{\text{CH}_3\text{OH}}$	reaction order with respect to methanol (dimensionless)
$c_{\text{H}_2\text{O}}$	water concentration (55.5 mol dm^{-3})
ΔH_{ads}	enthalpy of adsorption of step (2) (J mol^{-1})
a	lattice parameter (nm)
$B_{(2\theta)}$	width of the peak at the half height (in rad)
C_{dl}	double layer charging (F)
D	methanol diffusion coefficient in water ($\text{m}^2 \text{ s}^{-1}$)
d	particle diameter (nm)
Da_{II}	Damköhler number of second kind (dimensionless)
D^{BDL}	methanol diffusion coefficient in back diffusion layer ($\text{m}^2 \text{ s}^{-1}$)
d^{BDL}	thickness of back diffusion layer (μm)
D^{CL}	methanol diffusion coefficient in catalyst layer ($\text{m}^2 \text{ s}^{-1}$)
d^{CL}	thickness of catalyst layer (μm)
d_{in}	diameter of the inlet tube (here 0.40 cm)
E	potential (V)
E^θ	equilibrium potential (V)
$E_{\text{a,app}}$	apparent activation energy (J mol^{-1})
$E_{\text{a,i}}$	activation energy for the i -th step in a reaction mechanism (J mol^{-1})
E_{p}	potential energy (J)

F	Faraday's constant (96485 C mol ⁻¹)
I	total current (A)
I_{dl}	double layer current (A)
I_{mass}	current normalized with respect to metal loading (A g _{PtRu} ⁻¹)
j	current density (per geometric surface area) (A m ⁻²)
k_i	rate constant for the i-th step in the reaction mechanism
k_m	external film mass transport coefficient (m s ⁻¹)
mass _{Pt}	mass content of Pt determined from EDX (%)
mass _{Ru}	mass content of Ru determined from EDX (%)
Q	charge to oxidize full monolayer of CO adsorbed (C)
Q_{CO}	CO stripping charge (C)
Q_H	hydrogen desorption charge (C)
r	electrode radius (here, 0.80 cm)
R	universal gas constant (8.314 J mol ⁻¹ K ⁻¹)
Re	Reynolds number (dimensionless)
r_a	distance between metal colloids (nm)
r_i	reaction rate for the i-th step in the reaction mechanism (A)
r_{in}	cyclone radius at the middle of the inlet tube (here 2.97 cm)
S	real surface area (cm ²)
Sc	Schmidt number (dimensionless)
S_{CO}	CO surface area (cm ²)
Sh	Sherwood number (dimensionless)
S_{sp}	specific surface area (m ² g ⁻¹)
S_{XRD}	specific surface area determined from XRD particle size diameter (m ² g ⁻¹)
T	temperature (°C)
t	time (s)

V	volumetric flow rate ($\text{dm}^3 \text{min}^{-1}$)
Z_{Im}	impedance imaginary part (Ω)
Z_{Re}	impedance real part (Ω)

Greek letters

α_i	charge transfer coefficient for the i-th step of reaction mechanism (dimensionless)
$\lambda_{\text{K}\alpha 1}$	wavelength of X-rays used (here 0.154056 nm)
μ	dynamic viscosity of fluid (Pa s)
θ_{CO}	CO coverage on the platinum sites (dimensionless)
$\theta_{\text{CO}}^{\text{sat}}$	CO saturated surface coverage (dimensionless)
θ_{OH}	OH coverage on the ruthenium sites (dimensionless)
θ_{H}	hydrogen coverage at end-point potential (dimensionless)
2θ	diffraction angle ($^\circ$)
θ_{max}	Bragg angle ($^\circ$)
ρ	fluid density (kg m^{-3})
ρ_{PtRu}	PtRu alloy density (kg m^{-3})
ρ_{Pt}	Pt density (kg m^{-3})
ρ_{Ru}	Ru density (kg m^{-3})
ω	angular velocity (s^{-1})
v	sweep rate (mV s^{-1})

Abbreviations

BDL	back diffusion layer
BET	Brunauer Emmett Teller surface area measured with N_2
CFC	Cyclone Flow Cell

CL	Catalyst Layer
CV	Cyclic Voltammetry
DEMS	Differential Electrochemical Mass Spectroscopy
DMFC	Direct Methanol Fuel Cell
EDX	Energy Dispersive X-ray Analysis
EIS	Electrochemical Impedance Spectroscopy
EMIRS	Electrochemically Modulated Infra Red Spectroscopy
FTIR	Fourier Transform Infra Red Spectroscopy
FTIR-DRS	Fourier Transform Infrared-Diffuse Reflection Spectroscopy
H-region	hydrogen adsorption / desorption region (here from -0.2 to 0.1 V vs. Ag/AgCl).
IR	Infra-Red Spectroscopy
IRRAS	Infra-Red Reflection Absorption Spectroscopy
MEA	Membrane Electrode Assembly
O-region	in platinum potential region between 0.8 and 1.2 V vs. Ag/AgCl
r.d.s	rate determining step
RHE	Reversible Hydrogen Electrode
SEM	Scanning Electron Microscopy
SPAIRS	Single Potential Alteration Infrared Spectroscopy
STM	Scanning Electron Microscopy
TEM	Transmission Electron Microscopy
XPS	X-ray Photoelectron Spectroscopy
XRD	X-ray Diffraction

Appendix II

MEA notation

In this study the following MEA notation was used. For example:

13 CC C N105 APtRu5 003

- 13** denotes **total geometrical surface area**. In this case 12.56 cm².
- CC** denotes **cyclone cell**
- C** denotes the **type of the back diffusion layer**, here carbon cloth (alternatively for Toray paper would be T22 where the number denotes Teflon content in *mass %*).
- N105** type of **Nafion membrane** used for the MEA
- A** denotes **anode** side in the investigated cell
- PtRu** stands for the **type of catalyst**, here unsupported PtRu catalyst; alternatively for supported catalyst would be PtRuC. Non-commercial catalysts were denoted with corresponding names (Table A II.1)
- 5** stands for **metal loading** (here 5 mg cm⁻²)
- 003** denotes the **number** of MEA

Table A II.1 Non-commercial catalyst notation and abbreviations

Method	Catalyst description	Full name	Abbreviation
EUP	Supported, conditioned	EUP AA 105 03	EUP
KGE	Supported, unconditioned	KGE KA 083 01	KGE _{uncon}
	Supported, conditioned	KGE KA 083 02	KGE _{con}
	Unsupported, unconditioned	KGE KA 084 01	KGE _{unsupp}
WNF	Supported, unleached	WNF WA 083 01	WNF _{unleach}
	Supported, leached	WNF WA 152 04	WNF _{leach}